UNIVERSITÀ DEGLI STUDI DI PADOVA

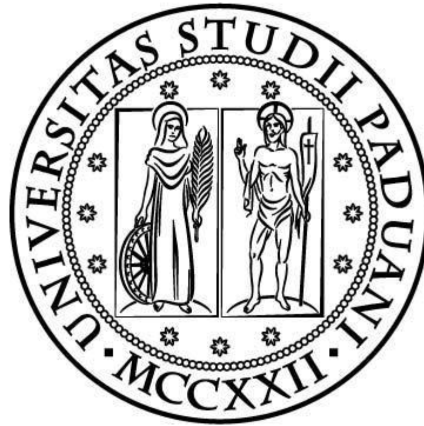

Dipartimento di Tecnica e Gestione dei Sistemi Industriali

Master's Thesis in Product Innovation Engineering

Interferometric Investigation of Liquid Thin Film Meniscus

Supervisor
PROF. SIMONE MANCIN
Università degli studi di Padova

Master candidate
MARTINA TOMELLERI
Matr: 1154260

Co-supervisor
PROF. JUSTIN WEIBEL
Purdue University

ABSTRACT

An interferometric investigation of liquid thin film meniscus on a smooth solid surface is presented. The curvature profiles in the contact line region of a microfilm of octane on a silicon wafer are measured in the earth's gravitational field, at room temperature and pressure. The profiles, which are function of the stress field, are obtained using image-analyzing interferometry technique and an improved data analysis procedure of the naturally occurring interference fringes. An experimental system is designed to microscopically study the extended meniscus curvature of the liquid-solid interface.

A parameter introduced, representing the average curvature of the extended meniscus, is used to compare the results, in order to analyze the effect of closeness to solid wall and of the filling ratio of the chamber on meniscus shape and film thickness.

The objective of the work presented in the proposed thesis is to experimentally verify the accuracy and repeatability of the reflectivity analysis and cleaning procedures achieving consistent results of the curvature measurements.

SOMMARIO

Nella seguente tesi viene presentata un'indagine interferometrica di un sottile menisco di liquido su una superficie liscia. Sono stati misurati i profili di curvatura dell'ottano su un campione di silicio, in campo gravitazionale e in condizioni di temperatura e pressione ambiente. La tecnica interferometrica viene utilizzata per ottenere il profilo di spessore del liquido, funzione del campo di pressioni, analizzando le frange interferometriche che si sviluppano naturalmente. Per studiare microscopicamente la curvatura dell'interfaccia liquido-solido, è stata progettata e costruita una camera, nella quale sono stati realizzati i test.

È stato introdotto un parametro che rappresenta la curvatura media del menisco di liquido al fine di confrontare i risultati e analizzare l'effetto delle pareti laterali della camera e della quantità iniettata di ottano sulla forma del menisco e sullo spessore di liquido.

L'obiettivo di questo progetto di tesi è di verificare sperimentalmente l'accuratezza e la ripetibilità dell'analisi interferometrica e della procedura di pulizia dei campioni in silicio per raggiungere risultati consistenti nelle misurazioni di curvatura.

NOMENCLATURE

Π: disjoining pressure [N/m^2]

σ_l: surface tension of liquid [N/m]

σ_{sl}: interfacial tension between liquid and solid [N/m]

σ_s: surface free energy of the solid [N/m]

K: meniscus curvature [1/m]

P_v: vapor pressure [N/m^2]

P_l: liquid pressure [N/m^2]

δ: film liquid thickness [m]

δ_0: average absorbed film thickness [m]

δ_c: critical thickness [m]

A: Hamaker constant [J]

$\rho_{N,l}$: number density of the liquid molecules [m^{-3}]

$\rho_{N,s}$: number density of the solid molecules [m^{-3}]

r: distance between the solid and liquid molecules [m]

θ: contact angle [degrees]

θ_a: apparent contact angle [degrees]

Y: healing length [m]

G: absolute gray value

$\bar{G}$: relative gray value

RL: reflectivity

G_{bare}: gray value of the bare surface

λ: wavelength of the monochromatic light in vacuum [m]

n_s: refractive index of solid

n_l: refractive index of liquid

n_v: refractive index of vapor

TABLE OF CONTENTS

1 Introduction 1
1.1 Motivation 1
1.2 Introduction to physical phenomena 2
1.2.1 Three-phase contact line 3
1.2.2 Physics of Disjoining pressure 5
1.2.3 Contact angle and Young's equation 7
1.3 Literature survey 10
1.3.1 Smooth surfaces 10
1.3.2 Structured surfaces 11
1.3.3 Theoretical models 14
1.4 Big picture of the entire project 17
1.5 Overview of the research work presented in this study 19
2 Interferometry technique 21
2.1 Thickness estimation 22
2.2 Image capture 26
3 Experimental design 29
3.1 Working fluid and sample 29
3.2 Chamber design 31
3.2.1 O-ring dimensioning 35
4 Cleaning process 37
4.1 Silicon wafer cleaning procedure 37
4.1.1 Piranha cleaning procedure 38
4.1.2 Ultrasonic cleaning procedure 40
4.1.2.1 Ultrasonic cleaning procedure A 41
4.1.2.2 Ultrasonic cleaning procedure B 43
4.1.2.3 Ultrasonic cleaning procedure C 44
4.2 Chamber cleaning procedure 45
5 Description of the experiment 47
5.1 Assembly procedure 47
5.2 Meniscus test procedure 48
6 Post data processing 53
6.1 Matlab code steps 53

6.2 Noise filtering 60
6.3 Average curvature 63
6.4 Bulk meniscus curvature estimation 65
7 Meniscus test 69
7.1 Meniscus test 1 70
7.2 Meniscus test 2 73
7.3 Meniscus test 3 75
7.4 Meniscus test 4 77
7.5 Meniscus test 5 79
7.6 Meniscus test 6 81
7.7 Meniscus test 7 85
7.8 Meniscus test 8 86
7.9 Meniscus test 9 88
7.10 Meniscus test 10 89
7.11 Meniscus test 11 92
7.12 Meniscus test 12 95
7.13 Meniscus test 13 96
7.14 Meniscus test 14 97
8 Results and discussion 99
8.1 Receding meniscus 99
8.2 Cleaning process 100
8.3 Comparison between different amount of liquid 103
8.4 Effect of chamber edge 104
8.5 Curvature comparison 107
9 Conclusions and future work 109
Acknowledgments 111
List of figures 113
List of Tables 119
References 121

1. INTRODUCTION

1.1. MOTIVATION

A variety of industrial applications such as power generation [1], solar still [2], cell cryopreservation [3], MEMS [4], micro heat pipes [5-7], and many others, rely on two-phase heat transfer processes involving boiling and call for more efficient means to prevent overheating; enhancements to the boiling process can improve the thermal performance across multiple industrial applications.

Recent studies on boiling show that a significant part of total heat transfer occurs in the thin liquid film region [8], at three phase contact line, namely solid-liquid-vapor line, the micro-region where all three phases meet.

Two phase heat transfer is affected by the wetted solid surface structure; controlling the nano-roughness allows to control the interfacial force gradients that are dominant at the contact line, and manipulations made at very small length scales, from some nanometers to a few hundred micrometers, can increase the evaporative mass flow and the microscale heat transfer, leading to discernable results at the system scale. Majority of theory related to thin film interfacial phenomena is relevant to smooth solid surfaces; despite many applications, the fundamental understanding on how surface structures affect the phase change heat transfer and which mechanisms contribute to the improvement are still not well understood.

The future development and optimization of many technologies requires a deep and thorough understanding of the physics behind the processes that occur at the solid-liquid-vapor contact line, which subsequently enables a control on the transport processes in the macro-region.

So, it is of fundamental significance and interest understanding the characteristics of the evaporation process on structured surfaces and their effect on the thin film, in order to guide structure design for improving the two-phase heat transfer. From this consideration, the design and realization of an experimental facility is required to study and analyze the

intermolecular pressure field and the liquid transport at three-phase contact line, related to different nano-structured surfaces.

1.2. INTRODUCTION TO PHYSICAL PHENOMENA

Liquid-vapor phase change is a natural phenomenon driven by the difference in temperatures of liquid and vapor phase and non-isothermal conditions lead to either condensation or evaporation depending on the respective temperature difference of the two phases.

Considering a nucleated bubble from a heated solid surface, as shown in Figure 1.1, or a partially wetting fluid rested on a solid surface forming a drop with a macroscopic convex profile, looking at the microscopic region, at the three-phase contact line, defined as the region where the film thickness is lower than about $\delta \sim 0.1$ μm, a liquid meniscus with a concave shape appears, schematically drawn in Figure 1.2. For a completely wetting fluid, the liquid meniscus is visualized near a solid sidewall, since it spreads entirely on a horizontal surface and forms a flat film.

Figure 1.1: Nucleate bubble [40]

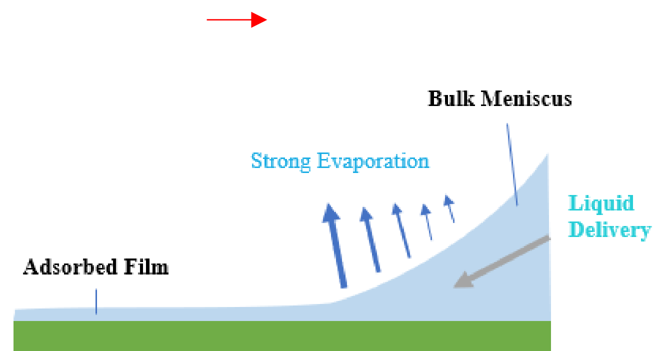

Figure 1.2: Thin liquid film region of nucleated bubble

At three-phase contact line region, the interfacial forces depend on the surface energies of the solid and the liquid phases; whenever a completely wetting or a partially wetting liquid comes in contact with a solid substrate, an extended meniscus is formed and the resulting laws of thermodynamics are different from those for a flat boundary: curvature

of the liquid-vapor interface and intermolecular attractions between solid and liquid molecules determine the shape of the meniscus (for isothermal condition) and control the transport processes and the flow to replenish liquid in the evaporating region (for non-isothermal condition).

1.2.1. THREE-PHASE CONTACT LINE

The heat transfer process in the micro-region can be visualized in terms of three resistances in series: the conduction resistance through the solid substrate, and it can be small owing to the high conductivity of the solid material; the conduction resistance through the liquid that changes with the thickness of the liquid film, increasing with it; and, finally, the liquid-vapor interfacial heat transfer resistance that depends on the strength of the intermolecular forces.

The liquid meniscus is traditionally divided in three zones:

- The bulk meniscus region, also called intrinsic meniscus region, governed principally by surface tension forces, where the curvature of the liquid-vapor interface becomes nearly constant and the conduction resistance is high due to the relatively thick liquid film.
- The adsorbed film region, where intermolecular forces predominate over surface forces and the liquid-vapor interfacial resistance is the strongest thermal resistance. This flat region is also called non-evaporating region because the overall thermal resistance is effectively infinite since there is no evaporation.
- The transition region, a zone bridging these two, also called evaporating thin film region, where the liquid-vapor interface has the biggest curvature, the small film thickness offers only moderate conduction resistance while the interfacial resistance and the attractive forces decreases compared to the adsorbed film region due to the increasing thickness; this film thickness range is several multiples of the adsorbed film thickness. Since the thermal resistance to phase

change is lowest, the heat flux reaches a maximum and extending the transition region should enhance the evaporative mass flow.

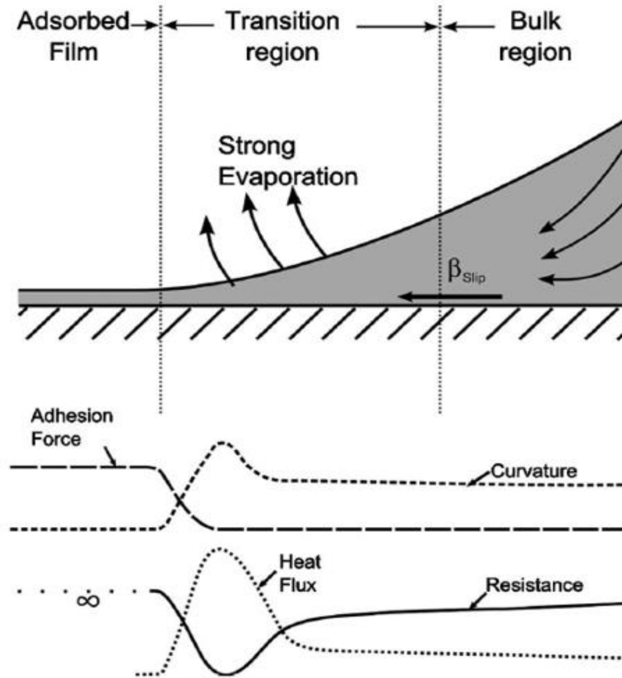

Figure 1.3: Schematic of a completely wetting meniscus; variation in adhesion force, curvature, heat flux, and thermal resistance in the contact line region of the evaporating meniscus. [21]

The microscale transport process and the meniscus stress field are governed by the Modified Young-Laplace Equation:

$$P_v - P_l = K\sigma_l + \Pi(\delta)$$

(1.1)

Where σ_l is the surface tension of the liquid, δ is the thickness of the liquid film, K is curvature of liquid-vapor interface and Π is the disjoining pressure. The pressure difference between liquid and vapor depends on capillary pressure K σ_l, affected by film curvature, and on disjoining pressure, affected by molecular attraction, namely by attractive and adhesion forces between the solid and the liquid.

Disjoining pressure is a result of the long-range solid-liquid intermolecular forces and it increases rapidly with decreasing film thickness and fully suppresses evaporation in the

adsorbed film region; it is the excess pressure required for liquid molecules to escape from the evaporating thin film. The thickness variation of the evaporating meniscus leads to a strong disjoining pressure gradient, which together with the capillary pressure gradient, drives the liquid flow from the intrinsic meniscus to the evaporating thin film to maintain the high heat flux. The bulk meniscus region acts as the reservoir that replenishes fluid to the transition region, where both forces are active and most evaporation occurs.

1.2.2. PHYSICS OF DISJOINING PRESSURE

The disjoining pressure describes the relative strength of adhesive versus cohesive forces, as a result of Van der Waals interactions, in particular of London dispersion forces.
The cohesive forces are the intermolecular forces, such as those from hydrogen bonding and Van der Waals forces, which cause a tendency in liquids to resist separation; these attractive forces exist between molecules of the same substance. The adhesive forces are the attractive forces between unlike molecules; they are caused by forces acting between two substances, such as mechanical forces (sticking together) and electrostatic forces (attraction due to opposing charges).
The Van der Waals interactions arise from the Lennard-Jones potential, which is a function of the distance between the centers of two particles and describes the interaction between a pair of neutral atoms or molecules. The short-range term (positive potential) refers to the repulsive forces due to overlapping electron orbitals (Pauli repulsion); the long-range term (negative potential) describes the attractive forces (Van der Waals forces); the distance between their centers is the separation distance at which the minimum potential energy is reached.
Intermolecular forces of Van Der Waals have three major contributions: (1) the Keesom forces (permanent dipole-permanent dipole interactions), attractive or repulsive electrostatic interactions between permanent charges (in the case of molecular ions) and in general between permanent multipoles; (2) the Debye forces (permanent dipole-induced dipole interactions, also known as polarization or induction) which are the attractive interactions between a permanent multipole on one molecule with an induced

multipole on another; (3) the London dispersion forces (induced dipole-induced dipole interactions) which are the temporary attractive interactions between instantaneous multipoles and the weakest intermolecular long-range forces, that vary inversely with the film thickness. The London dispersion forces are always present and control the transport processes in thin liquid-solid films.

The disjoining pressure of a thin liquid film on solid surfaces arises from the long-range intermolecular forces between the liquid and solid molecules. For a Lennard-Jones type potential, the long-range interaction is given as:

$$\Phi(r) = -\frac{A}{\pi^2 * \ \rho_{N,l} * \rho_{N,s}} * r^{-6}$$

(1.2)

Where r is the distance between the solid and liquid molecules, $\rho_{N,l}$ and $\rho_{N,s}$ the number density of the liquid and solid molecules, respectively, and A is the Hamaker constant. By integrating the solid-liquid potential, the disjoining pressure profile of a thin liquid film is calculated as:

$$\Pi_{int}(x, y) = -\int_{-\infty}^{+\infty} \int_{-\infty}^{+\infty} \int_{\delta(x,y)}^{+\infty} \rho_{N,l}\, \rho_{N,s}\, \Phi(x, y, z)\, dz\, dy\, dx$$

(1.3)

For a thin liquid film on a planar atomically smooth surface, the thickness profile is uniform along the surface, namely $\delta(x, y) \equiv \delta$, and the Equation of solid-liquid potential is simplified to the classical disjoining pressure model, that predicts disjoining pressure as the inverse cubic function of absorbed film thickness:

$$\Pi = \frac{A}{6\pi\, \delta^3}$$

(1.4)

The Hamaker constant A, that characterizes the strength of the solid-liquid interactions and it is function of liquid and solid properties and physical characteristics of the system

is described by Lifshitz theory, for smooth surfaces, and it is function of Boltzmann's constant, temperature, Planck's constant, plasma frequency of the free electron gas, refractive index and dielectric constant. The Lifshitz theory takes into account the influence of neighboring molecules on the interaction between every pair of molecules located in the two bodies with consideration of the dielectric properties of this intervening medium, rather than the Hamaker's method defined for a Van der Waals body–body interaction, that treats each pair of molecules completely independently of their surroundings and ignoring the influence of an intervening medium between the two particles of interaction.

The sign of the Hamaker constant is conventionally negative for a completely wetting fluid ($A<0$).

1.2.3. Contact angle and Young's equation

A partially wetting fluid is a fluid with a contact angle value less than 90 degrees; a completely wetting fluid has a contact angle of 0 degrees, and it is characterized by a very strong interaction between solid and liquid molecules and a negligible week interaction between liquid molecules themselves. A solid with a high energy surface has strong chemical bonds that hold the solid molecules together, such as metallic bonds for metals, and allows most molecular liquids to achieve complete wetting; whereas, solids with a low energy surface are held together by weak forces, such as van der Waals bonds, and they can permit either complete or partial wetting.
According to Young's equation, there is a relationship between the contact angle θ, the surface tension of the liquid σ_l (surface energy between liquid and gas), the interfacial tension σ_{sl} between liquid and solid (surface energy between solid and liquid) and the surface free energy σ_s of the solid (surface energy between solid and solid):

$$\sigma_s = \sigma_{sl} + \sigma_l * \cos\theta$$

(1.15)

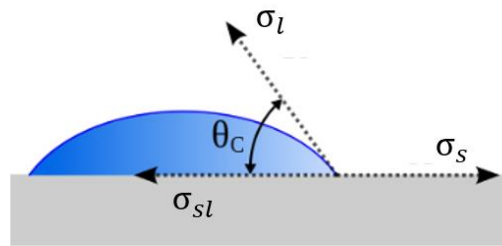

Figure 1.4: Schematic of a liquid drop showing the quantities in the Young's equation

Wenzel proposed a modified Young's equation showing the relation between the apparent contact angle of a liquid on a rough surface θ_a and the roughness factor of the solid surface r, given by:

$$\cos \theta_a = r * \cos \theta$$

(1.6)

The roughness factor r is defined as the ratio between the actual surface and the geometric surface. On wetting surfaces ($\theta < 90°$) the liquid-solid interface, the apparent contact angle decreases on a rough surface (with increased of r) and the consequent decreasing of liquid-solid interfacial energy favors more spreading; on non-wetting surfaces ($\theta > 90°$), the reverse is true, and the apparent contact angle increases with increasing roughness.

For example, as shown in Figure 1.5, the liquid with lower contact angle has a longer transition region (L), thus providing larger area for evaporation, since the height above which the conductive resistance in the fluid becomes formidable (h) starts later.

Changing the physical properties of the liquid–vapor–solid system can alter the contact angle and moreover the liquid transport process and the pressure field.

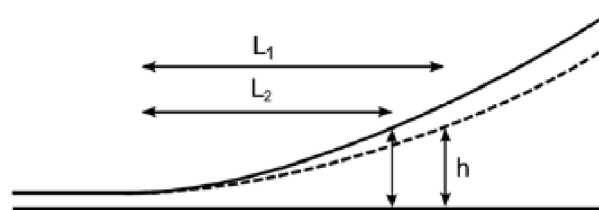

Figure 1.5: An increase in wetting (decrease in contact angle) results in an increased area for evaporation [41]

The capillary pressure and the surface tension forces associated with the liquid oppose the effects of surface roughness and lead to a smoother vapor-liquid interface; whereas the disjoining pressure attempts to maintain a conformal film thickness over the roughness features. Thus, for very thin liquid films disjoining pressure competes successfully with the surface tension forces that try to smooth the liquid-vapor interface; surface tension dominates as the film thickness increases and the liquid-vapor interface becomes smooth.

Wenzel State occurs when liquid penetrates all surface features; Cassie-Baxter State occurs when vapor occupies the interstices of the surface texture.

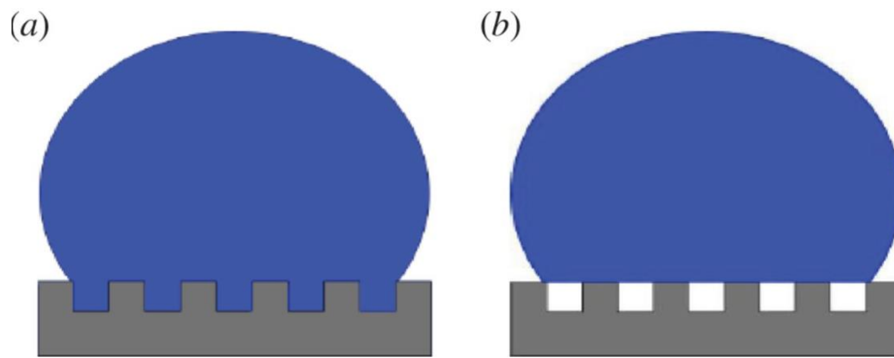

Figure 1.6: schematic of a liquid drop on the rough solid surface. (a) Wenzel model; (b) Cassie-Baxter model [42]

Robbins et al. [9] and Leger and Joanny [10] has been introduced a "healing length", Y, which characterizes the competition between the surface tension and disjoining pressure. Their relationship is valid when the amplitude of roughness is small such that the disjoining pressure due to an average thickness on the rough surface is equal to the local disjoining pressure generated due to roughness amplitude. Y is given by:

$$Y = \frac{\delta_0^2}{\sqrt{\frac{A}{2\pi\,\sigma_l}}}$$

(1.7)

Where δ_0 is the average absorbed film thickness.

When the wavelength of roughness is smaller than Y, the capillary pressure dominates, and the vapor-liquid interface remains flat; on the contrary, when the wavelength of roughness is larger, the disjoining pressure dominates, and the liquid interface follows the roughness of solid surface, since and surface tension plays a negligible role.

Another related parameter has been defined by Palasantzas [11] as the critical thickness, δ_c, or the thickness of the liquid film above which the fluctuations due to the solid roughness fall off.

1.3. LITERATURE SURVEY

1.3.1. SMOOTH SURFACES

The pressure field within the liquid has been experimentally obtained in several studies from the measurement of the interfacial parameters such as the film thickness profiles and the meniscus curvature. The sensitivity of the film thickness (especially in the adsorbed region) and the importance of the shape of the profile as an indicator of the intermolecular force field have been discussed in detail in a large number of related publications.
The augmented Young-Laplace model, which included the concept of disjoining pressure for the interfacial force field characterization of a thin film, together with an interferometry technique, were used by Wayner and co-workers [12-17] to study the contact line region of an evaporating, wetting meniscus.
Extensive experimental studies have been performed to characterize the thickness profile and the heat transfer performance of thin film evaporation. The thickness profile of the evaporating thin film can be directly measured using interferometry [18-21] and reflectometry [20].

Potash et al. [22] developed a model to describe the transport processes occurring in a completely wetting extended evaporating meniscus and calculated the pressure gradient for the flow towards the contact line region; they derived the thickness profile and heat

transfer rate based on the balance between evaporation and liquid flow driven by capillary and disjoining pressure. Moosman and Homsy [23] modeled the transport process in the contact line region of an evaporating wetting meniscus and demonstrated a high heat flux in the contact line region. Truong and Wayner [24] modeled the microscopic region of an equilibrium wetting liquid meniscus based on the sum of the hydrostatic force, capillarity and Van der Waals forces with the boundary conditions of zero curvature and zero contact angle in the adsorbed film region. Gee et al. [25] investigated the surface forces of thin liquid films of alkanes adsorbed on a quartz surface by ellipsometric measurements of the film thickness as a function of the disjoining pressure. DasGupta et al. [19] experimentally measured the isothermal profiles of extended meniscus of alkanes on a quartz surface using an interferometry technique and found that the augmented Young-Laplace equation is an excellent model for explaining the force field at the liquid-vapor interface.

Despite their proven success, these models did not properly account for the effect of surface structures on disjoining pressure, the key of the heat transfer characteristics of thin film evaporation.

1.3.2. STRUCTURED SURFACES

For thin film evaporation on structured surfaces, the disjoining pressure and the flow characteristics are affected by surface structures, which will, in turn, affect the thickness profile and the heat transfer rate of the evaporating thin film. Heat transfer can be increased with a larger transition region by increasing the wetting through mechanical modification of the solid surface. Thus, patterning a surface either chemically or physically alters three interrelated phenomena that can affect a phase change process, namely the surface potential, the shape of the liquid-vapor interface and the resulting fluid flow.

The size and scale of the surface features determine which solid/liquid/vapor interactions are important. Macro-sized, physical structures primarily serve to increase the contact area between the heat transfer fluid and the underlying solid. Micro-sized features lead to

a similar increase in solid-liquid interfacial area but also increase nucleation sites for enhancing condensation or boiling. Finally, sub-micron, nano-sized structures increase the surface potential, varying the adsorbed film thickness and the disjoining pressure, and can also lead to an increase in nucleation sites and interfacial area.

Experimental results and observations from naturally occurring systems both point to the need for a hierarchical surface structure to achieve maximum performance in phase-change processes.

Recent studies show that the experimental Hamaker constant is larger on rough surfaces than on smooth ones (theoretical value) [21]. Ojha et al. found that increasing surface roughness leads to enhanced disjoining pressure effect, resulting in a flatter meniscus, an extended evaporating region and improved heat transfer performance.

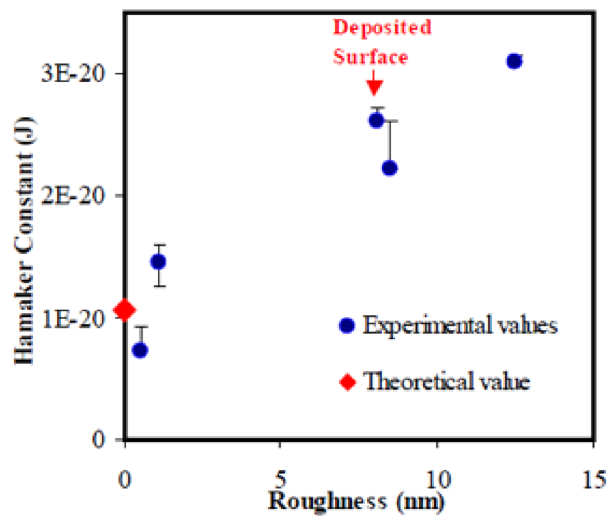

Figure 1.7: Experimental and theoretical Hamaker constant on all surfaces [41]

However, the experimental constant was different on structured surfaces with the same value of average roughness. Thus, roughness alone does not completely explain the wetting behavior and the behavior of the Hamaker constant on these surfaces.

Butt et al. [26] has proposed a method to calculate the capillary pressure on rough surfaces. Sweeny et al. [27] studied the capillary pressure in thin films on idealized rough surfaces. They solved the augmented Young-Laplace equation for one-dimensional and

two-dimensional periodic solid surfaces by employing a finite element approach. Their results show that on a rough surface, the capillary effect in a thin film is low for strongly wetting films. However, the capillary effect is prominent as the liquid becomes less wetting and the adsorbed film thickness decreases. Honda and Wei [28] studied the interactions between the solid and the liquid phase on the macro- and micro-scale features; they concluded that surface roughness of any type enhances nucleate boiling, as also surface cavities and microporous structures. The evaporative heat transfer performance of macro-sized, 3D internally finned heat pipes has been studied by Liao et al. [29]. The introduction of such macro-sized fins increases the heat transfer coefficient for condensation and evaporation. The resulting decrease in thermal resistance is due to two factors: an increase in the surface area due to the incorporation of the fins and an increase in nucleation sites due to surface nonuniformities. They also found that at higher heat fluxes, the area available on finned surfaces decreases and the original advantage the finned surface showed disappears due to formation of a continuous liquid film that covers the area. At the nanoscale, the findings of Kubo et al. [30] and Anderson and Davis [31] indicate that surface roughness is effective in enhancing nucleate boiling however, they also found that the trend is not directly related to the RMS (root mean squared) roughness of the surface. At the nano-scale, the role of intermolecular forces between the surface irregularities and the liquid becomes prominent, and the surface potential and subsequent intermolecular interactions are not only a function of the RMS roughness but are also dependent on other surface features like the correlation length, ξ, and roughness exponent, H. The enhancement of the evaporative heat flux by means of a combination of chemical and microscale physical modification has been shown by Takata, Hidaka et al. [32]. The effect of micro-sized patterns on the motion of the contact line of a drop during evaporation was studied by McHale et al. [33]. The use of structured wetting surfaces to promote evaporation and condensation processes mimicks natural control surfaces such as those found in lotus leaves by Cheng and Rodak. [34].

Thus, experimental studies showed that surface structures affect two phase heat transfer, but quantitative correlations between roughness features and thin film evaporation performance are not yet available and the enhancement mechanisms are still not well understood; the exploitation of such surfaces for heat and mass transfer applications by utilizing the underlying physics has just begun.

The effective Hamaker constant method is a simple empirical description of disjoining pressure on structured surfaces, which assumes that surface structures only affect the magnitude of the Hamaker constant rather than the inverse cubic relation between disjoining pressure and film thickness. However, there is not solid evidence that the inverse cubic relation is still valid for structured surfaces; the roughness alone does not completely explain the behavior of Hamaker constant on structured surfaces, how is related to the them and what are the physical phenomena involved are still to be clarified and demonstrated.

1.3.3. THEORETICAL MODELS

While a simple expression of disjoining pressure is not always obtainable for structured surfaces, the Equation of solid-liquid potential (3) can still be numerically solved to predict the disjoining pressure profile. The integration method leads to an accurate calculation of the disjoining pressure provided that the solid-liquid potential is precise. However, this calculation requires the solution of a double integral, which is not convenient to be lumped into the thin film evaporation model.

Theoretical models for disjoining pressure on structured surfaces have been developed based on Derjaguin approximation [35, 36], whereas the validity of these approximations on different surface structures has not been demonstrated.

As for a thin liquid film on a two-dimensional structured surface with a known surface profile Z(x), the film thickness varies along the surface. For example, assuming a flat meniscus (a), the thickness profile is $\delta(x) = \delta_0 - Z(x)$, where δ_0 is the mean film thickness defined as $\delta_0 = \frac{1}{L}\int_{-L/2}^{L/2} \delta(x)dx$.

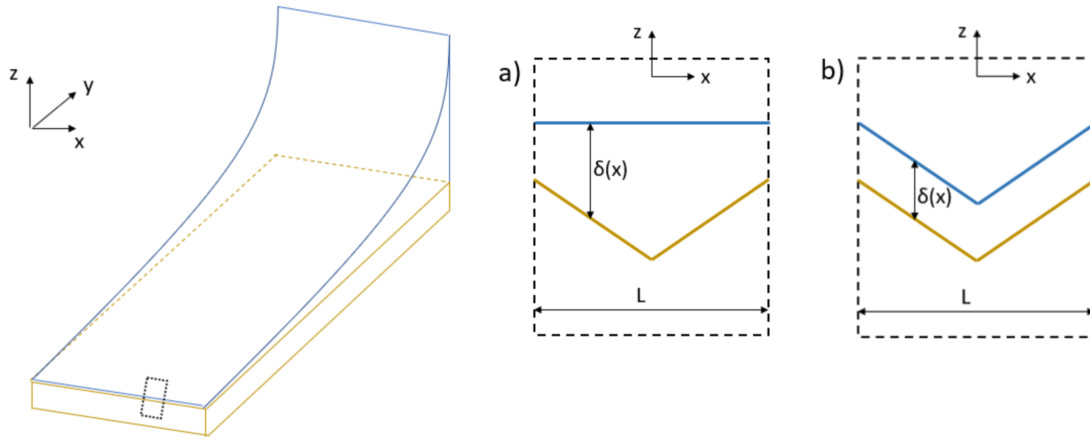

Figure 1.8: Schematic drawing of an extended meniscus on a rough surface (left); cross-sectional view of a V-groove structure (right) with a flat meniscus (a) and a conformal meniscus (b)

Derjaguin approximation is an accurate prediction of disjoining pressure based on flat liquid-vapor meniscus, for which the local solid-liquid interaction of a curved surface can be approximated by that of a planar surface with the same local thickness.

$$\Pi_{rough}^{Der}(\mathrm{x}) = \frac{A}{6\pi\,\delta^3(x)}$$

(1.8)

It gives the disjoining pressure profile along the x-axis; the mean disjoining pressure is calculated by averaging the disjoining pressure of the thin film.

$$\overline{\Pi_{rough}} = \frac{1}{L}\int_{-L/2}^{L/2} \Pi_{rough}(x)\,dx$$

(1.9)

The liquid meniscus shape is assumed to be a flat profile, namely: $\zeta(x) \equiv \delta_0$

For non-flat liquid-vapor meniscus (b), the thickness profile is defined with the meniscus shape $\zeta(x)$ as $\delta(x) = \zeta(x) - Z(x)$, and is substituted into Equation (8) and (9) to calculate disjoining pressure. The meniscus shape models require the implicit solution of simultaneous integral equations and the Derjaguin approximation becomes too complicated to be lumped into the thin film evaporation model.

In order to have a simple expression for calculating disjoining pressure, several fitting equations of disjoining pressure have been proposed in literature.

A meniscus shape model based on minimizing system free energy is being performed to capture the exact influence of roughness features and to take into account properly the effect of surface structures on disjoining pressure and flow permeability, which has been demonstrated may be significant reduced due to nanoscale surface roughness.

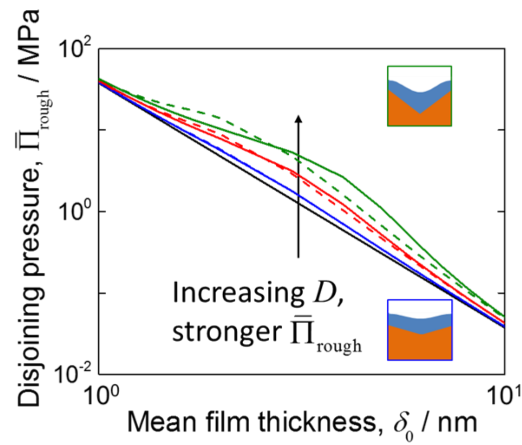

Figure 1.9: Model prediction of disjoining pressure on structured surfaces

The model shows that disjoining pressure on structured surfaces is not a linear curve in the logarithm plot with thickness, as it is for flat surfaces. Experiments are needed to validate the model and demonstrate the theoretical work.

1.4. BIG PICTURE OF THE ENTIRE PROJECT

The long-term objective of this project is to investigate how surface roughness affects processes at three-phase contact line, a key feature in boiling and evaporation, experimentally evaluating how one force acting on the liquid film, disjoining pressure, changes with film thickness and surface roughness; an experimental study to confirm meniscus shape model is desired.

The final goal of the entire work is to find a physical relation between solid surface roughness and disjoining pressure; an experimental curve which shows the disjoining pressure function of adsorbed film thickness $\prod = f(\delta)$ for different nano-structured surfaces has to be built, and subsequently compare with the theoretical model.

The experimental measurements are performed in isothermal condition. In this condition, when the pressure in gas and liquid phase is constant, the disjoining pressure in the adsorbed film region is roughly equal to the capillary pressure in the bulk meniscus region, since the disjoining pressure in the bulk meniscus is negligible due to the high thickness, as the capillary pressure in the adsorbed film region due to the null curvature.

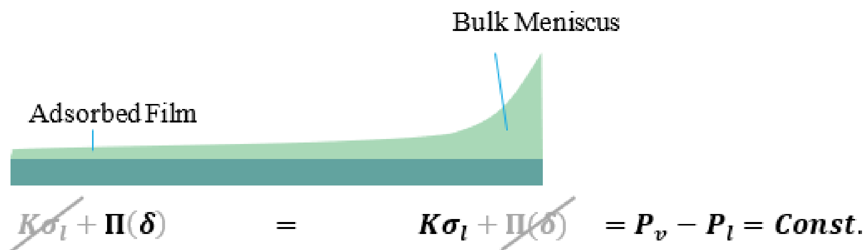

$$K\sigma_l + \Pi(\delta) = K\sigma_l + \Pi(\delta) = P_v - P_l = Const.$$

Figure 1.10: Schematic of three phase contact line region at isothermal condition

The characterization of disjoining pressure requires the use of two reflectivity technique: the interferometry technique, detailed reported in the present work, and the ellipsometry technique.

By using the interferometry technique, the thickness profile and the curvature in the bulk meniscus region can be obtained. Knowing the surface tension of the working liquid, the capillary pressure is calculated and so implicitly the disjoining pressure value.

Using the ellipsometry technique, the adsorbed film thickness is measured; this technique allows calculation of absolute film thickness by varying polarization states of a beam of light, and it is based on the interference behavior from the reflections at film surface and substrate surface. By scanning across multiple polarization angles for the incoming light, netting multiple measured points for a single film thickness, the absolute film thickness of a single spot can be measured.

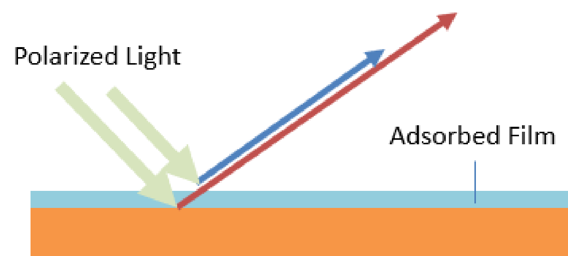

Figure 1.11: Polarized light reflection in ellipsometry technique

Thus, experimental value of both disjoining pressure and adsorbed film thickness are obtained for many samples characterized with different nano-roughness, thanks to the fabrication of an experimental facility which allows the interchangeability of different structured surfaces.

In order to build an experimental curve, more than one value is required to characterize a structured surface sample. The most effective and easy way to vary the disjoining pressure is to vary the equilibrium pressure inside the facility, maintaining isothermal conditions. The modification of vapor pressure leads to a different interfacial stress field, altering the equilibrium shape and the static behavior of the extended meniscus.

Once a method to vary the equilibrium pressure has been found, the experimental curve can be built and compared with the theoretical model.

1.5. OVERVIEW OF THE RESEARCH WORK PRESENTED IN THIS STUDY

In the proposed thesis, a phisical introduction on contact line behavior is presented in Chapter (1) and a discussion of the experimental studies and theoretical models of thin liquid film on structured surfaces is reported, covering the detailed review of the relevant literature on this subject.

The interfacial parameters, namely the meniscus curvature of liquid film profile, are experimental evaluated with ease by the optical interferometry technique, whose resolution is high and enables measurements at the microscopic scale; the physical phenomena on which the technique is based are presented in Chapter (2), with the detailed description of the functional operating.

The description of the experimental facility and the detailed dimensioning and design of the chamer are discussed in Chapter (3).

Various cleaning processes were utilized, namely the Piranha cleaning and different ultrasonic cleaning procedure, and discussed in Chapter (4).

The assembly procedure and the description of the experiment are illustrated in Chapter (5); the steps of data acquisition and the MATLAB post processing are reported and explained in detail in Chapter (6), with the relative addictions to the code, and the attempts of calculation of the bulk meniscus curvature.

The performing meniscus test are presented in Chapter (7). Discussion of results are reported in Chapter (8); consistency of test and repeatability of procedures were obtained and demonstrated.

The conclusions and future works are described in Chapter (9); further studies are required to complete the entire project and reach the final goal.

2. INTERFEROMETRY TECHNIQUE

Interferometry is a technique to measure non-constant thickness of liquid film and it is used to describe the film profile in the bulk meniscus region. It is based on the interference between reflections at solid and liquid surface.

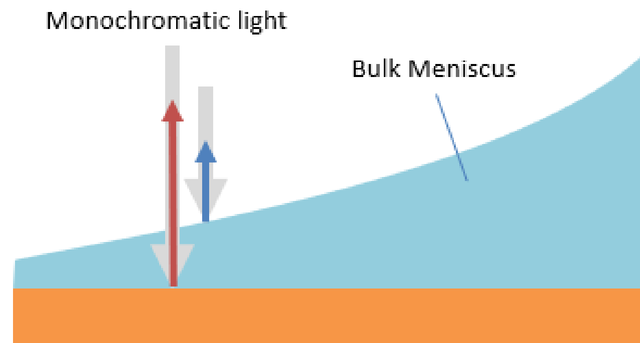

Figure 2.1: Monochromatic light reflection in interferometry technique

The interferometer provides a beam of monochromatic light from a light source; the beam hits the sample: one part is reflected by the liquid-vapor interface and one part is reflected by the solid surface. The microscope receives a beam that is the recombined superposition of the two parts of beam: an interference fringe pattern between the light that is reflected from the solid-liquid interface and liquid-vapor interface is created. The constructive interference occurs when beams are in phase, visualized as light fringes, and the destructive interference when beams are out of phase, visualized as dark fringes.

2.1. THICKNESS ESTIMATION

From the profile analysis of each image, a plot of the pixel gray value (G), versus pixel position, x, is extracted, corresponding to the dark and bright fringes of the corner meniscus. The extended meniscus is where the interferometry fringes start and the adsorbed layer ends. The adsorbed region is represented by a constant light gray value, without any fringes since it is a flat layer.

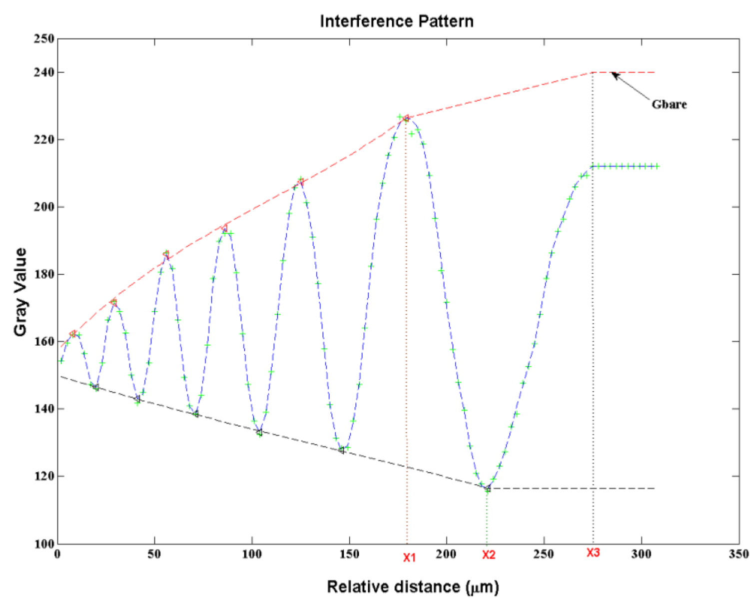

Figure 2.2: Grey value plot with the interpolatory envelop

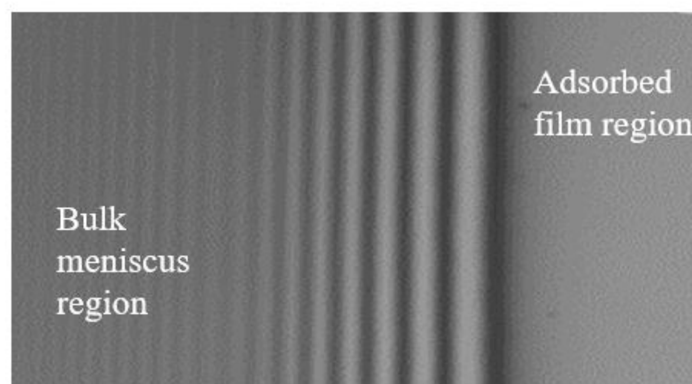

Figure 2.3: Gray scale interferometry image of naturally occurring interference fringes produced from the constantly changing thickness of the corner meniscus

The wavelength, namely the reciprocal of the frequency, is function of film thickness and increases with decreasing of it; in the adsorbed film this distance is infinity and thickness is assumed to be zero. Faster is the increasing of thickness, faster is the changing of the gray value plot and smaller is this distance, which results in a higher frequency. Thus, the frequency of the waves is an indicator of the film curvature: lower frequency means flatter profile. Whereas the amplitude of the waves is an indicator of the black and white contrast: lower amplitude means more uniform color and harder distinction between dark and bright fringes.

The grey value of pixel is a measure of reflectivity, which changes with film thickness, namely with the distance between liquid film surface and solid surface of the sample; the variation of thickness leads to a variation of superposition of beams, which causes a variation of the final resulting beam, which means a variation of reflectivity and a variation of the gray value of pixel.

The code scanned the peaks and valleys and calculated a relative gray value $\overline{G}(x)$ with respect to the interpolated envelopes at each pixel position, y, based on the following relation:

$$\bar{G}(x) = \frac{G(x) - G_{min}(x)}{G_{max}(x) - G_{min}(x)}$$

(2.1)

Where, $G_{min}(x)$ and $G_{max}(x)$ are determined from the interpolated envelopes to the various order minima and maxima, drawn by fitting the respective maxima and minima with polynomials of third order, up to x_1 (location of the first bright fringe) for $G_{max}(x)$ and up to x_2 (location of the first dark fringe) for $G_{min}(x)$. It is found that for most of the data, a third order spline fit is sufficient to fit these envelopes and the evaluated film thickness profiles are independent for higher orders of this polynomial. The value of $G_{min}(x)$ for positions prior to the first dark fringe is taken to be the value $G(x_2)$ at the first dark fringe. The value of $G_{max}(x)$ in the adsorbed flat film region is taken to be equal to the measured gray value G_{bare} of the bare surface. G_{bare} value corresponds to zero film thickness. A linear interpolation is used to connect the gray value $G(x_1)$ of the first

bright fringe and this value of G_{bare} at the beginning of the adsorbed section. The constant gray value in the flat adsorbed film region is G_0.

Film thickness is evaluated from the relative gray value, $\overline{G}(x)$, and reflectivity, RL, by using the following relation:

$$RL(x) = \bar{G}(x)[RL_{max} - RL_{min}] + RL_{min}$$

(2.2)

Since the gray value at each pixel location is known from the experimental data, the reflectivity of the liquid film at each pixel position can be determined.

The reflectivity of a thin liquid film on a solid surface is the basic relation that is used to connect the film thickness δ with the gray values and other parameters, such as λ, the wavelength of the monochromatic light in vacuum, n_s, n_l and n_v, respectively the refractive index of solid, liquid and vapor (vapor phase of liquid film), and it is provided in Equation 2.3:

$$RL\ (Reflectivity) = \frac{\alpha + \beta \cos 2\Theta}{k + \beta \cos 2\Theta}$$

(2.3)

Where,

$\Theta = \frac{2\,\pi\,n_l\,\delta}{\lambda}$ $\qquad \alpha = r_1^2 + r_2^2$ $\qquad \beta = 2\,r_1 r_2$

$k = 1 + r_1^2\,r_2^2$ $\qquad r_1 = \frac{n_l - n_v}{n_l + n_v}$ $\qquad r_2 = \frac{n_s - n_l}{n_s + n_l}$

The equation shows that the reflectivity changes cyclically with the minima and maxima according to:

$$RL_{max} = \left(\frac{r_1+r_2}{1+r_1 r_2}\right)^2 = \frac{\alpha+\beta}{k+\beta};\ \ \Theta = 0,\ \ m\pi$$

$$RL_{min} = \left(\frac{r_1-r_2}{1-r_1 r_2}\right)^2 = \frac{\alpha-\beta}{k-\beta};\ \ \Theta = \frac{\pi}{2},\ \left(m + \frac{1}{2}\right)\pi$$

From which the film thickness at every peak and valley can be found by knowing the order of fringes m ($m = 0$ for the first dark fringe x_2 and for the first bright fringe x_1):

$\Theta = \frac{2\pi n_l \delta}{\lambda} = m\pi,$ from which: $\delta = \frac{m\,\lambda}{2\,n_l}$

$\Theta = \frac{2\pi n_l \delta}{\lambda} = \left(\frac{1}{2} + m\right)\pi,$ from which: $\delta = \frac{\lambda}{2n_l}\left(\frac{1}{2} + m\right)$

Combining equation (2.3) and equation (2.2), the film thickness at each pixel location is related to the gray value at that pixel location according to the following equation (2.4):

$$2\Theta = cos^{-1}\left\{\frac{\beta + k\,[1 - 2\bar{G}(x)]}{\beta\,[2\bar{G}(x) - 1] - k}\right\}$$

(2.4)

Once the angle Θ was known, the film thickness at each pixel location is calculated using the following relations:

for destructive interference (negative slope):

$$\Theta = \pi\left(\frac{2\,n_l\,\delta}{\lambda} - m\right); \qquad \delta = \frac{\lambda}{2\,n_l}\left(m + \frac{\Theta}{\pi}\right)$$

for constructive interference (positive slope):

$$\Theta = \pi\left(m + 1 - \frac{2\,n_l\,\delta}{\lambda}\right); \qquad \delta = \frac{\lambda}{2\,n_l}\left(m + 1 - \frac{\Theta}{\pi}\right)$$

Thus, the film thickness at each pixel location is obtained based entirely on the experimental data.

2.2. IMAGE CAPTURE

Monochromatic light of wavelength λ=546 nm is used to illuminate the film covered silicon surface.

To relate the local film thickness with the local light intensity, each image is digitized into 2559 (horizontal) × 1919 (vertical) pixels, which act as individual light sensors, and is assigned a gray value between 0 (black) and 255 (white).

Each pixel of the digitized image represents the average reflectivity of a region of 0.44 μm diameter (200μm/454pixels) and 0.87 μm diameter (500μm/572pixels) for the magnification and camera settings used in these experiments (10x objective and 5x objective).

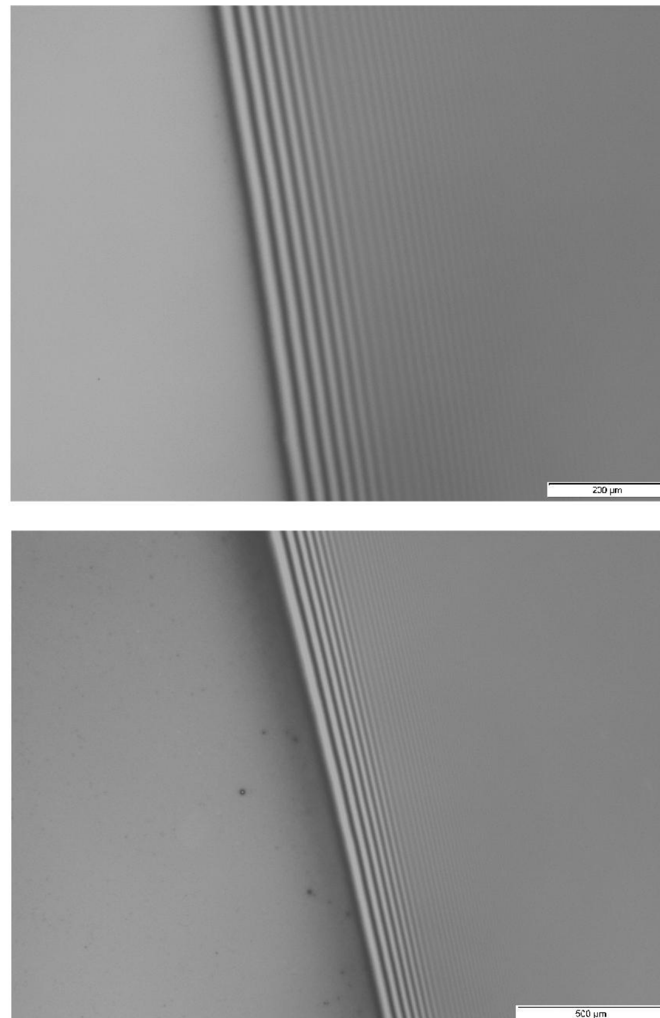

Figure 2.4: Gray scale interferometry image of extended meniscus; 10x objective (top); 5x objective (bottom)

Gray values of the digitized images are a measure of the reflectivity, and they are used to evaluate the film thickness profiles of a liquid meniscus on top of a substrate, its slope, and curvature profiles, by using a computer program written in MATLAB.

The computer program scanned the peaks and valleys and filtered the noise. It then interpolated peak-valley envelopes and by analyzing the relative reflectivity of any pixel with respect to these (dark and light pixel envelopes) determined a film thickness at every pixel. The description of the MATLAB processing is reported in detail in Chapter (6).

3. EXPERIMENTAL DESIGN

3.1. WORKING FLUID AND SAMPLE

In this study, an experimental system is designed. A closed chamber is devised by filling a micro channel with the desire liquid whose top is covered with a transparent solid surface.

The working fluid is octane, since it has a low vapor pressure so that it does not evaporate fast and it has also a low surface tension that makes it a wetting liquid.

Octane is a hydrocarbon, an organic compound consisting entirely of carbon and hydrogen atoms; it is an alkane with 8 carbon atoms in longest continuous chain. The chemical formula is $C_8 H_{18}$. It is a non-polar molecule, so it is not soluble in water, which is a polar solvent.

Properties	Value	Unit of measurement
Chemical formula	C8H18	-
Molar mass	114.23	g/mol
Vapor pressure at 20°C	1470	Pa*s
Density	703	Kg/m3
Boiling point	126	°C
Surface tension	21.1	dynes/cm
Specific enthalpy	301	kJ/Kg
Dynamic viscosity	508	Pa*s
Refractive index	1.398	-
Dielectric constant	1.95	-

Table 3.1: Physical properties of octane

The working sample is a silicon wafer, since it meets well the requirements for the interferometry technique: high reflectivity and high surface energy. It is a P-type semiconductor, doped with Boron; due to the very small thickness, it is weak and must be handles carefully during the assembly and cleaning procedure with the appropriate instrument.

Properties	Value	Unit of measurement
Diameter	50.8	mm
Thickness	350	µm
Crystalline orientation	100	-
Type	P	-
Refractive index	3.673	-
Surface energy	2512	mJ/m2
Density	2330	Kg/m3
Dielectric constant	11.7	-
Melting point	1414	°C

Table 3.2: Properties and dimensions of silicon wafer

3.2. CHAMBER DESIGN

In order to perform the experimental test, the facility has to meet some requirements:

- It has to be filled with the working liquid, thus it must provide for a very small channel or micro-hole
- It has to be small enough for microscope observation and compatible with interferometry technique (in future also with ellipsometry technique)
- It has to ensure the focal distance of 6 mm (distance from the visualization window to the sample surface), required by the microscopy
- It has to allow for changing samples and for cleaning of each component, namely it has to enabled for assembling and disassembling.

A similar experimental chamber has been designed by Monojit et. al [37], to study the equilibrium and dynamic electrowetting behavior of ultrathin liquid films of surfactant laden water over a silicon substrate, using image analyzing interferometry.

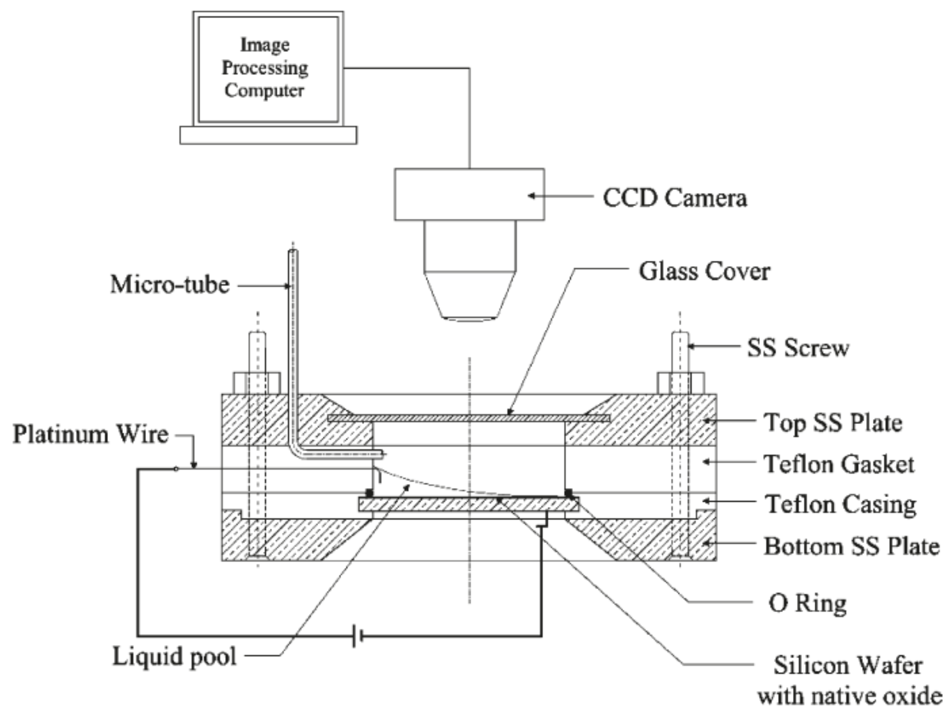

Figure 3.1: Schematic of the experimental setup with cross sectional view of Monojit et al. [37]

The chamber built for this study starts from this comparable design; some necessary changes have been made to meet mechanical and manufacturing requirements, namely:

- Instead of two separate Teflon parts, only the Telfon gasket has been included between the two stainless steel plates
- Instead of the 90-degrees bent micro-tube, a horizontal micro hole has been carved in the Teflon part, to facilitate the manual filling with the aid of a syringe
- The bottom stainless steel plate has been made a circular unpierced plate, directly provided with the thin groove for the wafer
- Two dowel pins have been added, to further support and align the parts concentrically
- The glass cover has been glued below the top plate base to facilitate the manufacturing and the assembly

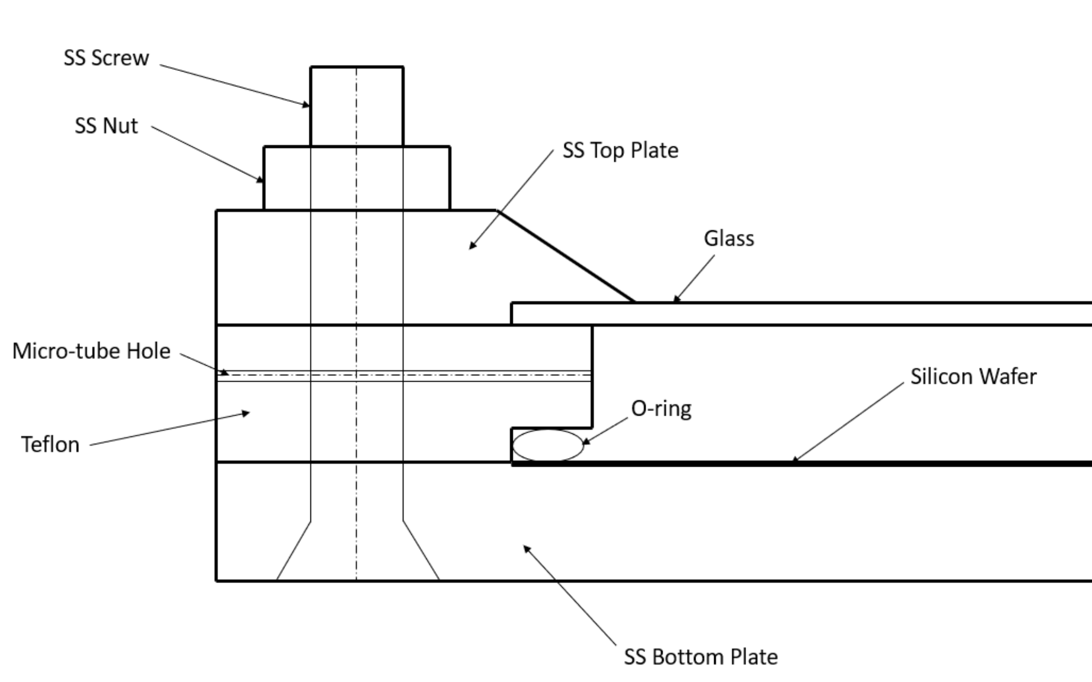

Figure 3.2: Schematic of half cross sectional view of the chamber, with indication of components

The experimental facility has been designed with the aid of Solidworks and manufactured by the precision machining laboratory of Purdue University, using milling, profiling and turning; the machine tools ensure a tollerance fabrication of 0.0025 mm, more than acceptable for our purpose.

The Chamber of 38.1x16 mm dimensions consists of the bottom base assembly and the top cover with the Teflon gasket in between. The base assembly of 5 mm thick is essentially a circular plate in 303 stainless steel, etched with a circular groove of 50.8 mm diameter to place the sample. On the top of it, the 6 mm thick Teflon annular gasket is placed; an O-ring fills the space between the Teflon part and the wafer to seal the system, prevent the leak of fluid, isolate the liquid film and avoid the direct contact between the sample and the Teflon part. The O-ring choice and the groove dimensioning is presented in more detail in the following paragraph. The top cover in 303 stainless steel is provided with an optically flat glass window of 1 mm thickness for viewing the meniscus from the top and for optical measurements; the annular top plate is 5 mm thick with a trapezoidal cross section. The glass disk is glued on the steel with a cyanoacrylate super glue, such as to chemically resist to organic solvent and aggressive solution for the cleaning part. A micro channel of 0.5 mm diameter is etched inside the Teflon gasket, 4 mm from the base of it.

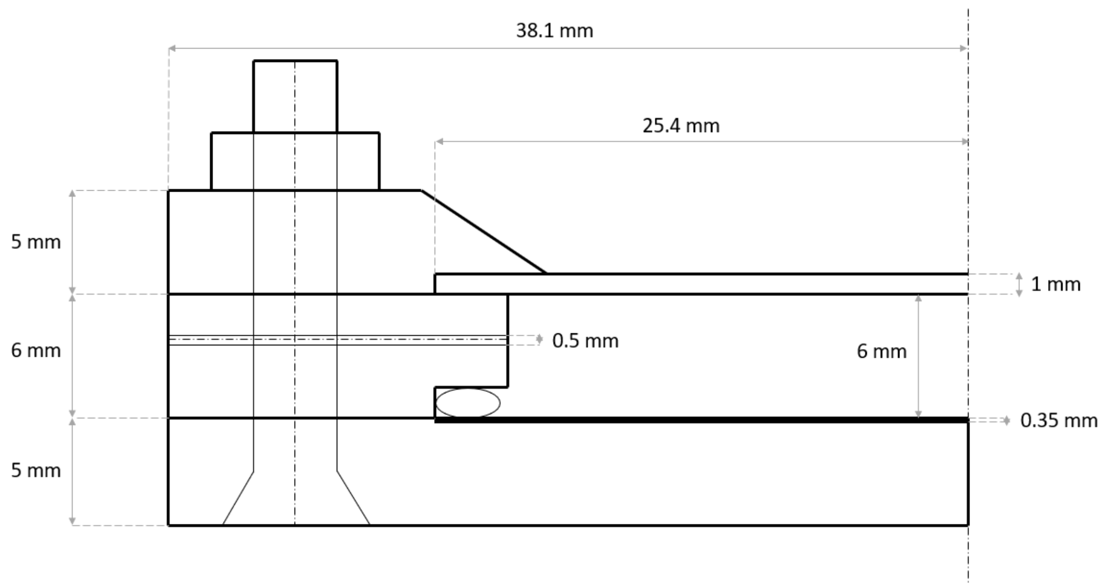

Figure 3.3: Schematic of half cross sectional view of the chamber, with indication of dimensions

The system is sealed with six 18-8 stainless steel screws of 4 mm diameter, with hex drive and flat head, fully threated and passivated to add protection against oxidation and corrosion; six 18-8 stainless steel hex nuts of 8 mm diameter, PTFE-coated and with a slippery surface to resist sticking during installation, chemical resistant as screws, are

tightened following the cross pattern to have a uniform adhesion. The two dowel pins are fixed to the bottom plate.

The distance from the glass to the silicon wafer ensures the focal distance of 6 mm and the small dimensions of the experimental facility make it compatible with microscope observation. Moreover, the chamber allows for changing surface samples since it can be easily assembly and disassembly.

The stainless steel 303 guarantees chemical resistance to organic solvent, as the working fluid and the mixture used for cleaning, and excellent processability of machine tools; the teflon part in the middle allows a good adhesion between parts.

Figure 3.4: Lateral (top) and top (bottom) view of the experimental chamber assembled

3.2.1. O-RING DIMENSIONING

The O-ring used for this static sealing application is a 32 O-ring in Kalrez 4079, which ensures an excellent chemical resistance, comparable to PTFE, but more compressible. The hardness is medium (Durometer 75A) and the internal and external diameter are respectively 1.864 mm and 2.004 mm. A schematic drawing of the O-ring groove and O-ring dimensions are sketched in Figure 3.5, represented in millimeters.

The O-ring cross section area is $\pi * \frac{D^2}{4} = 2.482\ mm^2$, where the diameter D is 1.778 mm.

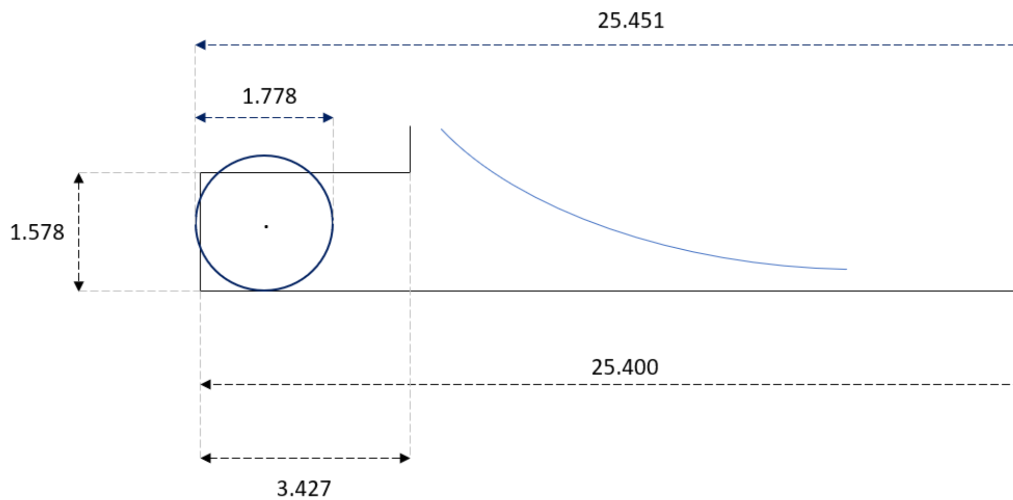

Figure 3.5: Schematic of uncompressed o-ring in half cross sectional view of chamber (millimiters)

The loaded O-ring cross section becomes an elliptical area, which must be equal to the original circular area $A_{circle} = A_{ellipse} = A$; from this consideration, the major axis b of the ellipse is obtained:

$$A_{circle} = A_{ellipse} = \pi * a * b = \pi * \frac{1.578}{2} * b = 2.482\ mm^2$$

$$b = \frac{A}{\pi * a} = 1.0016\ mm$$

With the chosen O-ring and groove dimensioning, the preload thus obtained is about $^4/_{10}$ (0,425 mm), which is adequate for this static application since the experiments are conducted at room pressure and room temperature.

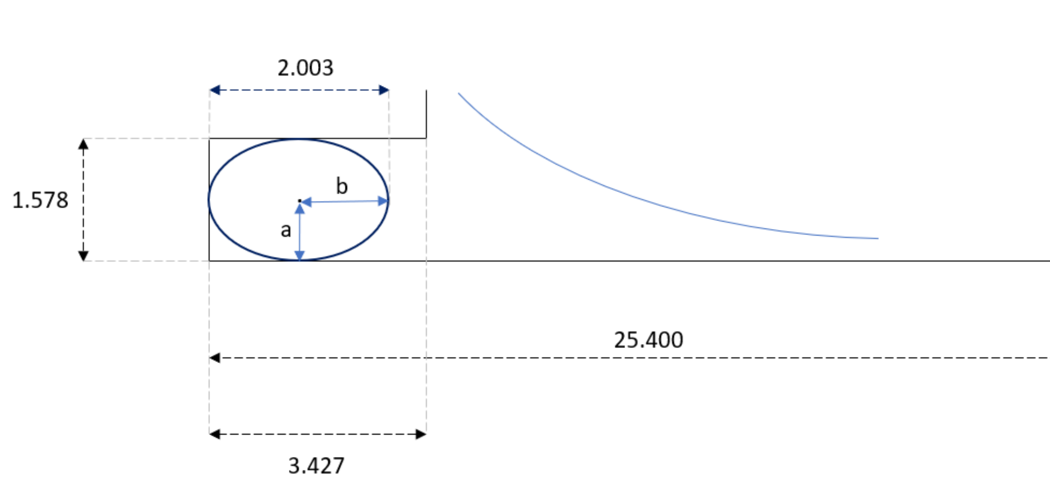

Figure 3.6: Schematic of compressed o-ring in half cross sectional view of chamber

4. CLEANING PROCESS

4.1. SILICON WAFER CLEANING PROCEDURE

The objective of the wafer cleaning process is the removal of particle impurities and organic residues without altering or damaging the wafer surface. Cleaning plays a vital role in all of these experiments in terms of the quality and reproducibility of data, and special care has been taken to standardize the cleaning procedure. Build an experimental procedure to achieve clean surface with repeatable, uniform interference fringes is one of the objective of this work.

Since the working scale is very small and comparable to the scale of dust, the presence of dust particles can significantly alter the contact line dynamics because of contact line pinning and disturb the local film thickness in an arbitrary way. Moreover, due to its significant surface energy, silicon surface is highly susceptible to contamination by adsorption from the ambient and impurities can distort the meniscus profile and affect the measurements. Cleanliness is therefore crucial and extremely important for the accuracy and repeatability of the results.

The silicon wafers are cleaned before and after every processing step and disposed in the plastic closed case. A container for hazardous waste with appropriate label is used to dispose the chemical wastes after every cleaning process.

Two different cleaning procedure has been used: the piranha cleaning and the ultrasonic cleaning; this last one has been performed with three different exposure time of solutions and drying method.

4.1.1. PIRANHA CLEANING PROCEDURE

Piranha cleaning is widely used for removing organic residues off substrates. It is an extremely powerful oxidizer with a high corrosive and aggressive potency. This solution is dangerous when hot and the reaction in the acid piranha is self-starting; rules and safety procedures for this cleaning process must be carefully follow. Piranha can melt and even attack plastic containers, thus only glass beakers and glass graduated cylinders have been used. The handling of Piranha solutions requires special protection equipment including: a protective acid apron, heavy duty rubber gloves and protective glasses.

Many different mixture ratios are commonly used; the used mixture consists in three parts of concentrated sulfuric acid H_2SO_4 and one part of hydrogen peroxide H_2O_2. The solution is mixed in the flow hood; it is prepared by adding hydrogen peroxide to sulfuric acid slowly to prevent thermal shock that may crack the substrate material. If the mixture is made rapidly, it will instantly boil, releasing large amounts of corrosive fumes since it is extremely exothermic.

Silicon wafer is rinsed with distilled water and dried before placing it in a piranha bath. The sample is soaked in the solution for 15 minutes, to allow the mixture to react and remove the organic impurities (cleaning usually requires about 10 to 40 minutes); after that the silicon wafer is removed from the piranha solution and soaked in a distilled water bath. 3-cycle of distilled water rinse are required. Once the sample is adequately rinsed, it is dried with a compressed-air to remove any traces of water and immediately disposed in the plastic case.

Figure 4.1: Glass beakers under the fume hood during piranha cleaning process (left); silicon wafer bathed in piranha mixture (right)

The Piranha cleaning is extremely efficient and produces very good results; however, the sample should be dried with a nitrogen gun to avoid contamination with dust particles and the entire process should be performed in a cleanroom. Since the unavailability of these two elements, and the request for special protection equipment, fume hood, particular attention and caution, the Piranha cleaning is not been considered the adequate procedure for this work.

The interferometry image captured after the Piranha cleaning shows an acceptable cleaning of the substrate, even without the nitrogen gun, since the dust impurities are relatively few (some particles in the adsorbed region) and they does not affect the meniscus profile for our study; however, other cleaning procedure has been tried in order to achieve the same results or close to them, using an easier, faster, safer and more convenient process.

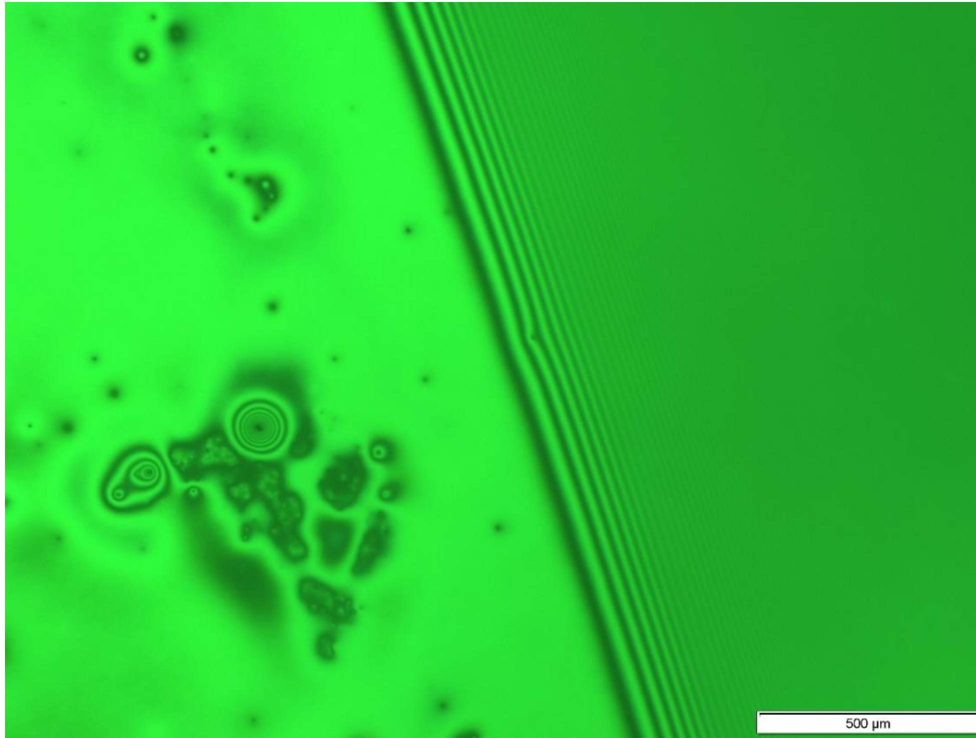

Figure 4.2: Interferometry image of extended meniscus after piranha cleaning process

4.1.2. ULTRASONIC CLEANING PROCEDURE

Ultrasonic cleaning is a process that uses ultrasound, high frequency pressure waves usually from 20-400 kHz, to agitate a liquid; this allows to remove all traces of contaminant adhering to substrates. The result is very fast, easy and effective cleaning.

An ultrasound generating transducer produces ultrasonic waves in the fluid by changing size in concert with an electrical signal oscillating at ultrasonic frequency. This creates compression waves in the liquid of the tank with the consequent formation of million of microscopic bubbles (cavitation); these bubbles collapse with enormous energy and allow the dislodging of dust particles and the removal of impurities on the substrate.

The silicon wafer is placed in a beaker containing the suitable solution; the baker is placed in the ultrasonic bath, previously filled with ordinary tap water. After setting the sonics

time, the power level and the heater (room temperature), the on-button is pressed to run the sonics cycle.

Cleaning normally lasts between three and six minutes, but can also exceed 20 minutes, depending on the object to be cleaned and the type of solution used.

Three different ultrasonic cleaning procedure has been performed and Isopropyl Alcohol, distilled water and two different organic solvents, namely Acetone and Methanol, have been used.

Figure 4.3: Ultrasonic cleaning machine during a cleaning process

4.1.2.1. ULTRASONIC CLEANING PROCEDURE A

The procedure of the ultrasonic cleaning process A consists in the following steps: the wafer is placed in a beaker of the appropriate size, after adding Acetone; the volume of the organic solvent has just to soak the sample. The beaker containing Acetone and the wafer is placed in the ultrasonic cleaner and allowed to sit in the bath for 5 minutes; then the wafer is removed and rinsed with distilled water. The beaker is emptied and cleaned

with distilled water. The second solvent, Methanol, is added in the clean beaker and the cleaning process is repeated as for Acetone; the last one used is Isopropyl Alcohol. Thus, after a total ultrasonic time of 15 minutes, the wafer is removed from the alcoholic solution, allowed to dry for a few seconds and immediately placed in the clean plastic case.

The distilled water has not been used in this process, since the Isopropyl Alcohol dries fast and does not leave residues, it is the last solution which dries on the substrate. Despite this, the wafer substrate had still residues and halos, which disturbed the microscope observation.

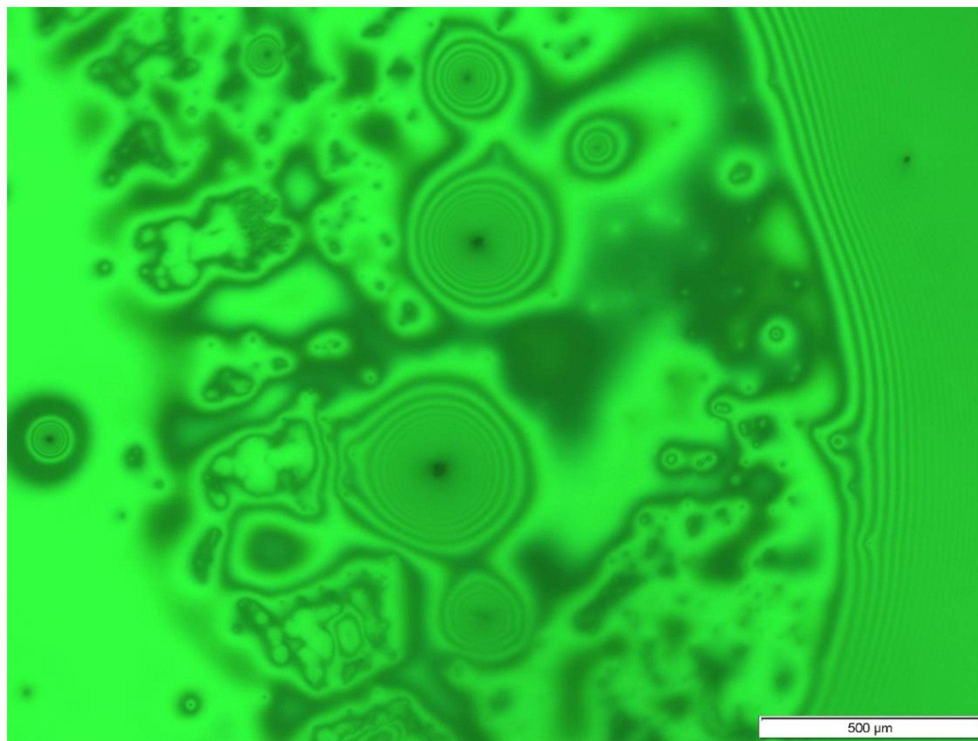

Figure 4.4: Interferometry image of extended meniscus after ultrasonic cleaning A

4.1.2.2. ULTRASONIC CLEANING PROCEDURE B

The procedure of the ultrasonic cleaning process B is similar to the process A, less than the ultrasonic time and the use of distilled water. The three previous solutions are allowed to act for 8 minutes each one, instead of 5 minutes. For the last ultrasonic cycle of 5 minutes distilled water has been used. Finally, the wafer is removed from the beaker and gently dried with compressed-air.

Since the used compressed-air was without filter, during drying dust particles in the air were deposited on the wafer surface; under the microscope, the surface was not satisfactory clean for experiments.

Small dust particles adhering to the surface cause nonparallel fringes in some regions and affect the measurements.

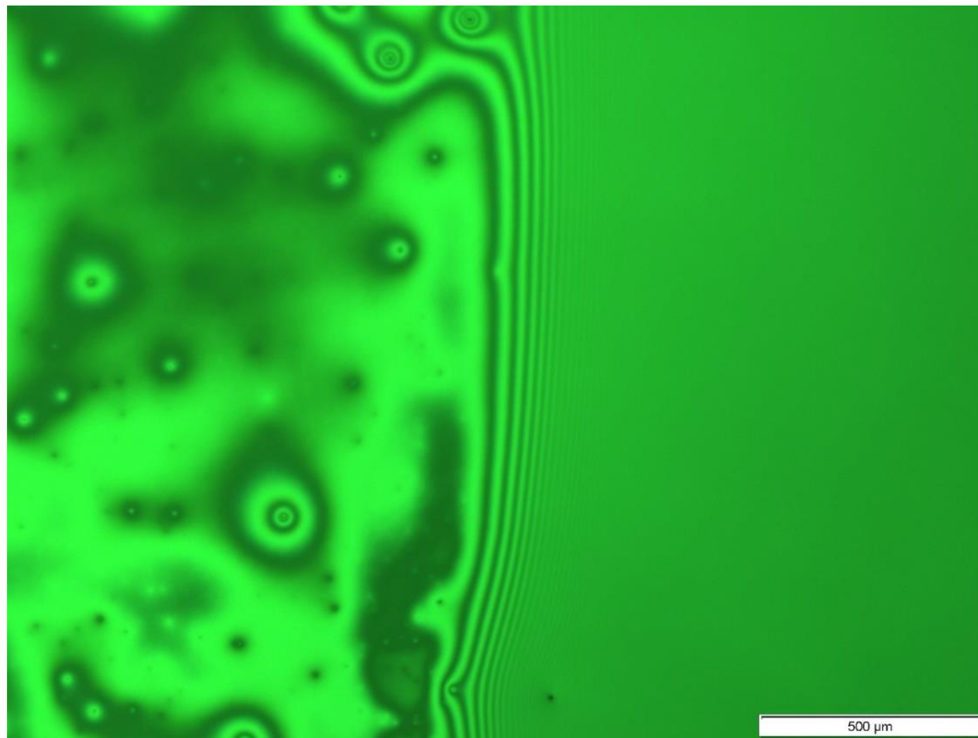

Figure 4.5: Interferometry image of extended meniscus after ultrasonic cleaning B

4.1.2.3. ULTRASONIC CLEANING PROCEDURE C

Acetone, Methanol and Isopropyl Alcohol are used in this process and left in the ultrasonic bath for 10 minutes each one; distilled water is still allowed to act for 5 minutes. At the end of the last cycle the wafer is removed from the beaker and placed vertically, leaning on a container; it is covered with a glass container and let dry for a few hours. Once dried, the sample is quickly placed in the clean plastic case.

The procedure of the ultrasonic cleaning process C was the one who produced the best cleaning result, with a good compromise between cleaning time, cleaning effectiveness and simplicity of the procedure. The drying step is crucial since it should be done ideally in a cleanroom or with a nitrogen gun; let the wafer dry vertically underneath a glass cover container minimizes the contact with the dust particles in the air and achieves acceptable cleaning standard for this work.

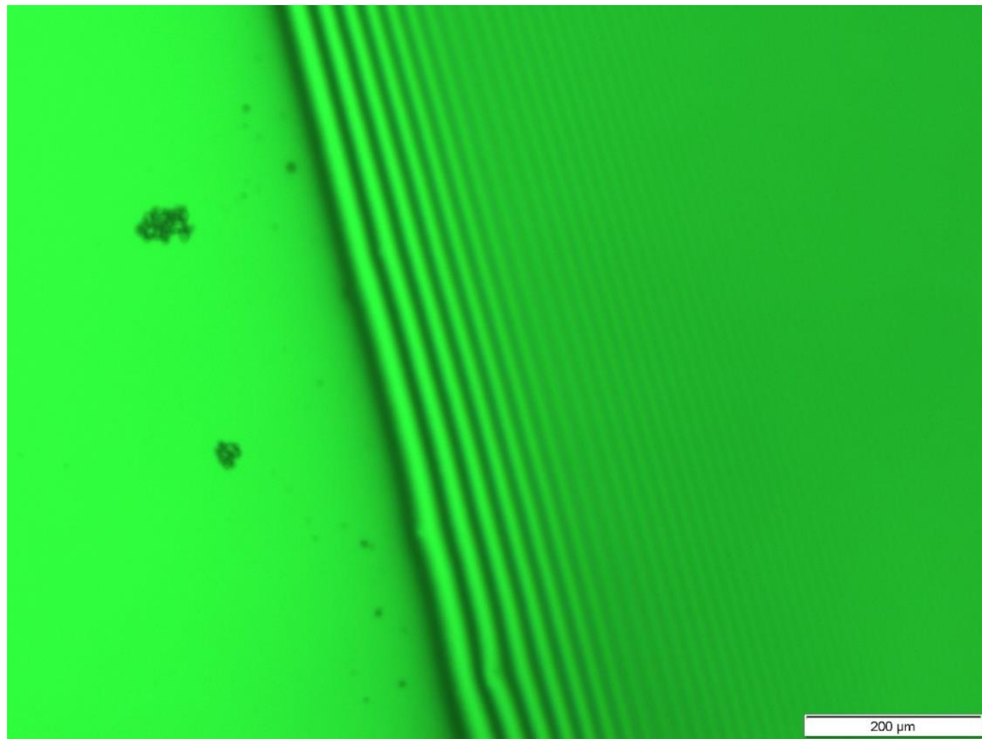

Figure 4.6: Interferometry image of extended meniscus after ultrasonic cleaning C

4.2. CHAMBER CLEANING PROCEDURE

The components of chamber, as well as the samples, are cleaned before and after every meniscus test. The facility is disassembled; each component is rinsed with distilled water and let dry on a clean table.

Particular attention is paid to clean the top steel plate with the glass slide, since it is fundamental to have a perfectly clean visualization window for microscope observations.

The top plate is soaked in Isopropyl Alcohol bath, contained in a beaker of the appropriate sizer; after 15 minutes, the component is removed from the solution and the same step is repeated with Ethanol. After a total of 30 minutes soaked in the cleaning bath, the top plate is dried with compressed-air.

5. DESCRIPTION OF THE EXPERIMENT

5.1. ASSEMBLY PROCEDURE

First, the clean silicon wafer is carefully placed in the appropriate space at the top of bottom stainless steel plate with tweezers; the O-ring is then gently placed above the wafer. After, the Teflon gasket is inserted in the dowel pins, followed by the top plate. Once all the components are in place, the six screws are inserted from the bottom of the chamber in the holes; then, the nuts are added at the top and tightened following the cross pattern. After placing the clean silicon wafer, the chamber is closed as fast as possible and the assembling steps must be quick to keep the sample clean and to minimize the contact with air.

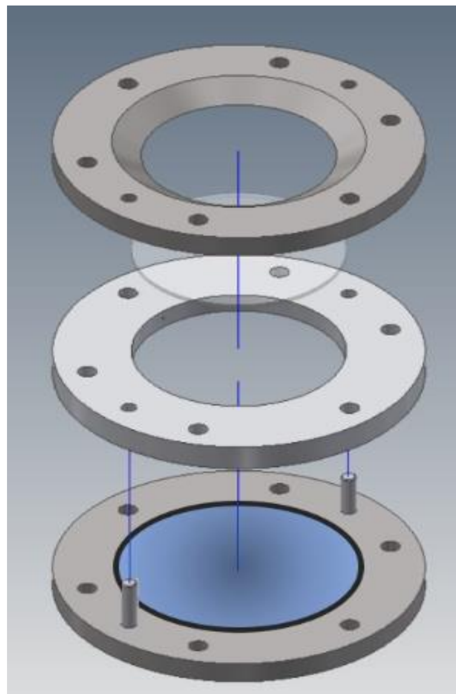

Figure 5.1: Schematic of assembly process of chamber's components

5.2. MENISCUS TEST PROCEDURE

Meniscus test are performed to analyze the effect of closeness to chamber wall and of volume of octane into the facility on meniscus shape and film thickness. This is to check a repeatability of experimental measurements and to determine the adequate position range where to take the interferometry images and the adequate amount of liquid which is to inject in the facility in order to reach consistent results.

In order to visualize properly the meniscus profile and to form a liquid pool with an extended curved meniscus, the whole assembly was slightly tilted with respect to the horizontal at 3.45 degrees with a plastic rectangular bulk 13.12mm thick, so that an octane reservoir is present at the lower end of the cell.

For each experiment, the chamber was filled through a syringe with 3 different amounts of octane to compare meniscus profiles at 3 different pool positions.

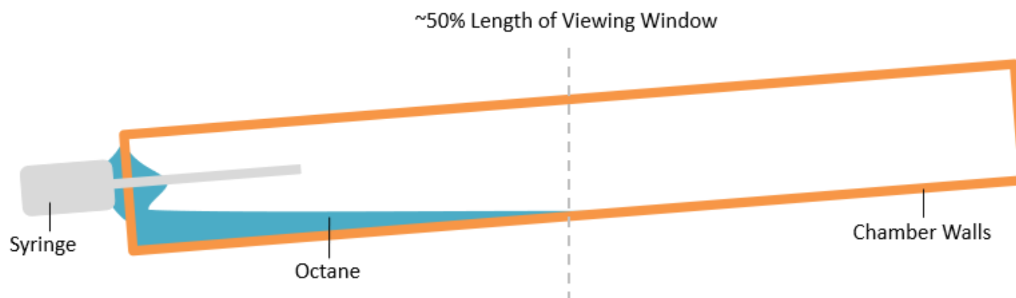

Figure 5.2: Schematic of tilted chamber during the filling

After each filling, the system was left to equilibrate with the surroundings before taking any data; it is necessary for reaching a steady-state and a uniform and stable pool of liquid, giving initials evaporation phenomena time to stop, in order to visualize properly the fringes. Furthermore, the manual pressure used with the syringe during the filling was sometimes excessive and caused the spreading out of octane which wetted most of the surface of the silicon wafer, therefore, the waiting time allowed the meniscus to recede and stabilize.

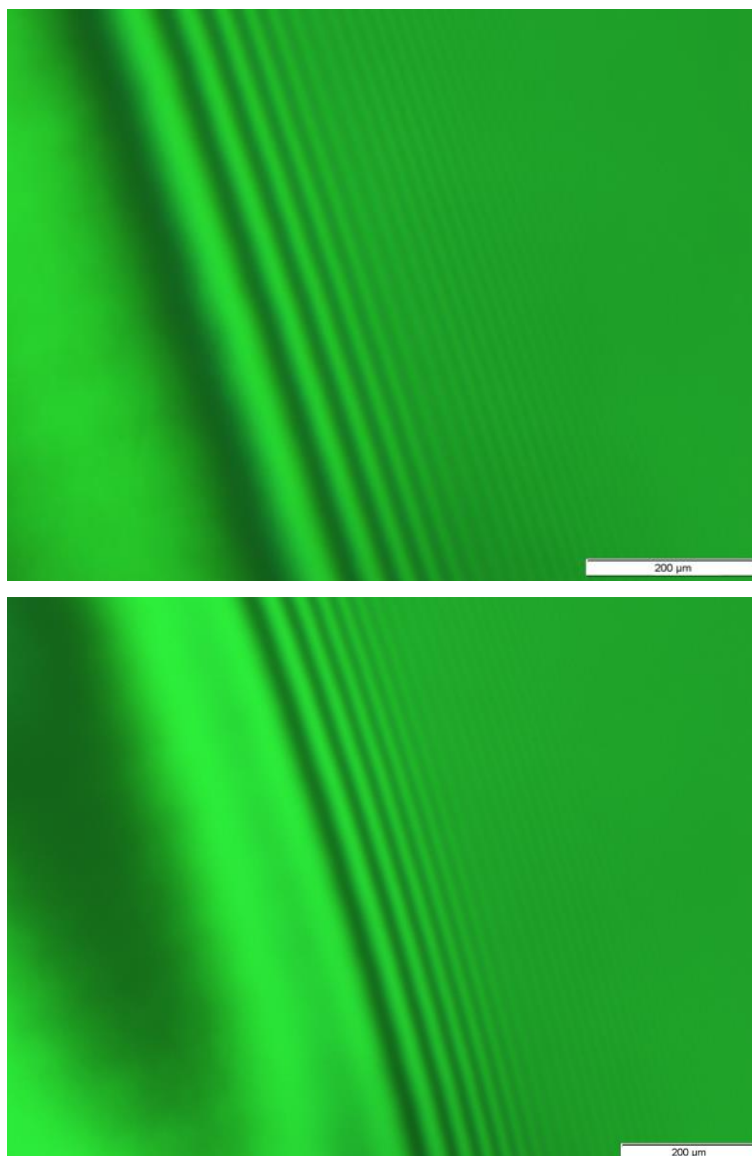

Figure 5.3: Two interferometry images at the same horizontal position of receding meniscus during a test; taken after about an hour from the filling (top); taken after about 3 hours from the filling (bottom)

The experimental procedure to perform a Meniscus test is reported below. A total of 14 meniscus test have been conducted, and each of them has been performed at room pressure and room temperature.

The assembled chamber is placed on the microscope stage, previously tilted. An appropriate amount of octane is injected into the micro hole with the syringe such that a pool of liquid is formed and submerges a part of the silicon surface.

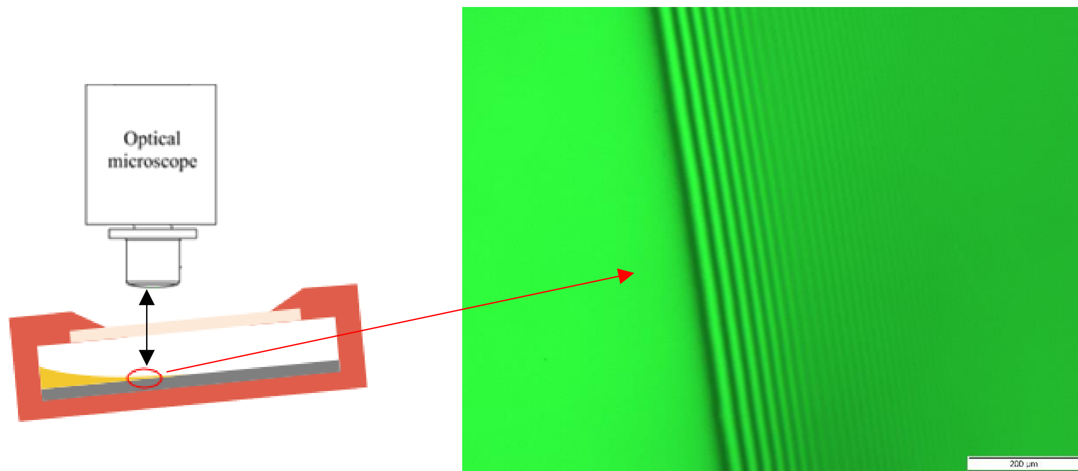

Figure 5.4: Schematic of experimental setup during a test (left); interferometry image of octane pool edge on smooth silicon wafer (right)

The microscope's illumination is turned on and the light is set to a comfortable level; the fine focus knob is adjusted on smallest detail visible in the field, by using a 10x objective or a 5x objective. The difficulty of the focus step is due to the fact that it is difficult to distinguish the wafer surface from the glass surface, if the sample is perfectly clean. After that, it is necessary to wait the chamber for reaching the steady state; during the entire time it is ensured that the facility is poised motionless.

Once the waiting time is passed, the interferometry images of the pool edge, that show the optical interference pattern representing the thickness profile, are taken with the camera, from side to side covering the entire pool edge. Subsequently, the second filling is made by injecting a further volume of octane inside the cell, until it covers the second desire amount; after reaching the equilibrium state, the second set of interferometry images are taken. Finally, after waiting the requisite hours, the third filling is performed and the last set of images of the pool edge are captured.

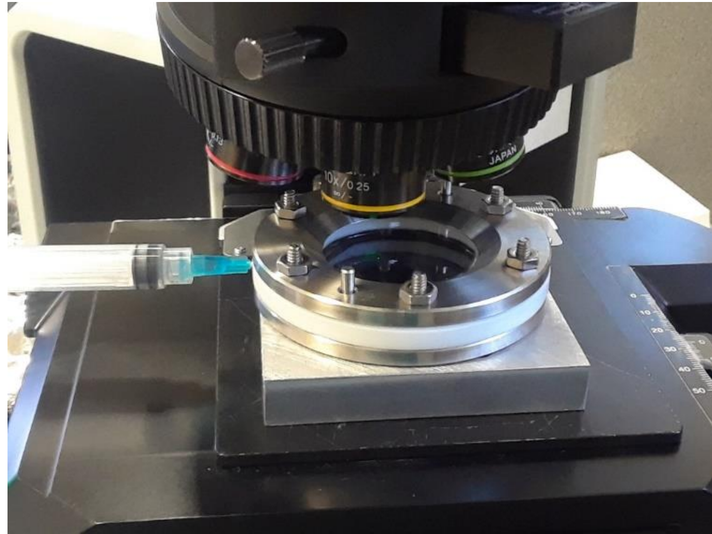

Figure 5.5: Experimental setup during a test

To avoid the leaking of octane through the micro-hole of the chamber, different sealing solutions have been considered during the test and presented in the Chapter (7).

6. POST DATA PROCESSING

6.1. MATLAB CODE STEPS

The acquired interferometry image is processed by the code and first converted in a greyscale image.

The first user defined step is to manually draw a line perpendicular to fringes, from the light region (adsorbed film) to the greyer region (bulk meniscus) where fringes start to be indistinguishable; that will be the direction on which the thickness profile is extracted. The length of the drawn line does not affect the calculation since it is defined in the next step.

Two more boundary lines are drawn by the code, parallel to the user central line. The three lines are plotted, representing the pixel gray values versus the distance along the profile. The dark fringes are represented by valleys as the bright fringes by peaks. The three plotted lines are coincident when the user defined line is exactly perpendicular to fringes. An average intensity profile in the across perpendicular direction is obtained, as shown in Figure 6.2.

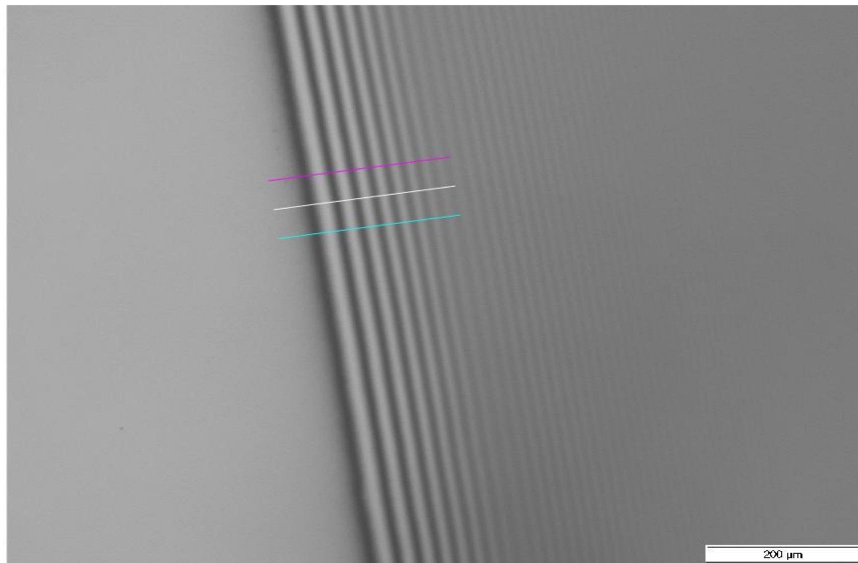

Figure 6.1: Image processing lines: user-drawn line (white), left/right boundaries for averaging (magenta, blue)

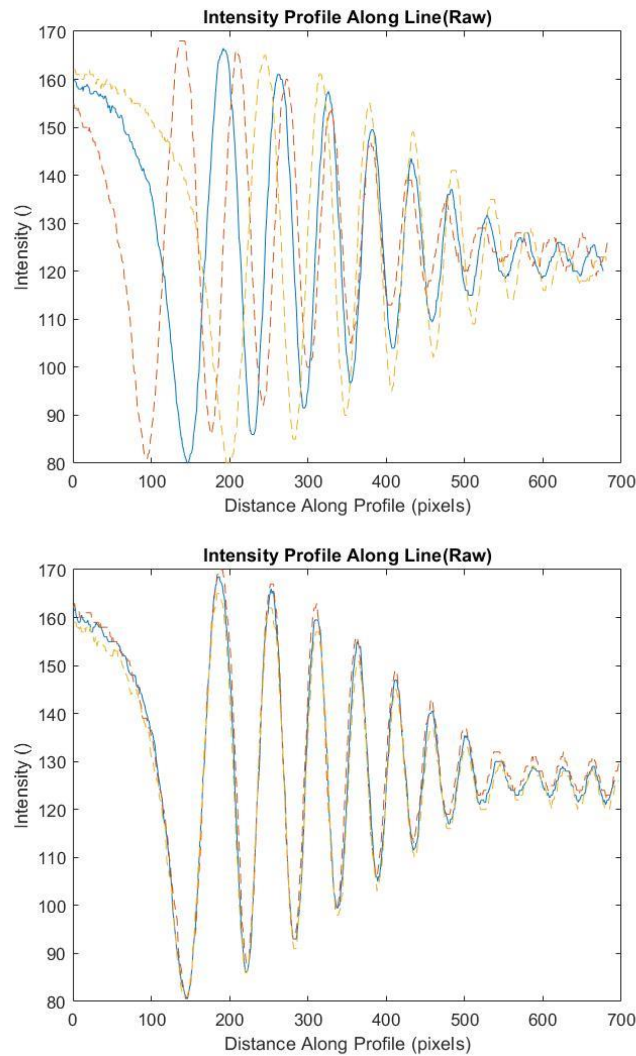

Figure 6.2: Plot of intensity between user-drawn line (blue), left/right boundaries (dashed orange, dashed red) vs. distance along profile; not parallel to fringes (top); roughly parallel to fringes (bottom)

In order to reduce the effect of the user drawn line, a step has been added: the code searches +/- 2.5 degrees for angle with lowest standard deviation between parallel line profiles.

The code draws a set of parallel lines inclined to the user-line; the intensity profiles of each line and its parallels are plotted. The more divergence the profiles have (the centerline line and the boundary parallel lines), the more inclination to the exact perpendicular to fringes they have. Thus, for each inclination to the user-line in the range

of +/- 2.5 degrees with increments of 0.1 degrees, the code calculates the standard deviation between the intensity profiles; finally the standard deviation versus the angle of inclination is plotted, and the angle corresponding to the minimum of that curve represents the lowest divergence between the profile, namely the right one perpendicular to fringes.

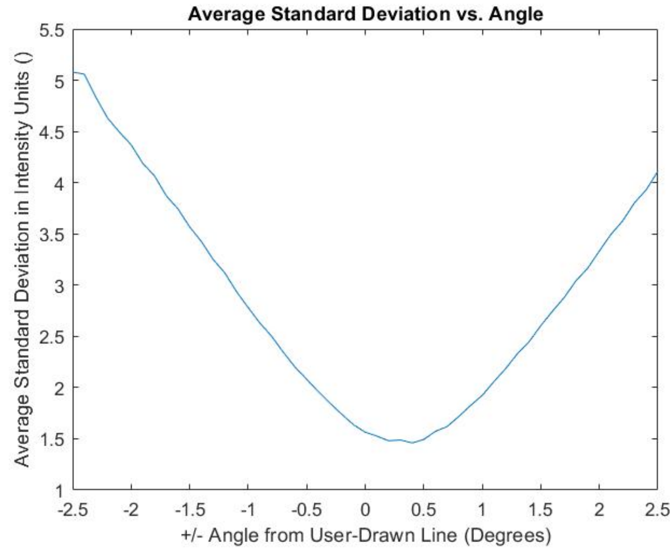

Figure 6.3: Plot of standard deviation between rake of line profiles vs. angle adjustment of user-drawn line

For example, in Figure 6.3 the user-line has been drawn inclined at -0.75 degrees to the perpendicular to fringes. If the user-line is drawn with a slope error greater than 2.5 degrees, it is out of the range and the code is not able to correct it.

The code applies the angle adjustment to the slope, correcting the inclination of the user-line, on which the thickness profile is derived.

An average intensity profile of the fringes area delimited by the two boundary lines across the selected perpendicular direction is obtained. The length in perpendicular direction to average across L and the number of parallel lines for standard deviation calculation N (namely the unit length of spacing between them) is set respectively 150 μm and 25 μm, an adequate compromise between effectiveness of results and computation time.

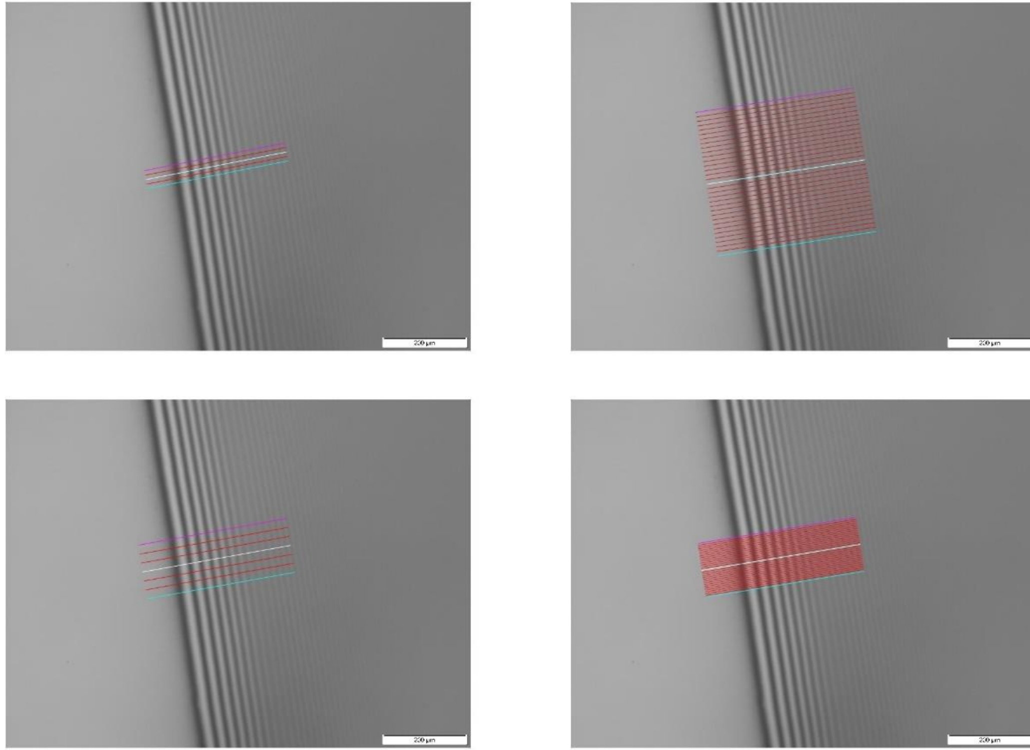

Figure 6.4: Image processing line: user-drawn line (white), left/right boundaries for averaging (magenta, blue), rake of line profiles to calculate standard deviation (red); L=50, N=25 (top left); L=400, N=25 (top right); L=150, N=50 (bottom left); L=150, N=10 (bottom right)

The second user defined step is to cut the desire portion along the x-axis direction in the intensity plot.

The start point has to fall between the adsorbed film region (constant pixel value region) and the first fringe; then, the beginning x point is set by the code 25 points (pixels) prior to the first dark fringe. The ending point is the real user-defined determination of the length of the cut portion, which has been chosen to be from 500 to 600 pixels, to compare results in the same portion of the fringes area for each processed image.

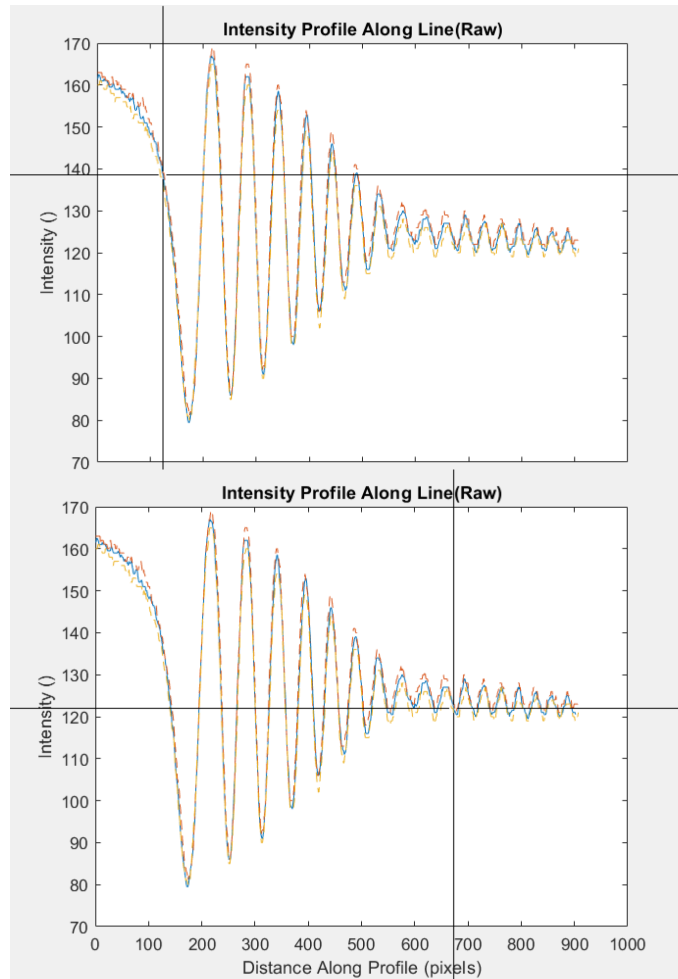

Figure 6.5: Plot of intensity vs. distance along profile: first cut before the first dark fringe (top); second cut in the bulk meniscus region with a total length between 500 and 600 pixels (bottom)

The code scan peaks and valleys and filters noises with a smoothing algorithm, until maximum and minimum points are located and separated from each other. The curve is smoothed until the user decided that peaks and valleys are correctly identified.

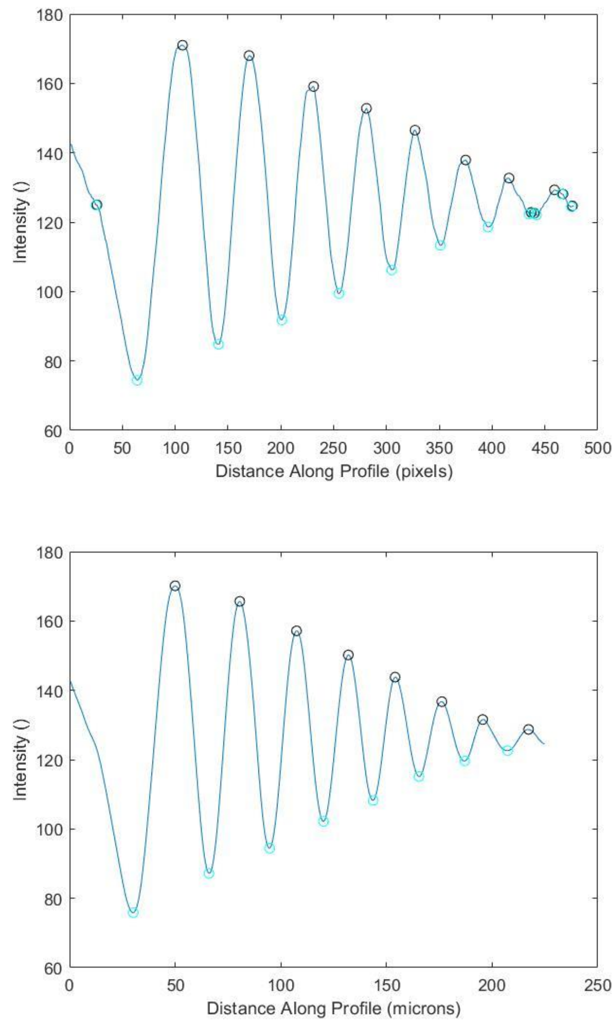

Figure 6.6: Plot of intensity vs. distance along profile with peaks/valleys marked: profile line in pixels before smoothing (top); profile line in microns after smoothing (bottom)

The x axis, the distance along the profile, is turned from pixel to micron by knowing the proportion between them for the setting objective of the microscope. The used working zoom are 10x objective, for which 200 microns correspond to 454 pixels, and 5x objective, for which 500 microns correspond to 572 pixels.

Then the code determines the reflectivity of any given pixel and calculated the film thickness for each of them. A plot of film thickness versus distance along the profile is obtained.

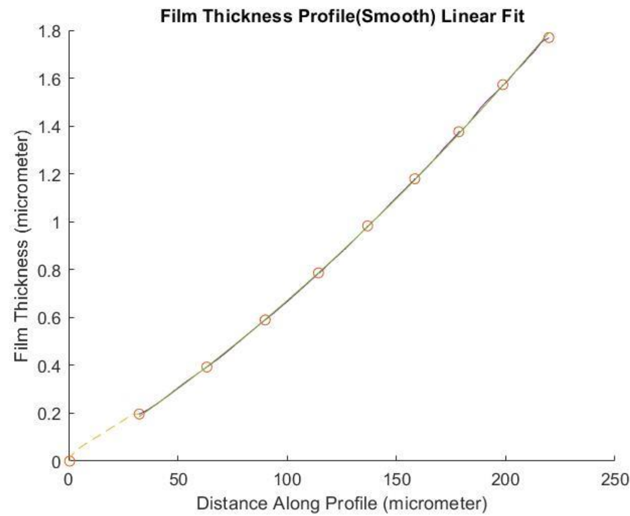

Figure 6.7: Plot of film thickness smoothed profile: extrapolated portion (dashed orange), fitted curve (green), smoothed curve (purple), peaks/valleys (dots)

The orange dash line is the extrapolated portion of the adsorbed region; the film thickness profile in the adsorbed layer region is set to zero. The positions of peaks and valley are highlighted by the red circles.

The purple solid line is the smooth curve representing the film thickness profile obtained by the interferometry relationship between reflectivity and pixel gray values, described at Chapter 2.1. Despite the smooth algorithm applied by the code, the film thickness profile curve is not clean and still presents noises, which can be reduced using a filter, described in the next paragraph, but not completely removed.

The green solid line is the fitted curve, approximated by using a least squares method to fit a circle to the non-extrapolated data, representing the envelope of minimum/maximum point (valleys/peaks).

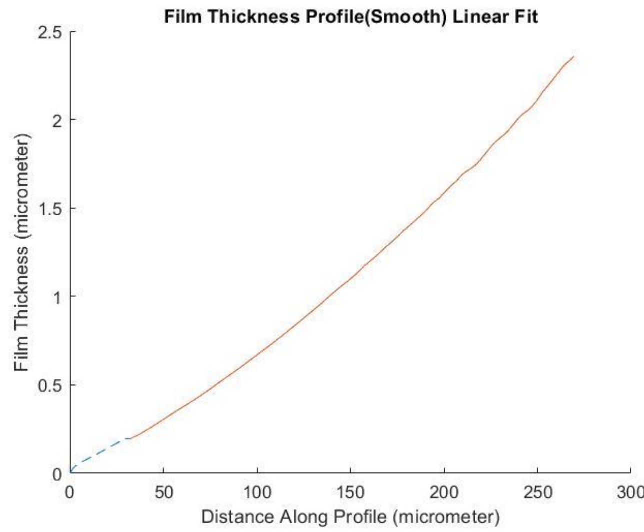

Figure 6.8: Plot of film thickness smoothed profile: extrapolated portion (dashed blue), smoothed curve (red)

6.2. NOISE FILTERING

Since an optical technique for the measurement of the film thickness profiles has been used, the relative contrast of dark and bright fringes has a profound effect on the measurement capability and its accuracy.

If the two refractive indices, both for the solid surface and the liquid one, are close to each other, a drastic reduction in contrast takes place and it will be difficult to see the fringes and perform any image analysis due to the high noise in the captured picture, in particular in the bulk meniscus region.

The problem of noises is crucial especially for nano-structured surfaces, since the roughness of the solid substrate causes a not clear contrast between fringes.

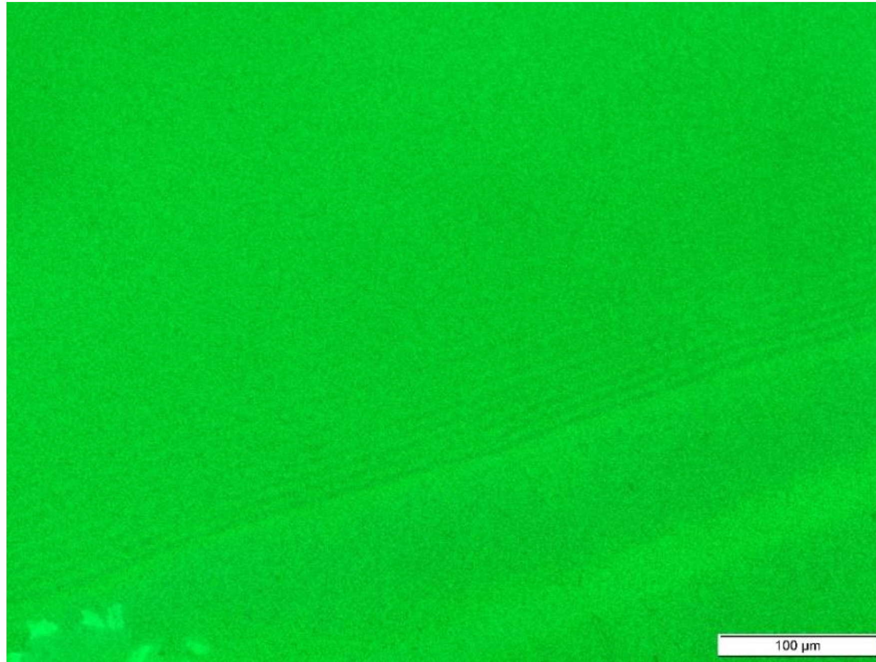

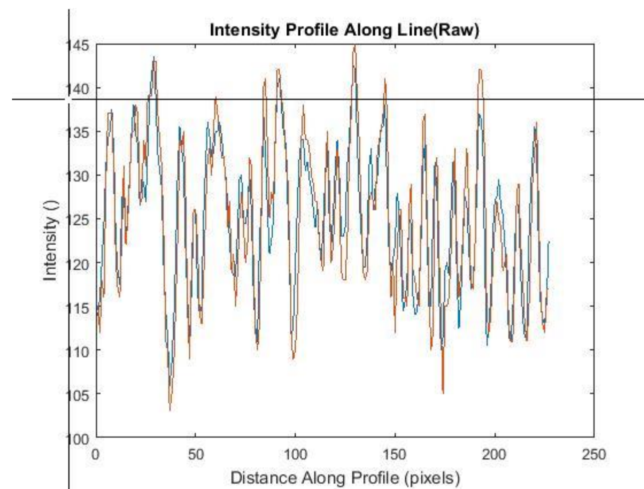

Figure 6.9: Noisy interferometry image of octane pool edge on a nanowire surface (top); Intensity plot of the noisy interferometry image (bottom)

For this reason, a filter has been added to Matlab code. The noise filtering must retain the original image intensity to not loss information from the acquired data.

A median filter was found to be the best solution and it was applied to the gray scale image, without altering the intensity of gray scale image; a 5×5 kernel matrix was used, where each output pixel contains the median value in the 5-by-5 neighborhood around the corresponding central pixel in the input image.

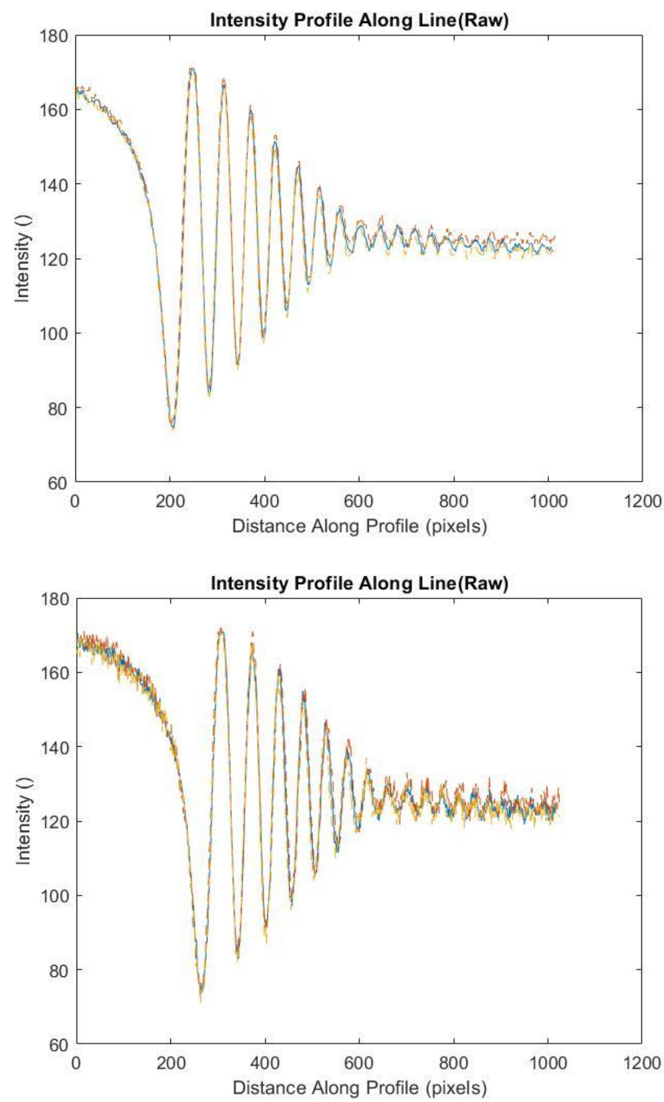

Figure 6.10: Intensity plot with median filter addition (top); intensity plot without filter addition (bottom)

This filter is effective in removing random, high impulse noise and softens the interferometry image, especially in the bulk meniscus region.

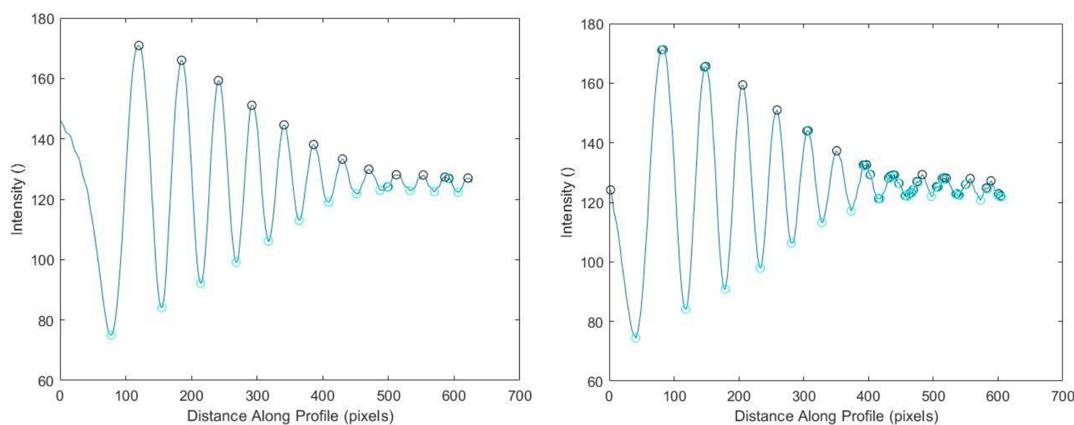

Figure 6.11: Intensity plot before smoothing with peaks/valleys marked; median filter addition (left); without filter addition (right)

6.3. AVERAGE CURVATURE

To compare the meniscus profiles from multiple images, a parameter is introduced, representing an average curvature of the film region (length from 500 to 600 pixels), which includes both the transition region and the bulk meniscus region, while the adsorbed film thickness is extrapolated (not included in the fitting circle) and set to a value of zero. The curvature is approximated by using the least squares method (green solid line).

It should be remembered that the ultimate goal is to experimental measure the constant curvature in the bulk meniscus region, but in order to check the consistency of the meniscus profile and standardize the measurement procedure, an average curvature is calculated, to make comparison between test results.

In order to cover the entire region, four values of curvature are calculated for each image by drawing the line in four different locations. Thus, the final curvature representing the thickness film profile of an image is the average value of the four different values.

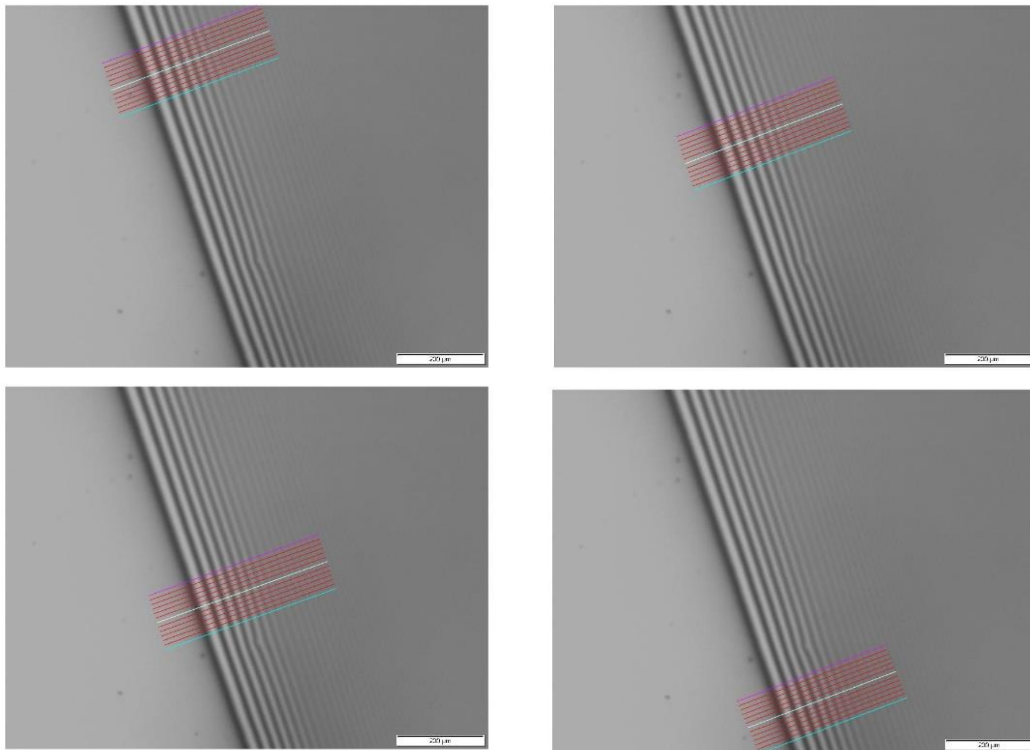

Figure 6.12: Four processing lines covering four pool positions of the same interferometry image (L=150, N=25)

6.4. BULK MENISCUS CURVATURE ESTIMATION

Different method to calculate the constant value of bulk meniscus curvature K_∞ has been tried. The ideal trend of curvature in the 3-phase-contact-line is reported below.

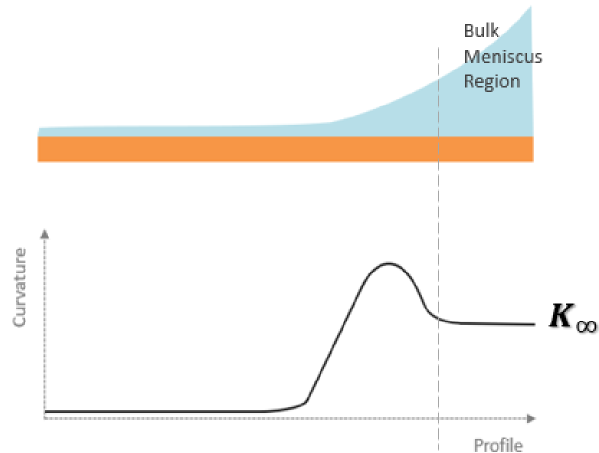

Figure 6.13: Schematic of extended meniscus (top); ideal trend of curvature vs. thickness profile (bottom)

First, with MATLAB code, the second derivative of film thickness profile is been calculated. Despite the smooth algorithm, the obtained meniscus curve has still a lot of noises, in particular in the bulk region, which significantly spread with the second derivative.

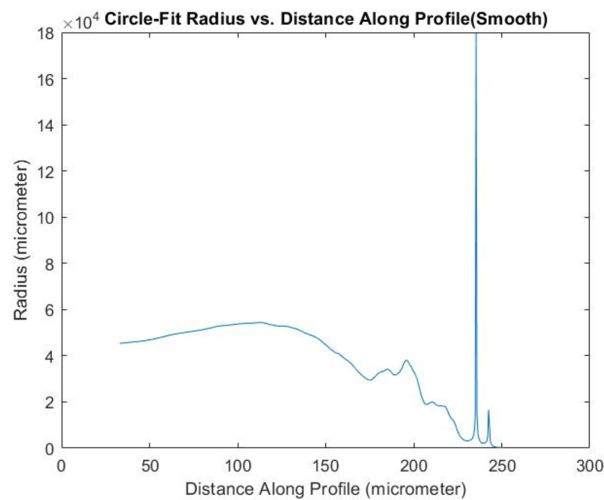

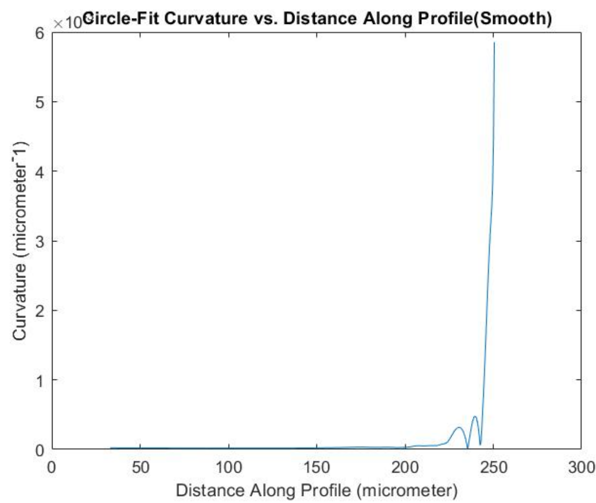

Figure 6.14: Plot of curvature (second derivative) of smoothed profile (top); plot of radius of smoothed profile (bottom)

The reported plots of the radius and the curvature of the meniscus thickness profile do not show anything meaningful; the very different trend from the ideal curvature plot is evident. This, it is difficult not only measure the expected constant curvature but also to recognize when the bulk meniscus region starts.

In order to mitigate and try to reduce the spreading errors, the first derivative has been calculated, namely the plot of the slope. The ideal trend of it is reported in Figure 6.15.

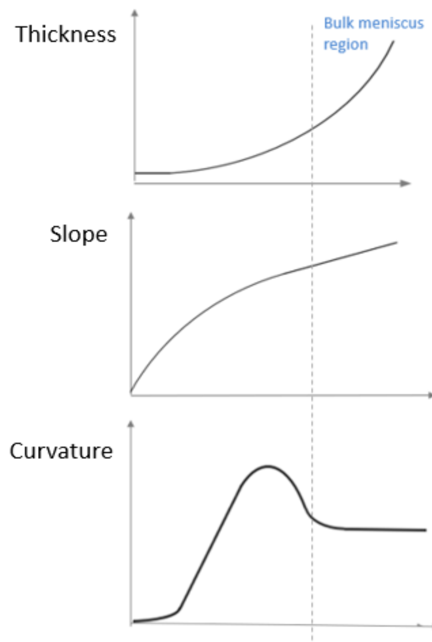

Figure 6.15: Ideal trend of thickness, slope and curvature of extended meniscus

Since the thickness constantly increases, from the adsorbed to the bulk meniscus region, the relative slope is an increasing curve, which starts from zero, changes inclination and reaches a linear trend, corresponding to the constant curvature in the bulk meniscus region. Even so, the noises still propagate with the first derivative calculation, though less strongly than with the second one.

The second attempt was to obtain the slope plot by calculating the slope at point i as the slope of the linear curve between point $i+1$ and point $i-1$, linearizing with a least square method that portion of curve. This was also unsuccessful, and the graph reported in Figure 6.16 does not show a recognized trend and the linear portion is not distinguishable.

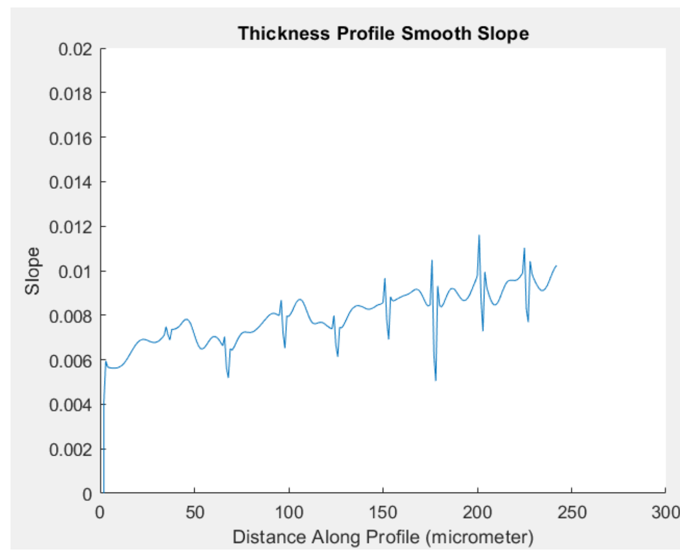

Figure 6.16: Plot of slope (linearization) of smoothed profile

By increasing the range of the linearization until $i \pm 8$, significant differences did not be noticed and the results did not yet relevant.

Another calculation attempt has been performed: the code addition calculated the curvature for smaller portions of meniscus profile and get a plot of more localized curvature as a function of distance along the line profile.

This piecewise method consisted of dividing the meniscus into evenly sized pieces and fitting a circle to each piece. Peaks and valley were used as key separation points.

Even though errors should be reduced since they affect circle fit less when using less data and cutting meniscus into more pieces, the results were not significant and the bulk meniscus portion has still noises.

7. MENISCUS TEST

A parameter introduced, representing the average curvature of the extended meniscus, is used to compare results, in order to analyze the effect of closeness to solid wall and of volume of fluid into the facility on meniscus shape and film thickness.
A large number of the images of the interference fringes of the liquid film are captured, and the film thickness and curvature profiles are evaluated.

The measurements were performed at different pool position, namely different amount of octane, and different location along the pool edge, to calculate the dispersion of measurements in order to achieve a repeatable procedure and consistent results. The dispersion of values has been calculated using the mean error:

$$Mean\ error = \frac{\sum_{i=1}^{N} |x_i - \bar{x}|}{N}$$

(7.1)

7.1. MENISCUS TEST 1

The first Meniscus test has been performed for pool at 20%, 50%, and 75% the length of the wafer in the viewing window.

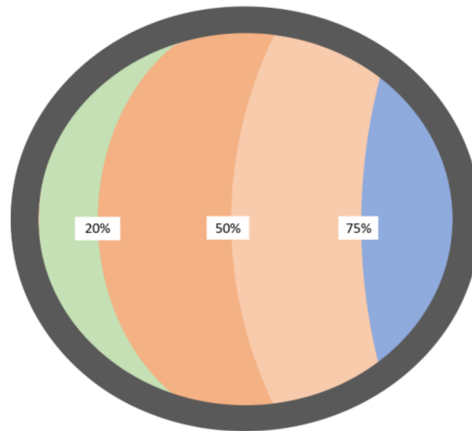

Figure 7.1: Schematic of meniscus position in viewing window of closed chamber

A new fresh silicon wafer has been used for this test. Despite this, the interferometry images captured are not properly clean and some dust particles are still present, because the assembly procedure has been probably made not fast enough to avoid deposition of impurities.

A plastic syringe of capacity 3 milliliters, with a 25 Gauge blunt tip bulk disposable needle of 5/8 inch length has been used for this first test; probably due to the needle length lower than the hole length, a heavy manual pressure was required for filling the chamber and for this reason the normal time of the test was prolonged.

Once the syringe deposited all fluid in the cell, the pool of octane on the lower tilted side reaches the needle hole and the chamber consistently leaked through it. For this reason, the meniscus constantly receded and all the acquired images for this test are quasi-steady.

The waiting time to allow equilibrium was less than 1 hour, for all the three filling. The entire movement of the film is recorded to analyze the advancing film at different instants of time as well as at its final equilibrium state (quasi-steady). The meniscus recedes from about 300 micrometers in less than 1 hour. Naturally occurring interference fringes are readily observed because of the constructive and destructive interference of the reflected light from the curved liquid meniscus and the solid silicon surface.

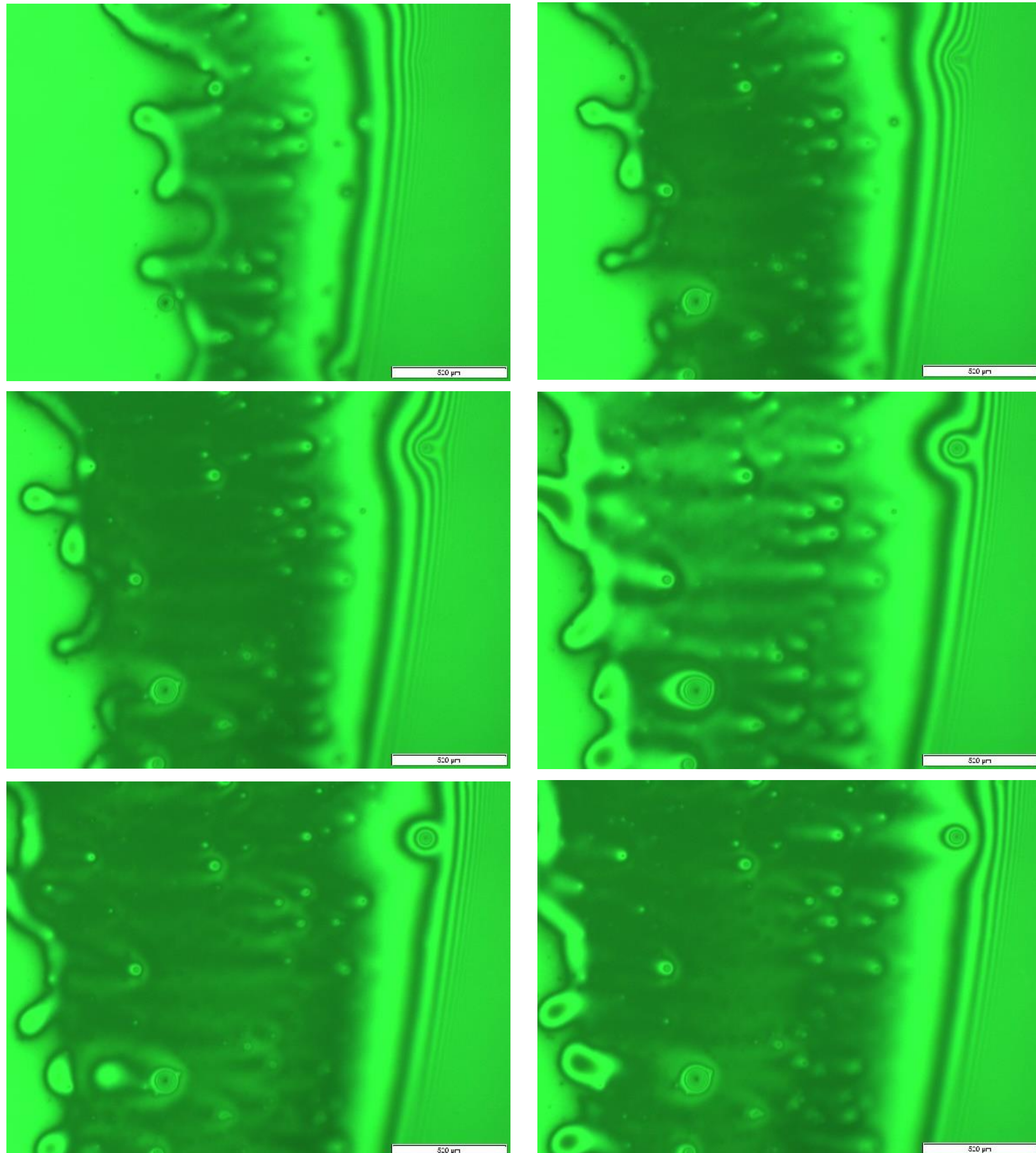

Figure 7.2: Interferometry images of receding meniscus at 6 different moments, from the moment immediately after the filling (first top left) to an hour later (last bottom left)

The values of curvature are reported below. The curvature of each image is the average of 4 values of curvature. The average curvature of the images at each pool position represents a value of curvature obtained for the specific amount of volume. The final average curvature representing the performed test is the average between the curvature of each pool position.

The mean error is calculated, to measure the relative variability of results and the dispersion of data.

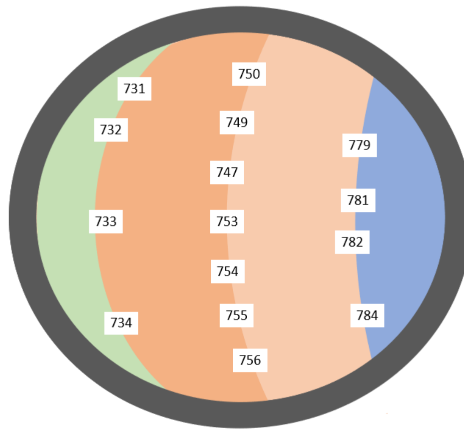

Figure 7.3: Schematic of locations of interferometry images in viewing window of closed chamber for Meniscus test 1

Volume %	Image	Curvature 1	Curvature 2	Curvature 3	Curvature 4	Average	Mean Error
unit of measure		1/µm	1/µm	1/µm	1/µm	1/µm	1/µm
20	731	2.17E-05	2.16E-05	2.06E-05	2.07E-05	2.11E-05	5.11E-07
	732	5.17E-05	5.76E-05	7.92E-05	8.00E-05	6.72E-05	1.25E-05
	733	5.77E-05	5.64E-05	4.17E-05	5.87E-05	5.36E-05	5.98E-06
	734	5.47E-05	4.37E-05	5.31E-05	5.39E-05	5.13E-05	3.83E-06
	Average					4.83E-05	1.36E-05
50	747	2.53E-05	2.62E-05	2.70E-05	2.58E-05	2.61E-05	5.32E-07
	749	3.81E-05	2.59E-05	2.48E-05	2.64E-05	2.88E-05	4.66E-06
	750	2.70E-05	3.06E-05	3.05E-05	3.05E-05	2.96E-05	1.31E-06
	753	3.08E-05	2.92E-05	2.96E-05	2.85E-05	2.95E-05	6.96E-07
	754	3.73E-05	3.39E-05	3.38E-05	3.41E-05	3.48E-05	1.27E-06
	755	2.99E-05	3.06E-05	3.05E-05	3.31E-05	3.10E-05	1.05E-06
	756	3.61E-05	3.83E-05	3.39E-05	3.60E-05	3.61E-05	1.14E-06

	Average					3.08E-05	2.67E-06
75	779	2.11E-05	2.35E-05	2.01E-05	2.15E-05	2.15E-05	9.72E-07
	781	2.51E-05	2.55E-05	2.19E-05	2.23E-05	2.37E-05	1.61E-06
	782	2.05E-05	2.03E-05	1.97E-05	2.18E-05	2.06E-05	6.25E-07
	784	2.12E-05	1.98E-05	2.11E-05	1.85E-05	2.02E-05	1.04E-06
	Average					2.15E-05	1.12E-06
Average						3.35E-05	1.34E-05

Table 7.1: Curvature measured for Meniscus test 1

7.2. MENISCUS TEST 2

The Meniscus test number 2 has not been completed because a piece of Teflon probably detached from the hole in the gasket part of the chamber affected the measurements.

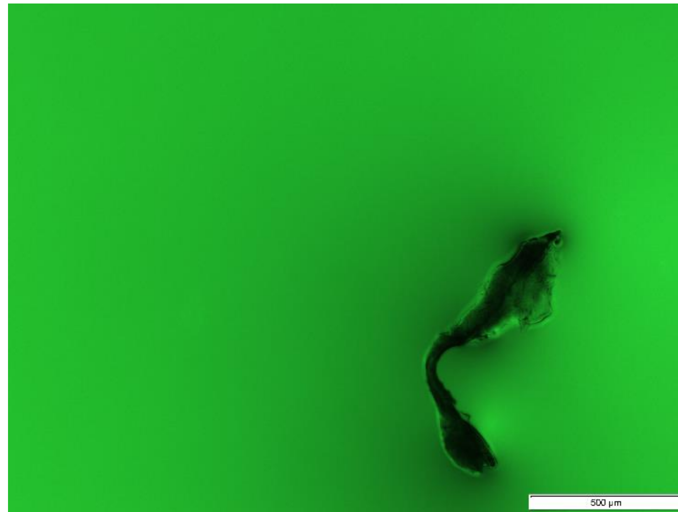

Figure 7.4: Piece of teflon affecting measurements during Meniscus test 2

The silicon wafer used for this test was new and completely clean as for the first test, but probably due to the not yet familiarity and ability of the assembly process, it still presented dust particles on the surface.

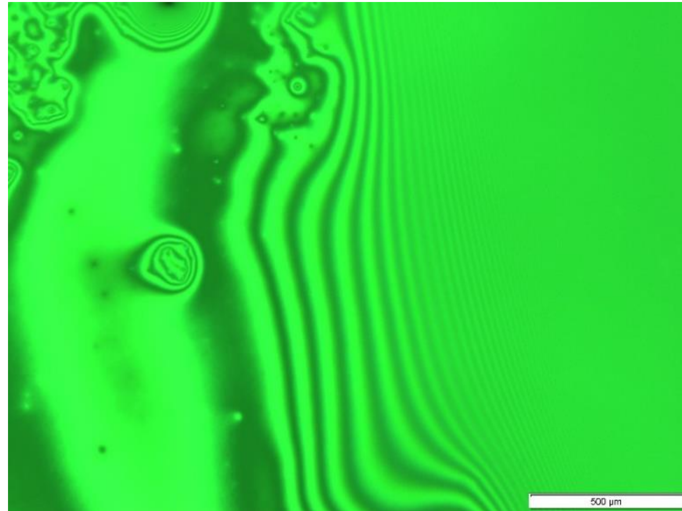

Figure 7.5: Interferometry image of octane pool edge on fresh silicon wafer captured during Meniscus test 2

Despite this, before stopping the test, two set of interferometry images of pool at 35% and 50% has been taken and the results are reported below. The silicon wafer was cleaned with the ultrasonic cleaning procedure (A).

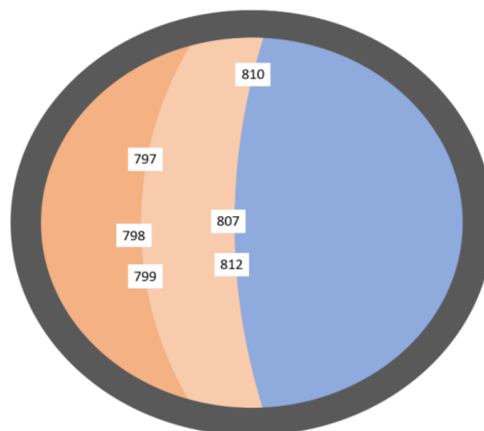

Figure 7.6: Schematic of locations of interferometry images in viewing window of closed chamber for Meniscus test 2

Volume %	Image	Curvature 1	Curvature 2	Curvature 3	Curvature 4	Average	Mean Error
unit of measure		1/μm	1/μm	1/μm	1/μm	1/μm	1/μm
35	797	2.32E-05	1.39E-05	1.54E-05	1.63E-05	1.72E-05	2.97E-06
	798	3.43E-05	3.53E-05	9.35E-06	2.35E-05	2.56E-05	9.20E-06
	799	2.33E-05	2.45E-05	1.81E-05	2.17E-05	2.19E-05	1.99E-06
	Average					2.16E-05	2.90E-06
50	807	2.76E-05	3.31E-05	3.11E-05	3.75E-05	3.23E-05	3.00E-06
	810	5.56E-05	5.31E-05	5.10E-05	5.27E-05	5.31E-05	1.24E-06
	812	2.10E-05	2.02E-05	2.45E-05	2.30E-05	2.22E-05	1.56E-06
	Average					3.59E-05	1.15E-05
Average						2.87E-05	7.15E-06

Table 7.2: Curvature measured for Meniscus test 2

7.3. MENISCUS TEST 3

For the Meniscus test number 3, the silicon wafer used in the test number 2 has been used after the ultrasonic cleaning process (A). The acquired images are overly dirty and, according with results, the curvature has a high variability both for different pool position and different location along the same pool profile.

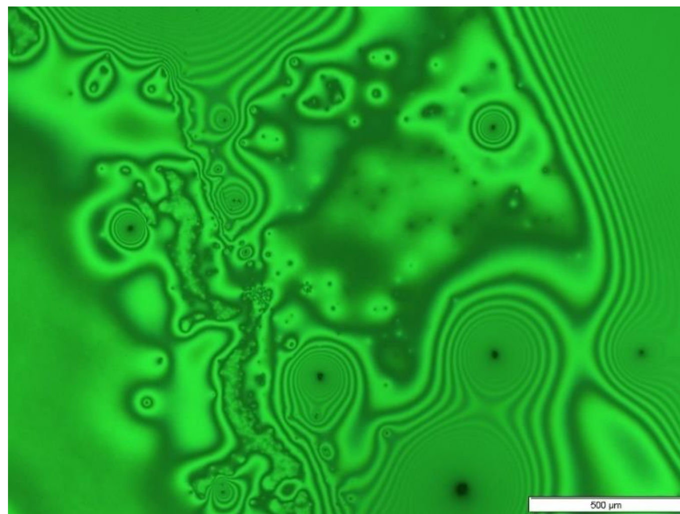

Figure 7.7: Interferometry image of octane pool edge on smooth silicon wafer after ultrasonic cleaning A captured during Meniscus test 3

A syringe with a needle of 1 inch length has been used for this test, that largely cover the hole of 16.13mm length; this let the manual filling of the chamber more fast, easy and accurate, since the pressure for injecting octane was very low and controlled.

The waiting time to allow equilibrium was longer than the previous test, namely 2 hours (for each filling), in order to check if the meniscus reached more stability and uniformity of profile.

Regarding the leaking problem through the hole, a sealing solution has been adopted: a micro-O-ring gasket for the needle, 0.3 mm thick and with inside diameter of 0.5 mm, has been tried. This aid has not succeeded in sealing the chamber and it was not sufficient to avoid the leaking of octane, indeed even worst than using the syringe without it. For this reason, the test has been performed for pool at 30%, 35%, and 40% the length of the wafer, instead of initial established amount of 40%, 50%, 60%; for the second and third filling, the meniscus largely receded due to the leaking from the micro hole and the volume of octane was reduced a lot during the waiting time, and not respected the initial percentage. In fact, for amount of volume greater than about 30%, the meniscus does not reach a steady state and continue to slowly and constantly recede until the pool no longer covers the hole.

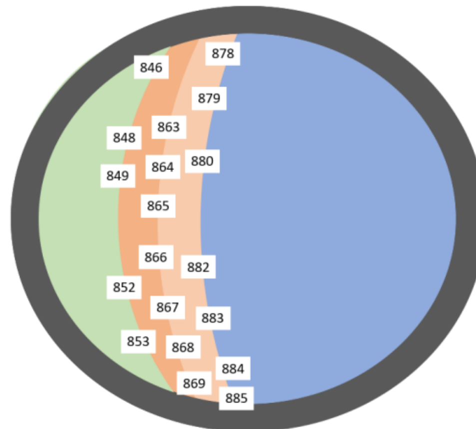

Figure 7.8: Schematic of locations of interferometry images in viewing window of closed chamber for Meniscus test 3

Volume %	Image	Curvature 1	Curvature 2	Curvature 3	Curvature 4	Average	Mean Error
unit of measure		1/µm	1/µm	1/µm	1/µm	1/µm	1/µm
30	846	1.67E-04	1.82E-04	1.93E-04	1.64E-04	1.76E-04	1.12E-05
	848	2.92E-05	5.30E-05	4.87E-05	3.22E-05	4.08E-05	1.00E-05
	849	3.55E-05	4.45E-05	3.23E-05	3.43E-05	3.66E-05	3.92E-06
	852	2.91E-05	3.07E-05	2.56E-05	4.76E-05	3.32E-05	7.18E-06
	853	3.58E-05	3.57E-05	3.65E-05	3.57E-05	3.59E-05	3.03E-07
	Average					6.46E-05	4.47E-05
35	863	3.23E-05	3.42E-05	3.08E-05	3.16E-05	3.22E-05	1.03E-06
	864	3.42E-05	3.41E-05	3.49E-05	3.53E-05	3.46E-05	5.03E-07
	865	3.43E-05	3.49E-05	3.15E-05	3.17E-05	3.31E-05	1.51E-06
	866	1.99E-05	1.95E-05	2.25E-05	1.98E-05	2.04E-05	1.04E-06
	867	2.62E-05	2.51E-05	2.64E-05	2.62E-05	2.60E-05	4.54E-07
	868	3.25E-05	2.96E-05	3.31E-05	2.73E-05	3.06E-05	2.17E-06
	869	2.14E-05	3.67E-05	6.52E-05	2.87E-05	3.80E-05	1.36E-05
	Average					3.07E-05	4.32E-06
40	878	7.86E-05	3.74E-05	3.06E-05	9.15E-05	5.95E-05	2.55E-05
	879	2.84E-05	2.92E-05	3.00E-05	2.86E-05	2.91E-05	5.28E-07
	880	2.948E-05	2.99E-05	2.66E-05	2.74E-05	2.83E-05	1.31E-06
	882	2.05E-05	2.46E-05	2.19E-05	2.48E-05	2.30E-05	1.75E-06
	883	3.00E-05	2.94E-05	2.79E-05	2.97E-05	2.93E-05	6.55E-07
	884	6.23E-05	4.67E-05	6.20E-05	5.70E-05	5.70E-05	5.16E-06
	885	1.07E-04	9.21E-05	4.19E-05	1.05E-04	8.64E-05	2.23E-05
	Average					4.46E-05	1.97E-05
Average						4.66E-05	1.69E-05

Table 7.3: Curvature measured for Meniscus test 3

7.4. MENISCUS TEST 4

The silicon wafer used in the Meniscus test number 4 has been cleaned with the ultrasonic cleaning (B). Even if the results were better than the procedure (A), the wafer was still not adequately clean, and a lot of dust impurities were present on the substrate.

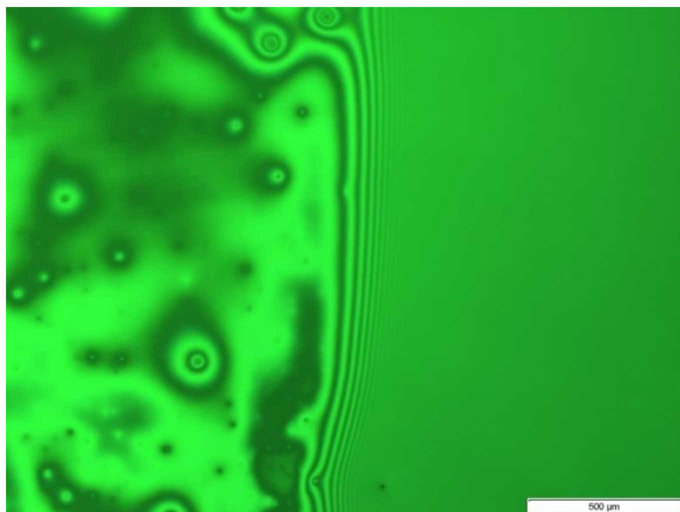

Figure 7.9: Interferometry image of octane pool edge on smooth silicon wafer after ultrasonic cleaning B captured during Meniscus test 4

The waiting time to allow equilibrium was 2 hours for all the three filling, as for the previous test. Instead of the micro-O-ring, the micro-hole has been sealed with a Teflon tape. Since the meniscus kept reducing and the problem of leaking has not been solved, here again the initial amount of octane has not been respected and the test has been stopped after the second filling.

The following results are referred to pool at 25% (first filling) and 40% (second filling) the length of the wafer.

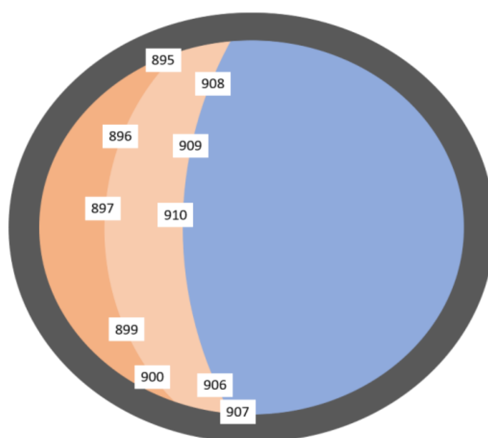

Figure 7.10: Schematic of locations of interferometry images in viewing window of closed chamber for Meniscus test 4

Volume %	Image	Curvature 1	Curvature 2	Curvature 3	Curvature 4	Average	Mean Error
unit of measure		1/µm	1/µm	1/µm	1/µm	1/µm	1/µm
25	895	1.59E-04	1.62E-04	1.25E-04	1.52E-04	1.49E-04	1.21E-05
	896	5.76E-05	6.45E-05	1.53E-05	5.83E-05	4.89E-05	1.68E-05
	897	3.19E-05	2.10E-05	3.31E-05	3.62E-05	3.05E-05	4.78E-06
	899	3.33E-05	3.25E-05	3.06E-05	3.24E-05	3.22E-05	7.89E-07
	900	6.04E-05	5.26E-05	5.07E-05	5.15E-05	5.38E-05	3.31E-06
	Average					6.30E-05	3.46E-05
40	908	7.81E-05	2.89E-05	6.79E-05	3.97E-05	5.36E-05	1.93E-05
	909	5.50E-05	7.36E-05	7.45E-05	6.87E-05	6.79E-05	6.45E-06
	910	4.08E-05	2.42E-05	4.19E-05	4.01E-05	3.67E-05	6.27E-06
	906	7.32E-05	6.76E-05	6.31E-05	6.81E-05	6.80E-05	2.62E-06
	907	8.82E-05	1.22E-04	1.25E-04	1.19E-04	1.13E-04	1.26E-05
	Average					6.79E-05	1.82E-05
Average						6.55E-05	2.48E-06

Table 7.4: Curvature measured for Meniscus test 4

7.5. MENISCUS TEST 5

The silicon wafer used in the meniscus test number 5 has been subject to the Piranha cleaning. The waiting time to allow equilibrium was 2 hours, as for the previous test.

The sealing solution adopted for this test was to just use a piece of rubber: once the desire volume of liquid inside the chamber has been reached, the syringe was removed, and the micro hole was sealed with a piece of Teflon attached with some adhesive tape. The Teflon piece was detached to allow the next filling and attached again after finishing. This solution enabled the meniscus to stop reducing and maintain a controlled volume, achieving a steady state.

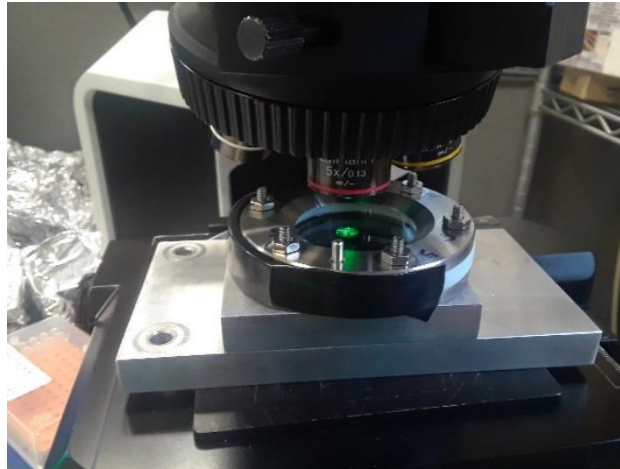

Figure 7.11: Experimental setup during Meniscus test 5 with piece of rubber as sealing solution

The test has been performed for pool at 40%, 50% and 65% the length of the wafer; the percentage of volume has been reduced to a smaller range, closer to the center (50%), since the results showed that the effect of the chamber edges affect the measurement for meniscus profile close to the lateral vertical wall.

Also, for the next test, the volume range has been varied in order to check the consistency of results in relation to different pool position.

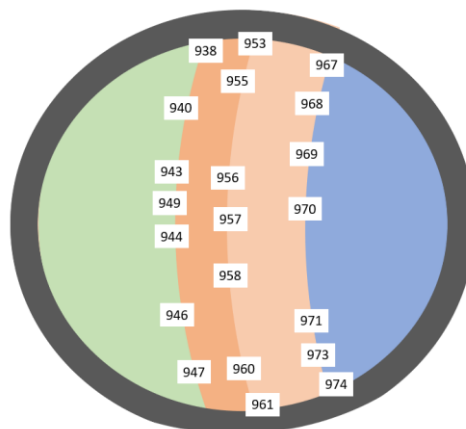

Figure 7.12: Schematic of locations of interferometry images in viewing window of closed chamber for Meniscus test 5

Volume %	Image	Curvature 1	Curvature 2	Curvature 3	Curvature 4	Average	Mean Error
unit of measure		1/µm	1/µm	1/µm	1/µm	1/µm	1/µm
40	938	1.94E-04	1.92E-04	1.89E-04	1.81E-04	1.89E-04	3.98E-06
	940	1.72E-05	1.06E-05	1.72E-05	1.56E-05	1.51E-05	2.28E-06
	943	1.93E-05	1.90E-05	1.84E-05	1.82E-05	1.87E-05	4.34E-07
	949	2.70E-05	1.23E-05	1.79E-05	2.61E-05	2.08E-05	5.72E-06
	944	1.46E-05	1.37E-05	1.43E-05	1.45E-05	1.43E-05	2.97E-07
	946	2.71E-05	2.58E-05	1.72E-05	2.44E-05	2.36E-05	3.21E-06
	947	3.49E-05	3.08E-05	3.17E-05	3.37E-05	3.28E-05	1.52E-06
	Average					4.49E-05	4.12E-05
50	953	1.09E-04	6.07E-05	5.42E-05	1.15E-04	8.48E-05	2.74E-05
	955	2.79E-05	2.26E-05	2.88E-05	3.00E-05	2.73E-05	2.38E-06
	956	1.44E-05	1.40E-05	1.49E-05	1.46E-05	1.45E-05	2.57E-07
	957	2.48E-05	2.13E-05	1.47E-05	1.78E-05	1.97E-05	3.40E-06
	958	2.53E-05	2.50E-05	2.53E-05	2.43E-05	2.50E-05	3.32E-07
	960	2.94E-05	3.41E-05	3.02E-05	3.41E-05	3.19E-05	2.16E-06
	961	6.23E-05	6.50E-05	6.84E-05	6.69E-05	6.57E-05	1.99E-06
	Average					3.84E-05	2.10E-05
65	967	5.05E-05	7.07E-05	7.16E-05	7.90E-05	6.79E-05	8.74E-06
	968	2.87E-05	2.95E-05	2.97E-05	2.96E-05	2.94E-05	3.26E-07
	969	2.27E-05	2.10E-05	2.28E-05	2.30E-05	2.24E-05	6.87E-07
	970	2.23E-05	2.30E-05	2.38E-05	2.39E-05	2.33E-05	6.01E-07
	971	2.39E-05	2.51E-05	2.59E-05	2.47E-05	2.49E-05	5.95E-07
	973	3.34E-05	3.32E-05	3.30E-05	3.38E-05	3.34E-05	2.37E-07
	974	3.40E-05	2.62E-05	3.49E-05	3.36E-05	3.22E-05	2.97E-06
	Average					3.33E-05	9.89E-06
Average						3.89E-05	5.78E-06

Table 7.5: Curvature measured for Meniscus test 5

7.6. MENISCUS TEST 6

The Meniscus test number 6 has been performed for pool at 35%, 45% and 55% the length of the wafer, and as for the previous test, the silicon wafer has been cleaned using the Piranha process.

The waiting time to allow equilibrium was 2 hours, for all the three filling.

The images set of the third filling has been taken a second time, after a waiting time of 20 hours; a comparison between the results of the two meniscus profiles has been made.

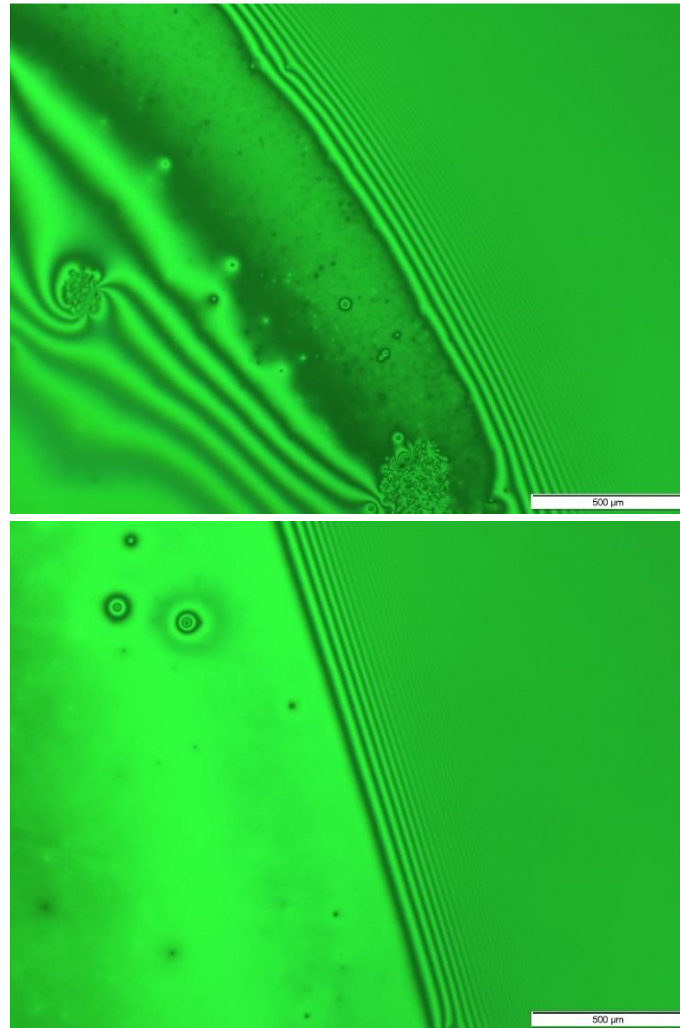

Figure 7.13: Interferometry images of octane pool edge captured during Meniscus test 6 after a waiting time of 2 hours (top) and 20 hours (bottom)

Better images and a clearer fringes pattern have been reached by extending the period of waiting. The meniscus attained a more uniform and stable profile; according to this, the curvature values show a lower dispersion and an evident consistency.

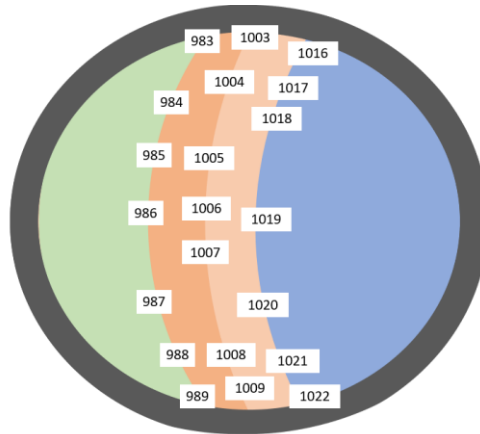

Figure 7.14: Schematic of locations of interferometry images in viewing window of closed chamber for Meniscus test 6

Volume %	Image	Curvature 1	Curvature 2	Curvature 3	Curvature 4	Average	Mean Error
unit of measure		1/μm	1/μm	1/μm	1/μm	1/μm	1/μm
35	983	3.13E-05	5.76E-05	1.06E-04	6.66E-05	6.53E-05	2.09E-05
	984	3.33E-05	3.28E-05	3.27E-05	3.25E-05	3.28E-05	2.20E-07
	985	3.00E-05	2.91E-05	2.78E-05	3.02E-05	2.93E-05	7.93E-07
	986	4.12E-05	3.63E-05	4.24E-05	3.50E-05	3.87E-05	3.07E-06
	987	3.93E-05	3.90E-05	3.75E-05	3.55E-05	3.78E-05	1.31E-06
	988	3.49E-05	3.52E-05	3.63E-05	3.61E-05	3.56E-05	5.69E-07
	989	6.97E-05	5.00E-05	7.05E-05	5.77E-05	6.20E-05	8.14E-06
	Average					4.31E-05	1.18E-05
45	1003	1.55E-05	3.46E-05	1.42E-05	7.84E-05	3.57E-05	2.14E-05
	1004	2.87E-05	2.94E-05	2.96E-05	3.09E-05	2.97E-05	6.47E-07
	1005	2.31E-05	2.30E-05	2.37E-05	2.30E-05	2.32E-05	2.51E-07
	1006	2.55E-05	2.51E-05	2.52E-05	2.57E-05	2.54E-05	2.15E-07
	1007	2.90E-05	3.40E-05	3.32E-05	2.87E-05	3.12E-05	2.39E-06
	1008	2.58E-05	2.48E-05	2.52E-05	2.40E-05	2.50E-05	5.52E-07
	1009	3.41E-05	3.35E-05	3.95E-05	3.96E-05	3.67E-05	2.89E-06
	Average					2.95E-05	4.95E-06
55 (2 hours)	1016	8.28E-05	9.29E-05	7.23E-05	7.36E-05	8.04E-05	7.45E-06
	1017	3.52E-05	3.47E-05	3.56E-05	3.51E-05	3.51E-05	2.26E-07
	1018	2.18E-05	2.32E-05	2.41E-05	2.17E-05	2.27E-05	9.18E-07
	1019	2.60E-05	2.70E-05	2.68E-05	2.76E-05	2.69E-05	4.47E-07
	1020	2.82E-05	2.78E-05	2.71E-05	2.82E-05	2.78E-05	3.63E-07
	1021	3.02E-05	2.93E-05	3.04E-05	3.11E-05	3.02E-05	5.22E-07
	1022	3.25E-05	3.64E-05	3.65E-05	3.63E-05	3.54E-05	1.44E-06
	Average					3.69E-05	1.24E-05
Average						3.65E-05	6.77E-06

Table 7.6: Curvature measured for Meniscus test 6, considering the lowest waiting time for third filling

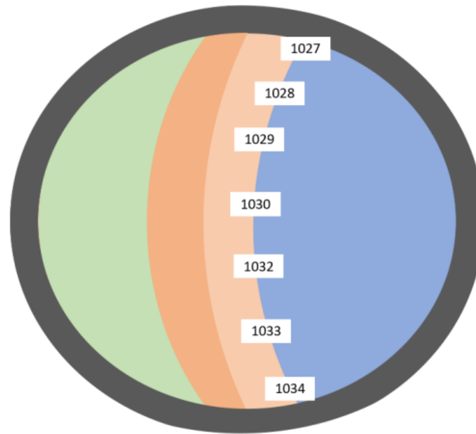

Figure 7.15: Schematic of locations of interferometry images in viewing window of closed chamber for third filling after a waiting time of 20 hours (Meniscus test 6)

Volume %	Image	Curvature 1	Curvature 2	Curvature 3	Curvature 4	Average	Mean Error
unit of measure		1/µm	1/µm	1/µm	1/µm	1/µm	1/µm
55 (2 hours)	1016	8.28E-05	9.29E-05	7.23E-05	7.36E-05	8.04E-05	7.45E-06
	1017	3.52E-05	3.47E-05	3.56E-05	3.51E-05	3.51E-05	2.26E-07
	1018	2.18E-05	2.32E-05	2.41E-05	2.17E-05	2.27E-05	9.18E-07
	1019	2.60E-05	2.70E-05	2.68E-05	2.76E-05	2.69E-05	4.47E-07
	1020	2.82E-05	2.78E-05	2.71E-05	2.82E-05	2.78E-05	3.63E-07
	1021	3.02E-05	2.93E-05	3.04E-05	3.11E-05	3.02E-05	5.22E-07
	1022	3.25E-05	3.64E-05	3.65E-05	3.63E-05	3.54E-05	1.44E-06
	Average					3.69E-05	1.24E-05
55 (20 hours)	1027	4.16E-05	7.50E-05	5.30E-05	5.87E-05	5.71E-05	9.80E-06
	1028	3.51E-05	2.23E-05	3.49E-05	3.48E-05	3.18E-05	4.75E-06
	1029	3.79E-05	3.02E-05	3.77E-05	3.69E-05	3.57E-05	2.73E-06
	1030	3.94E-05	3.62E-05	3.85E-05	3.65E-05	3.76E-05	1.32E-06
	1032	3.95E-05	4.31E-05	4.08E-05	4.34E-05	4.17E-05	1.54E-06
	1033	3.30E-05	3.31E-05	3.31E-05	3.33E-05	3.31E-05	7.94E-08
	1034	3.81E-05	3.90E-05	3.81E-05	3.88E-05	3.85E-05	3.87E-07
	Average					3.94E-05	5.73E-06
Average						3.81E-05	1.21E-06

Table 7.7: Curvature measured at different time for third filling of Meniscus test 6

7.7. MENISCUS TEST 7

The Meniscus test number 7 has been performed for pool at 30%, 50% and 60% the length of the wafer. The silicon wafer used in the test number 2 has been used after the ultrasonic cleaning (C).

The waiting time to allow equilibrium was 7 hours for the first amount of volume, 15 hours for the second and 32 hours for the last.

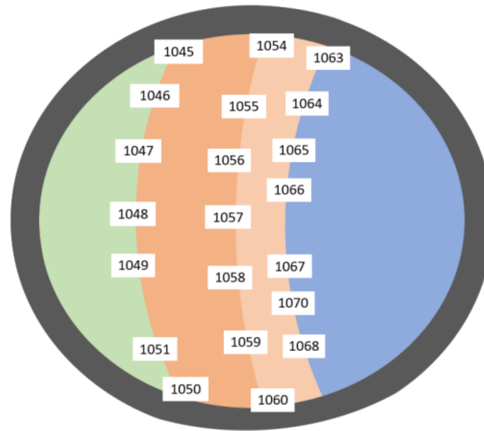

Figure 7.16: Schematic of locations of interferometry images in viewing window of closed chamber for Meniscus test 7

Volume %	Image	Curvature 1	Curvature 2	Curvature 3	Curvature 4	Average	Mean Error
unit of measure		1/µm	1/µm	1/µm	1/µm	1/µm	1/µm
30	1045	1.84E-04	1.86E-04	1.56E-04	1.81E-04	1.77E-04	1.06E-05
	1046	6.71E-05	6.54E-05	6.75E-05	6.32E-05	6.58E-05	1.50E-06
	1047	3.53E-05	3.56E-05	2.98E-05	3.54E-05	3.40E-05	2.10E-06
	1048	2.86E-05	2.99E-05	3.56E-05	3.30E-05	3.18E-05	2.52E-06
	1049	2.88E-05	3.18E-05	3.49E-05	3.61E-05	3.29E-05	2.60E-06
	1051	4.63E-05	4.76E-05	4.83E-05	4.95E-05	4.79E-05	9.74E-07
	1050	7.58E-05	6.49E-05	6.53E-05	7.54E-05	7.03E-05	5.22E-06
	Average					6.56E-05	3.31E-05
50	1054	5.69E-05	4.97E-05	4.93E-05	5.69E-05	5.32E-05	3.71E-06
	1055	2.32E-05	2.62E-05	2.55E-05	2.57E-05	2.51E-05	9.77E-07
	1056	2.18E-05	2.35E-05	2.02E-05	2.31E-05	2.22E-05	1.13E-06
	1057	2.50E-05	2.43E-05	2.37E-05	2.37E-05	2.41E-05	4.79E-07
	1058	2.55E-05	2.21E-05	2.71E-05	2.50E-05	2.49E-05	1.42E-06
	1059	2.60E-05	2.76E-05	2.69E-05	2.70E-05	2.69E-05	4.45E-07
	1060	2.62E-05	2.65E-05	2.60E-05	2.52E-05	2.60E-05	3.72E-07

	Average					2.89E-05	6.94E-06
60	1063	5.43E-05	5.42E-05	4.26E-05	5.64E-05	5.19E-05	4.64E-06
	1064	2.78E-05	2.59E-05	2.65E-05	2.72E-05	2.69E-05	6.43E-07
	1065	2.53E-05	2.61E-05	2.64E-05	2.64E-05	2.61E-05	3.81E-07
	1066	2.82E-05	2.76E-05	2.70E-05	2.75E-05	2.76E-05	3.02E-07
	1067	2.44E-05	2.24E-05	2.30E-05	2.16E-05	2.28E-05	8.50E-07
	1070	3.04E-05	2.99E-05	3.00E-05	3.06E-05	3.02E-05	2.61E-07
	1068	2.63E-05	2.52E-05	2.61E-05	2.66E-05	2.61E-05	4.07E-07
	Average					3.02E-05	6.20E-06
Average						4.16E-05	1.84E-05

Table 7.8: Curvature measured for Meniscus test 7

7.8. MENISCUS TEST 8

The Meniscus test number 8 has been performed for pool at 40%, 50% and 60% the length of the wafer. The silicon wafer used in the test number 1 has been used after the ultrasonic cleaning (C).

The waiting time to allow equilibrium was 17 hours for the first amount of volume, 7.5 hours for the second and 15 hours for the last.

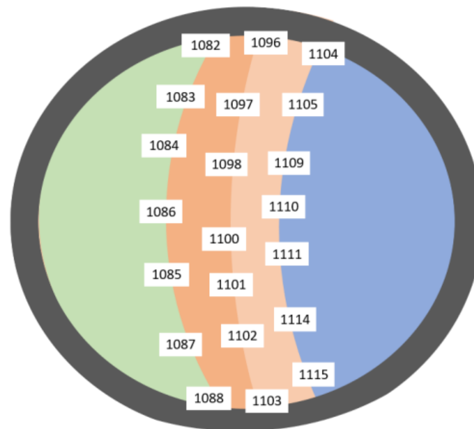

Figure 7.17: Schematic of locations of interferometry images in viewing window of closed chamber for Meniscus test 8

Volume %	Image	Curvature 1	Curvature 2	Curvature 3	Curvature 4	Average	Mean Error
unit of measure		1/µm	1/µm	1/µm	1/µm	1/µm	1/µm
40	1082	1.69E-04	1.80E-04	1.60E-04	1.70E-04	1.70E-04	5.50E-06
	1083	2.96E-05	3.82E-05	4.09E-05	3.12E-05	3.50E-05	4.57E-06
	1084	4.19E-05	4.25E-05	3.60E-05	4.05E-05	4.02E-05	2.13E-06
	1086	3.22E-05	3.18E-05	3.17E-05	3.25E-05	3.20E-05	3.16E-07
	1085	2.89E-05	3.02E-05	2.94E-05	2.91E-05	2.94E-05	4.23E-07
	1087	3.54E-05	3.16E-05	3.25E-05	3.15E-05	3.27E-05	1.31E-06
	1088	2.12E-05	5.32E-05	5.52E-05	5.81E-05	4.69E-05	1.29E-05
	Average					5.51E-05	3.27E-05
50	1096	1.03E-04	1.20E-04	9.76E-05	8.78E-05	1.02E-04	9.41E-06
	1097	2.65E-05	2.57E-05	2.68E-05	2.73E-05	2.66E-05	4.56E-07
	1098	3.79E-05	3.68E-05	3.36E-05	3.57E-05	3.60E-05	1.34E-06
	1100	2.73E-05	2.50E-05	2.68E-05	2.45E-05	2.59E-05	1.15E-06
	1101	2.74E-05	2.71E-05	2.59E-05	2.76E-05	2.70E-05	5.46E-07
	1102	2.94E-05	3.08E-05	3.20E-05	2.97E-05	3.05E-05	9.37E-07
	1103	4.30E-05	3.91E-05	4.41E-05	4.00E-05	4.16E-05	2.01E-06
	Average					4.14E-05	1.74E-05
60	1104	6.93E-05	7.22E-05	6.69E-05	7.25E-05	7.02E-05	2.14E-06
	1105	3.24E-05	3.39E-05	3.42E-05	3.37E-05	3.35E-05	5.95E-07
	1109	3.40E-05	3.62E-05	3.57E-05	3.37E-05	3.49E-05	1.04E-06
	1110	2.45E-05	2.37E-05	2.33E-05	2.25E-05	2.35E-05	5.71E-07
	1111	4.97E-05	4.18E-05	4.27E-05	4.66E-05	4.52E-05	2.96E-06
	1114	2.45E-05	2.47E-05	2.23E-05	2.38E-05	2.38E-05	7.56E-07
	1115	2.91E-05	3.05E-05	2.91E-05	3.11E-05	2.99E-05	8.33E-07
	Average					3.29E-05	1.17E-05
Average						4.31E-05	1.11E-05

Table 7.9: Curvature measured for Meniscus test 8

7.9. MENISCUS TEST 9

The Meniscus test number 9 has been performed for pool at 40%, 50% and 60% the length of the wafer. The silicon wafer has been cleaned using the ultrasonic cleaning (C).
The waiting time to allow equilibrium was 6 hours for the first amount of volume, 15 hours for the second and 18 hours for the last.

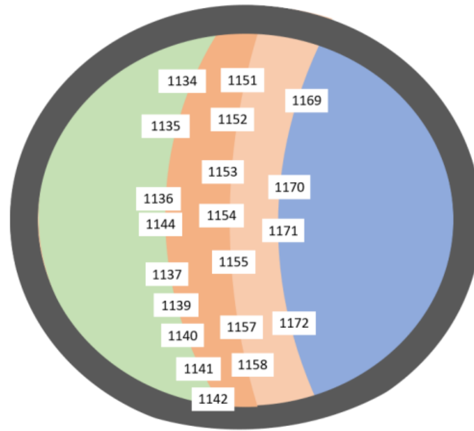

Figure 7.18: Schematic of locations of interferometry images in viewing window of closed chamber for Meniscus test 9

Volume %	Image	Curvature 1	Curvature 2	Curvature 3	Curvature 4	Average	Mean Error
unit of measure		1/µm	1/µm	1/µm	1/µm	1/µm	1/µm
40	1134	1.30E-05	1.40E-05	1.34E-05	1.37E-05	1.35E-05	3.11E-07
	1135	1.74E-05	1.74E-05	1.95E-05	1.62E-05	1.76E-05	9.23E-07
	1136	3.56E-05	3.59E-05	3.54E-05	3.43E-05	3.53E-05	4.81E-07
	1137	3.09E-05	3.32E-05	3.05E-05	3.17E-05	3.16E-05	8.83E-07
	1139	3.02E-05	2.88E-05	3.05E-05	2.96E-05	2.98E-05	5.88E-07
	1140	3.14E-05	3.13E-05	2.53E-05	3.54E-05	3.09E-05	2.78E-06
	1141	2.93E-05	3.13E-05	3.13E-05	2.96E-05	3.04E-05	9.20E-07
	1142	2.42E-05	2.42E-05	5.35E-05	5.30E-05	3.87E-05	1.45E-05
	1144	2.80E-05	2.78E-05	2.77E-05	2.91E-05	2.81E-05	4.84E-07
	Average					2.84E-05	5.78E-06
50	1151	2.75E-05	2.89E-05	3.03E-05	2.71E-05	2.84E-05	1.12E-06
	1152	2.63E-05	1.49E-05	2.55E-05	2.79E-05	2.37E-05	4.40E-06
	1153	3.40E-05	3.18E-05	3.32E-05	3.33E-05	3.31E-05	6.54E-07
	1154	2.32E-05	2.42E-05	2.43E-05	2.31E-05	2.37E-05	5.49E-07

	1155	3.54E-05	3.25E-05	3.66E-05	3.08E-05	3.38E-05	2.18E-06
	1157	3.37E-05	3.47E-05	3.47E-05	2.51E-05	3.20E-05	3.48E-06
	1158	3.29E-05	2.69E-05	3.90E-05	3.56E-05	3.36E-05	3.70E-06
	Average					2.98E-05	3.85E-06
60	1169	2.93E-05	2.76E-05	3.00E-05	2.79E-05	2.87E-05	9.57E-07
	1170	2.37E-05	2.14E-05	2.68E-05	2.85E-05	2.51E-05	2.57E-06
	1171	2.06E-05	2.26E-05	2.43E-05	2.33E-05	2.27E-05	1.07E-06
	1172	3.16E-05	3.19E-05	2.73E-05	3.33E-05	3.10E-05	1.86E-06
	Average					2.69E-05	2.98E-06
Average						2.84E-05	1.44E-06

Table 7.10: Curvature measured for Meniscus test 9

7.10. MENISCUS TEST 10

The Meniscus test number 10 has been performed for pool at 40%, 50% and 60% the length of the wafer. A new fresh silicon wafer has been used.
For the first amount of volume, the interferometry images have been taken at different moment: one time after 6 hours and the second time after 28 hours.

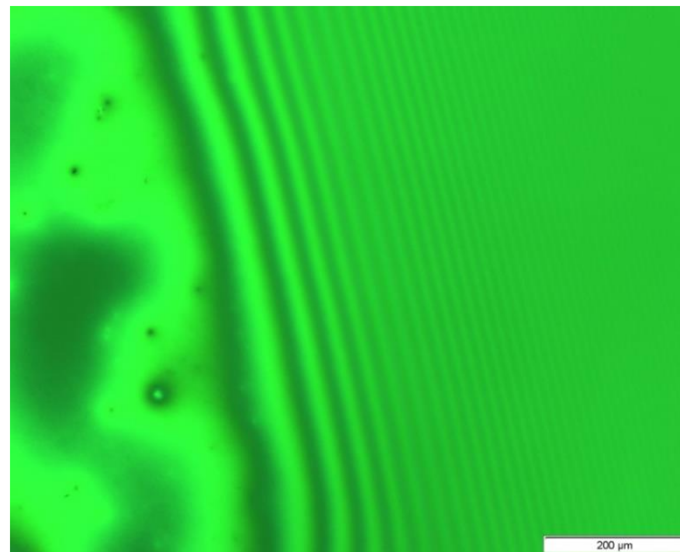

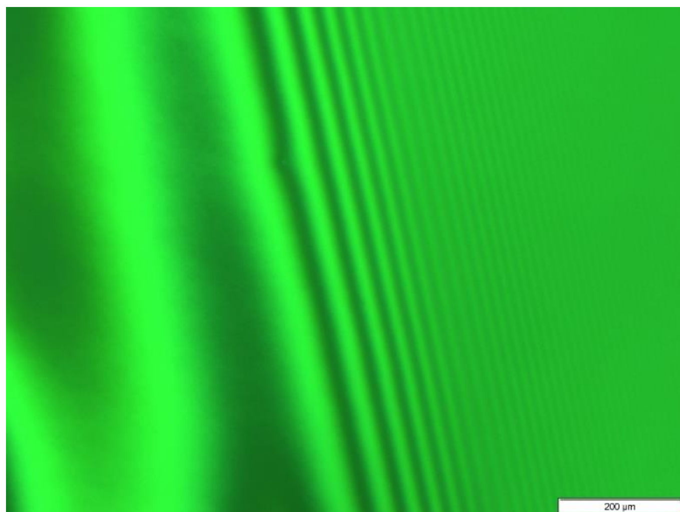

Figure 7.19: Interferometry images of octane pool edge captured during Meniscus test 10 after a waiting time of 6 hours (top) and 28 hours (bottom)

It is concluded that 6 hours is a sufficient time for the meniscus to reach equilibrium, since any significant differences have been found between the 2 different set of images. The waiting time to allow equilibrium was 7 hours for the second amount of volume, 12 hours for the last.

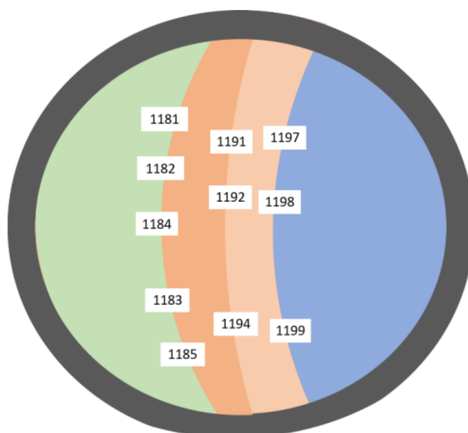

Figure 7.20: Schematic of locations of interferometry images in viewing window of closed chamber for Meniscus test 10

Volume %	Image	Curvature 1	Curvature 2	Curvature 3	Curvature 4	Average	Mean Error
unit of measure		1/μm	1/μm	1/μm	1/μm	1/μm	1/μm
40 (6 hours)	1181	2.45E-05	2.37E-05	2.55E-05	2.31E-05	2.42E-05	8.14E-07
	1182	1.77E-05	2.24E-05	1.94E-05	2.28E-05	2.06E-05	2.05E-06
	1183	2.70E-05	2.68E-05	2.13E-05	2.84E-05	2.59E-05	2.29E-06
	1184	2.61E-05	2.36E-05	2.47E-05	2.58E-05	2.51E-05	9.18E-07
	1185	2.56E-05	2.55E-05	2.62E-05	2.54E-05	2.57E-05	2.44E-07
	Average					2.43E-05	1.52E-06
50	1191	2.54E-05	2.57E-05	2.51E-05	2.59E-05	2.55E-05	2.61E-07
	1192	2.34E-05	2.50E-05	2.55E-05	2.54E-05	2.49E-05	7.08E-07
	1194	2.39E-05	2.25E-05	2.29E-05	2.23E-05	2.29E-05	4.94E-07
	Average					2.44E-05	1.03E-06
60	1197	2.57E-05	2.48E-05	2.62E-05	2.59E-05	2.56E-05	4.37E-07
	1198	2.60E-05	2.59E-05	2.43E-05	2.58E-05	2.55E-05	5.87E-07
	1199	2.15E-05	2.11E-05	2.14E-05	2.14E-05	2.14E-05	1.34E-07
	Average					2.42E-05	1.88E-06
Average						2.43E-05	1.32E-07

Table 7.11: Curvature measured for Meniscus test 10, considering the lowest waiting time for first filling

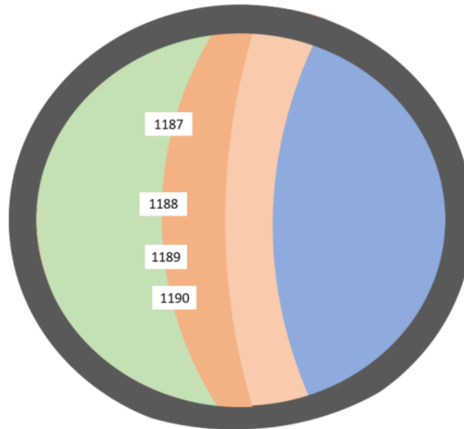

Figure 7.21: Schematic of locations of interferometry images in viewing window of closed chamber for first filling after a waiting time of 28 hours (Meniscus test 10)

Volume %	Image	Curvature 1	Curvature 2	Curvature 3	Curvature 4	Average	Mean Error
unit of measure		1/μm	1/μm	1/μm	1/μm	1/μm	1/μm
40 (6 hours)	1181	2.45E-05	2.37E-05	2.55E-05	2.31E-05	2.42E-05	8.14E-07
	1182	1.77E-05	2.24E-05	1.94E-05	2.28E-05	2.06E-05	2.05E-06
	1183	2.70E-05	2.68E-05	2.13E-05	2.84E-05	2.59E-05	2.29E-06
	1184	2.61E-05	2.36E-05	2.47E-05	2.58E-05	2.51E-05	9.18E-07
	1185	2.56E-05	2.55E-05	2.62E-05	2.54E-05	2.57E-05	2.44E-07
	Average					2.43E-05	1.52E-06
40 (28 hours)	1187	2.72E-05	2.67E-05	2.71E-05	2.67E-05	2.69E-05	2.29E-07
	1188	2.61E-05	2.82E-05	2.33E-05	2.88E-05	2.66E-05	1.93E-06
	1189	2.59E-05	2.47E-05	2.44E-05	2.20E-05	2.42E-05	1.12E-06
	1190	3.03E-05	2.92E-05	2.82E-05	2.91E-05	2.92E-05	5.79E-07
	Average					2.67E-05	1.32E-06
Average						2.55E-05	1.22E-06

Table 7.12: Curvature measured at different time for first filling of Meniscus test 10

7.11. MENISCUS TEST 11

The Meniscus test number 11 has been performed for pool at 25%, 50% and 70% the length of the wafer. A new fresh silicon wafer has been used. The waiting time to allow equilibrium was 24 hours for the first amount of volume, 5.5 hours for the second and 19.5 hours for the last.

A relatively small piece of dust that was probably due to the octane's contamination has been found in the volume of fluid.

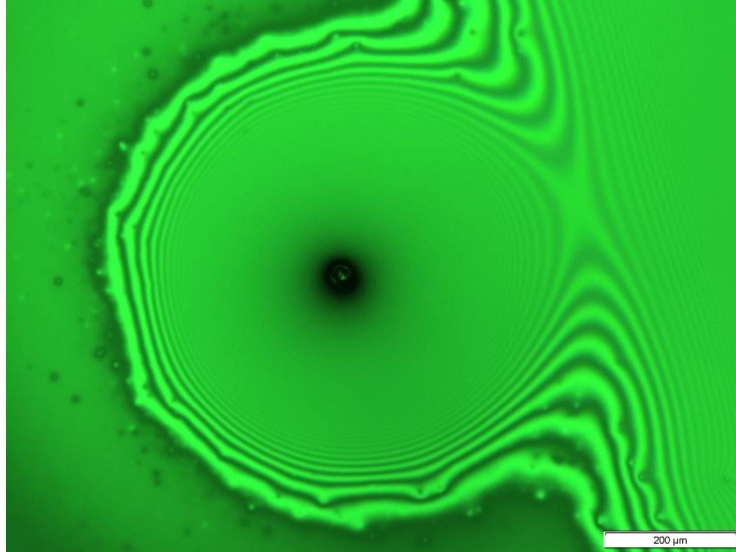

Figure 7.22: Dust particle affecting octane pool edge during Meniscus test 11

Figure 7.23: Disassembled chamber after Meniscus test 11 with dust particles in octane pool

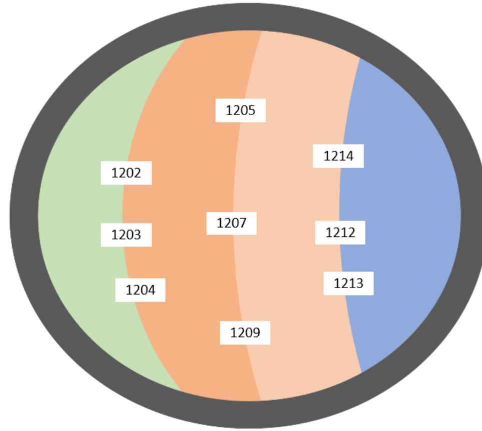

Figure 7.24: Schematic of locations of interferometry images in viewing window of closed chamber for Meniscus test 11

Volume %	Image	Curvature 1	Curvature 2	Curvature 3	Curvature 4	Average	Mean Error
unit of measure		1/µm	1/µm	1/µm	1/µm	1/µm	1/µm
25	1202	3.56E-05	3.64E-05	3.54E-05	3.60E-05	3.59E-05	3.42E-07
	1203	3.14E-05	3.47E-05	3.33E-05	3.21E-05	3.29E-05	1.13E-06
	1204	3.24E-05	3.33E-05	3.25E-05	3.37E-05	3.30E-05	5.26E-07
	Average					3.39E-05	1.30E-06
50	1205	2.79E-05	2.77E-05	2.98E-05	2.85E-05	2.85E-05	6.53E-07
	1207	2.15E-05	2.64E-05	2.57E-05	2.07E-05	2.36E-05	2.47E-06
	1209	2.42E-05	2.39E-05	2.33E-05	2.40E-05	2.39E-05	2.58E-07
	Average					2.53E-05	2.10E-06
70	1212	2.57E-05	2.48E-05	2.87E-05	2.76E-05	2.67E-05	1.42E-06
	1213	2.58E-05	2.37E-05	2.62E-05	2.71E-05	2.57E-05	9.99E-07
	1214	2.48E-05	2.35E-05	2.23E-05	2.34E-05	2.35E-05	6.40E-07
	Average					2.53E-05	1.20E-06
Average						2.82E-05	4.30E-06

Table 7.13: Curvature measured for Meniscus test 11

7.12. MENISCUS TEST 12

The Meniscus test number 12 has been performed for pool at 40%, 45% and 55% the length of the wafer. A new fresh silicon wafer has been used. The waiting time to allow equilibrium was 6.5 hours for the first amount of volume, 51.5 hours for the second and 8.5 hours for the last.

After the disassembly, a little crack has been noticed at the edge of the wafer.

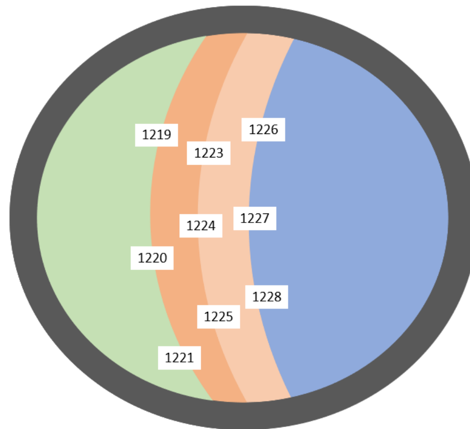

Figure 7.25: Schematic of locations of interferometry images in viewing window of closed chamber for Meniscus test 12

Volume %	Image	Curvature 1	Curvature 2	Curvature 3	Curvature 4	Average	Mean Error
unit of measure		1/µm	1/µm	1/µm	1/µm	1/µm	1/µm
40	1219	2.67E-05	2.80E-05	2.84E-05	2.68E-05	2.75E-05	7.27E-07
	1220	2.32E-05	2.61E-05	2.49E-05	2.59E-05	2.50E-05	9.73E-07
	1221	2.88E-05	2.82E-05	2.69E-05	2.82E-05	2.80E-05	5.37E-07
	Average					2.68E-05	1.21E-06
45	1223	2.89E-05	2.84E-05	2.89E-05	2.88E-05	2.88E-05	1.66E-07
	1224	2.65E-05	2.65E-05	2.63E-05	2.68E-05	2.65E-05	1.34E-07
	1225	2.20E-05	2.52E-05	2.51E-05	2.47E-05	2.42E-05	1.14E-06
	Average					2.65E-05	1.51E-06
55	1226	3.03E-05	3.05E-05	2.88E-05	2.99E-05	2.99E-05	5.27E-07
	1227	2.38E-05	2.34E-05	2.37E-05	2.43E-05	2.38E-05	2.75E-07
	1228	2.23E-05	2.47E-05	2.38E-05	2.33E-05	2.35E-05	7.41E-07
	Average					2.57E-05	2.76E-06
Average						2.64E-05	5.53E-07

Table 7.14: Curvature measured for Meniscus test 12

7.13. MENISCUS TEST 13

The Meniscus test number 13 has been performed for pool at 45% and 55% the length of the wafer. A new fresh silicon wafer has been used. The waiting time to allow equilibrium was 6.5 hours for the first amount of volume and 42 hours for the second.

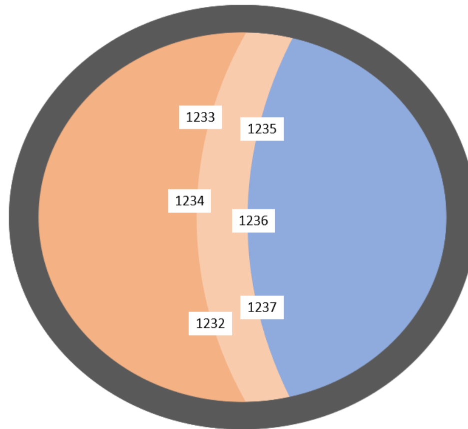

Figure 7.26: Schematic of locations of interferometry images in viewing window of closed chamber for Meniscus test 13

Volume %	Image	Curvature 1	Curvature 2	Curvature 3	Curvature 4	Average	Mean Error
unit of measure		1/µm	1/µm	1/µm	1/µm	1/µm	1/µm
45	1232	2.93E-05	2.84E-05	3.01E-05	2.89E-05	2.92E-05	5.12E-07
	1233	2.39E-05	2.28E-05	2.63E-05	2.33E-05	2.41E-05	1.12E-06
	1234	2.36E-05	2.66E-05	2.42E-05	2.65E-05	2.52E-05	1.35E-06
	Average					2.62E-05	2.01E-06
55	1235	2.92E-05	2.95E-05	2.93E-05	2.90E-05	2.92E-05	1.55E-07
	1236	3.75E-05	3.91E-05	3.79E-05	3.68E-05	3.78E-05	6.69E-07
	1237	2.81E-05	2.86E-05	2.87E-05	2.75E-05	2.82E-05	4.13E-07
	Average					3.18E-05	4.05E-06
Average						2.90E-05	2.80E-06

Table 7.15: Curvature measured for Meniscus test 13

7.14. MENISCUS TEST 14

The Meniscus test number 14 has been performed for pool at 45% and 55% the length of the wafer. A new fresh silicon wafer has been used. The waiting time to allow equilibrium was 6 hours for the first amount of volume and 16 hours for the second.

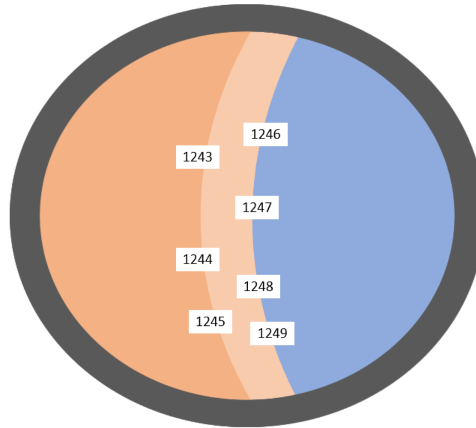

Figure 7.27: Schematic of locations of interferometry images in viewing window of closed chamber for Meniscus test 14

Volume %	Image	Curvature 1	Curvature 2	Curvature 3	Curvature 4	Average	Mean Error
unit of measure		1/µm	1/µm	1/µm	1/µm	1/µm	1/µm
45	1243	2.37E-05	2.43E-05	2.43E-05	2.33E-05	2.39E-05	3.93E-07
	1244	2.35E-05	2.14E-05	2.17E-05	2.28E-05	2.23E-05	8.08E-07
	1245	2.14E-05	2.17E-05	2.22E-05	2.06E-05	2.15E-05	4.71E-07
	Average					2.26E-05	8.86E-07
55	1246	2.24E-05	2.33E-05	2.39E-05	2.24E-05	2.30E-05	5.91E-07
	1247	2.37E-05	2.20E-05	2.24E-05	2.27E-05	2.27E-05	5.12E-07
	1248	2.15E-05	2.51E-05	2.31E-05	2.26E-05	2.31E-05	1.03E-06
	1249	2.40E-05	2.28E-05	2.45E-05	2.37E-05	2.37E-05	4.75E-07
	Average					2.31E-05	3.10E-07
Average						2.28E-05	2.73E-07

Table 7.16: Curvature measured for Meniscus test 14

8. RESULTS AND DISCUSSION

8.1. RECEDING MENISCUS

Considering only the test with the effective sealing solution (from Meniscus test 5 onwards), 6 hours has been found the sufficient time to allow the meniscus for receding and stabilizing, reaching the steady state (nonevaporating condition). In 6 hours, the meniscus recedes from about 150 to 200 μm.

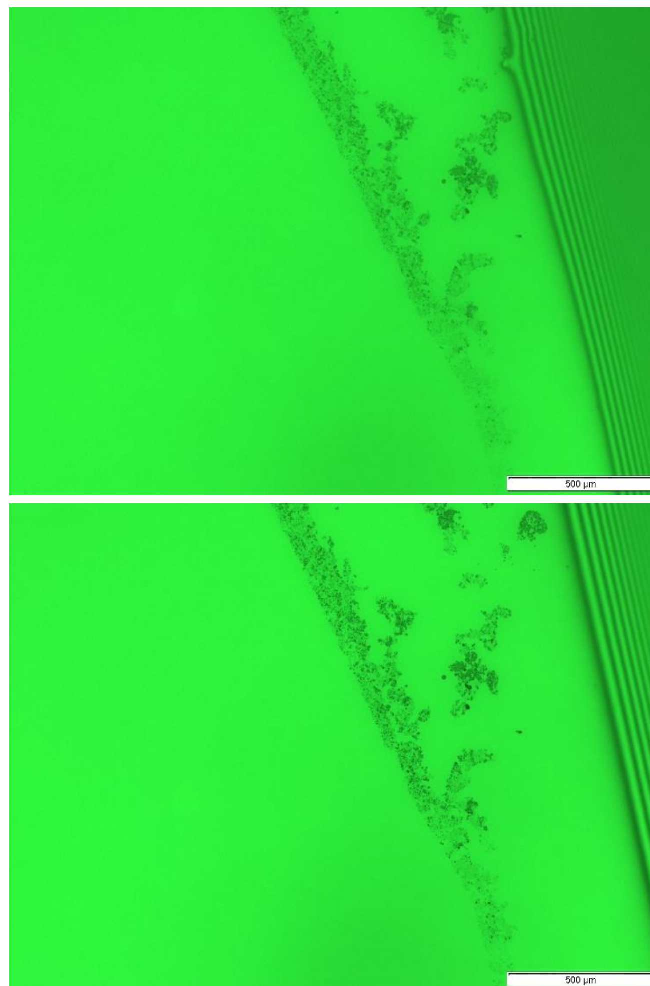

Figure 8.1: Interferometry images of receding meniscus: shortly after filling (top); after 6 hours (bottom)

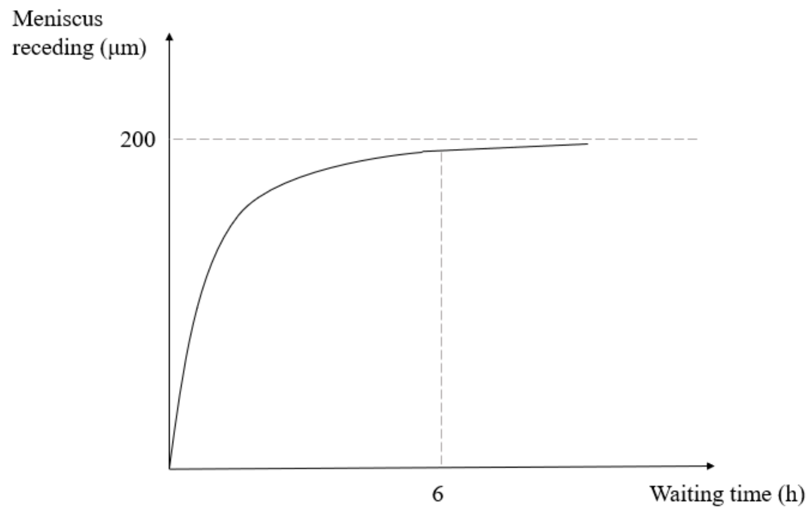

Figure 8.2: Amount of receding meniscus (microns) vs waiting time to reach the steady state

8.2. CLEANING PROCESS

The ultrasonic cleaning procedure (C) is found to produce the best results. It is evident not only from more clear interferometry images, but also with more consistent results; being the pool edge more uniform, the 4 values of curvature have a lower deviation for each processed image.

The graph reported below is refers to the mean error between 4 values of curvature of the same interferometry image, representing the errors associated with measuring the curvature; the average of the mean error of the images set for different pool positions for each test is reported.

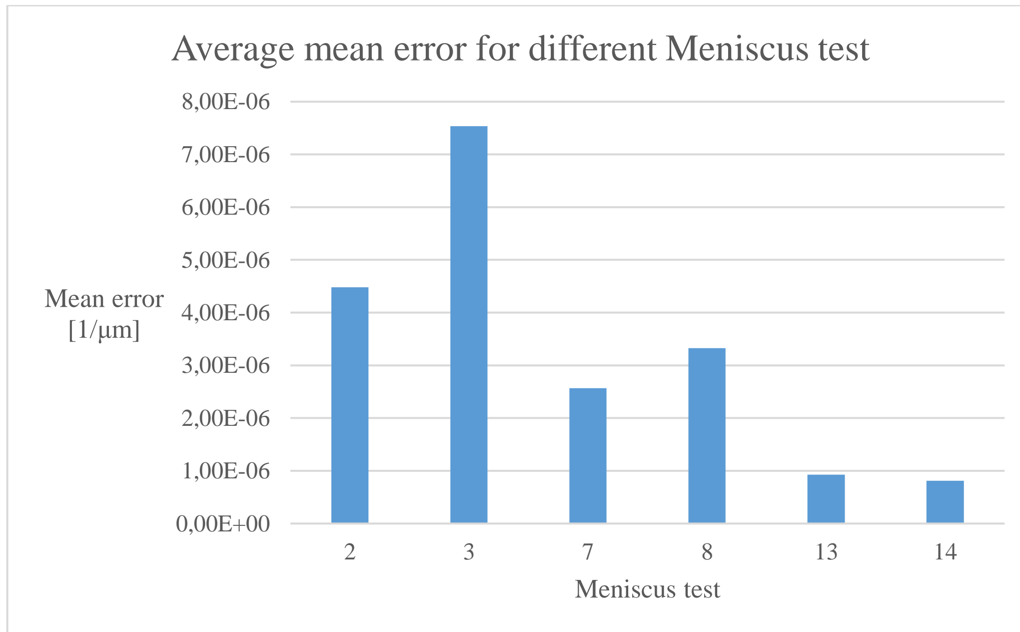

Figure 8.3: Average of mean error between 4 curvature values measured for each image relative to a pool position, averaged between different pool position for each Meniscus test

The column diagram compares the mean error between test performed with the ultrasonic cleaning procedure (A) (Meniscus test number 2 and 3), with the ultrasonic cleaning procedure (C) (Meniscus test number 7 and 8) and with new fresh silicon wafers, the ideally cleaning (Meniscus test number 13 and 14). The dispersion values are lower and acceptable for the ultrasonic cleaning (C); a standardize and reproducible procedure and adequate cleaning results have been reached.

The presence of particles in the adsorbed region, far enough from the pool edge, does not affect the measurements.

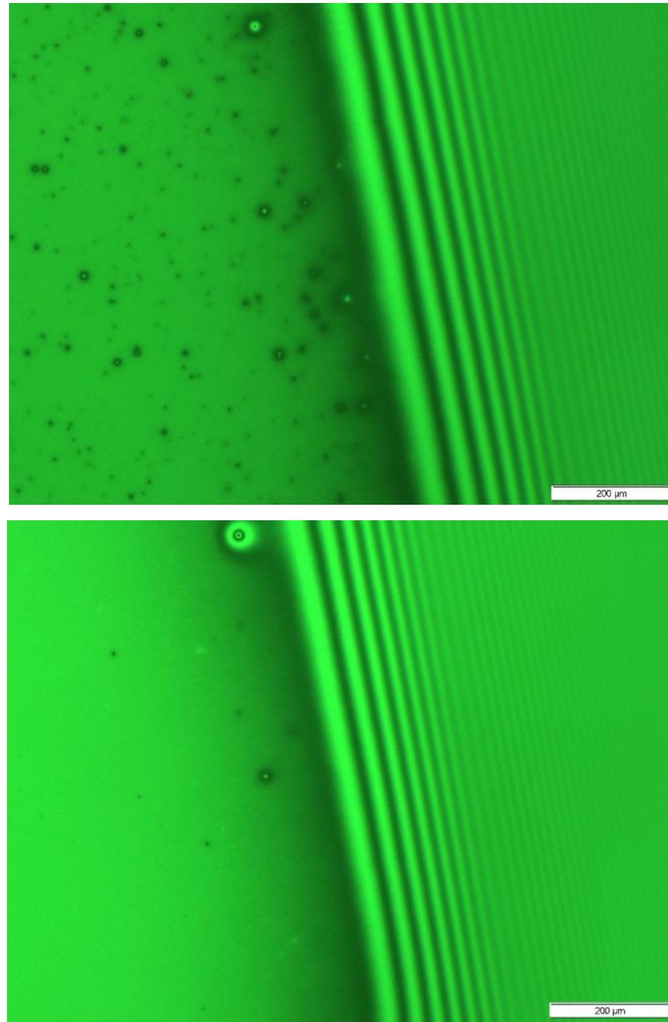

Figure 8.4: Interferometry images of octane pool edge on smooth silicon wafer after ultrasonic cleaning C (top); on fresh silicon wafer (bottom)

Considering these two interferometry images shown in Figure 8.4, at comparable pool location and amount of liquid, the one on the top presents some dust in the adsorbed layer, which is why it is not bright as the cleaner image on the bottom. Despite this, the particles do not affect the meniscus profile and the obtained value of curvature of the left picture, starting from the first bright fringe onwards, is roughly the same as that for the right image.

Test	Image	% Volume	Curvature (μm^{-1})
9	1171	60	2.27E-05
12	1226	55	2.99E-05

Table 8.1 Comparison between curvature on new fresh silicon wafer (1226) and silicon wafer cleaned using ultrasonic cleaning C (1171)

8.3. COMPARISON BETWEEN DIFFERENT AMOUNT OF LIQUID

The results are been compared for different amount of volume. The average curvature calculated considering every test is reported. The plot shows high values for percentage under 35 and slightly low for percentage greater than 65. A constant area appears from 35% to 65% with relatively constant curvature around $3 * 10^{-5}\ \mu m^{-1}$.

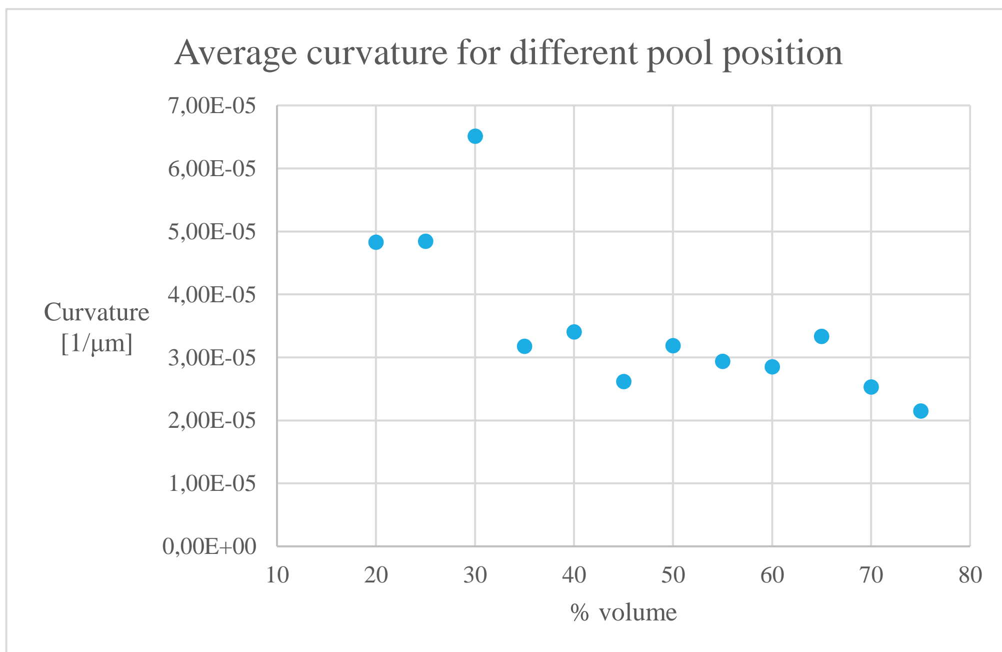

Figure 8.5: Average curvature obtained for different pool position between every Meniscus test

It can be concluded that the chamber walls affect the measurements, for pool position close to the tilted side of the micro-hole.

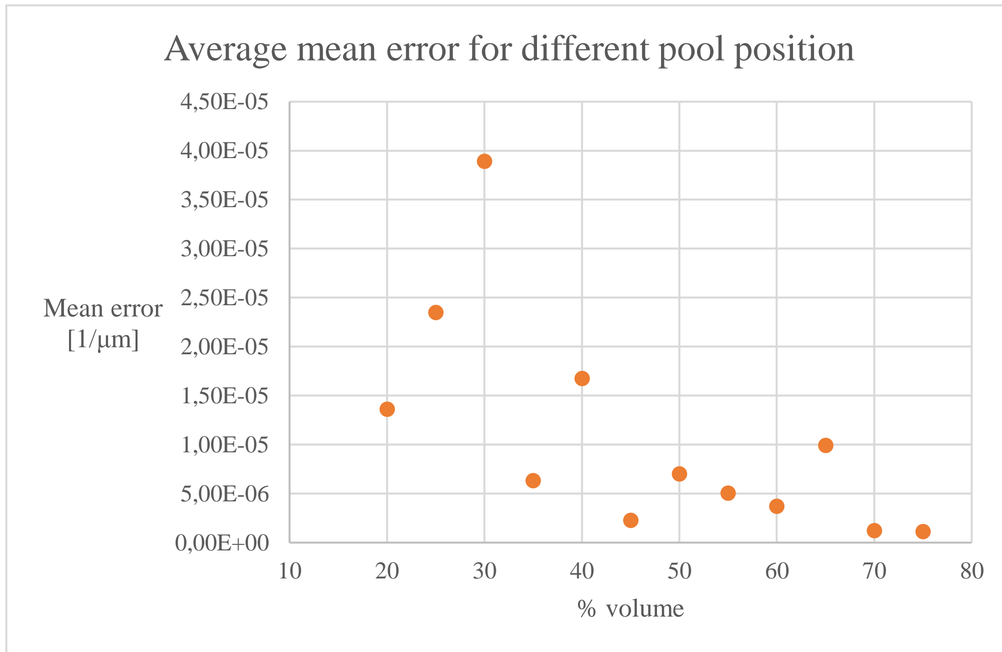

Figure 8.6: Average of mean error between values of curvature of a set images relative to a pool position, averaged considering all Meniscus test

In order to have an extended meniscus profile unrelated and unaffected by volume, the amount of liquid has to be greater than 45% the radial length of the wafer, starting from the lower tilted side. Further, the plot of the average mean error versus different pool positions shows a relatively low dispersion of measurements for amount of fluid above about 50%.

8.4. EFFECT OF CHAMBER EDGE

Analyzing the effect of chamber edge for the same pool position, similar results have been found.

Figure 8.8 shows the values of curvature for different radial location; for simplicity, the chamber has been divided in 7 horizontal areas, namely the border regions 7 and 1 closer to the edges and the central region 4, as reported in Figure 8.7.

After Meniscus test 8, interferometry images have been taken only in the central area since the considered range has been gradually restricted; before Meniscus test 5, the results were heavily affected by a not yet acceptable cleaning process. So only Meniscus test number 5, 6, 7, and 8 are taken into account for the following considerations.

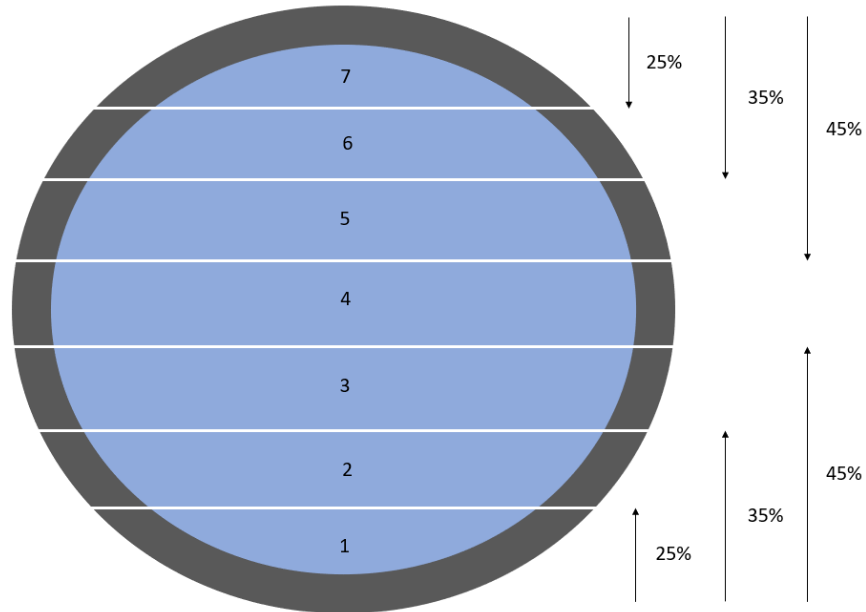

Figure 8.7: Schematic of chamber top view with marked 7 regions at different radial location

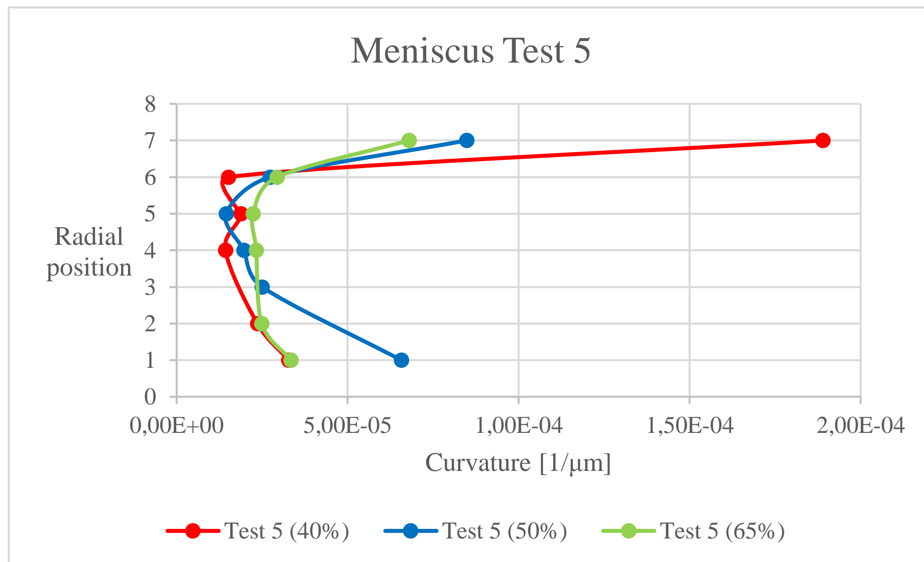

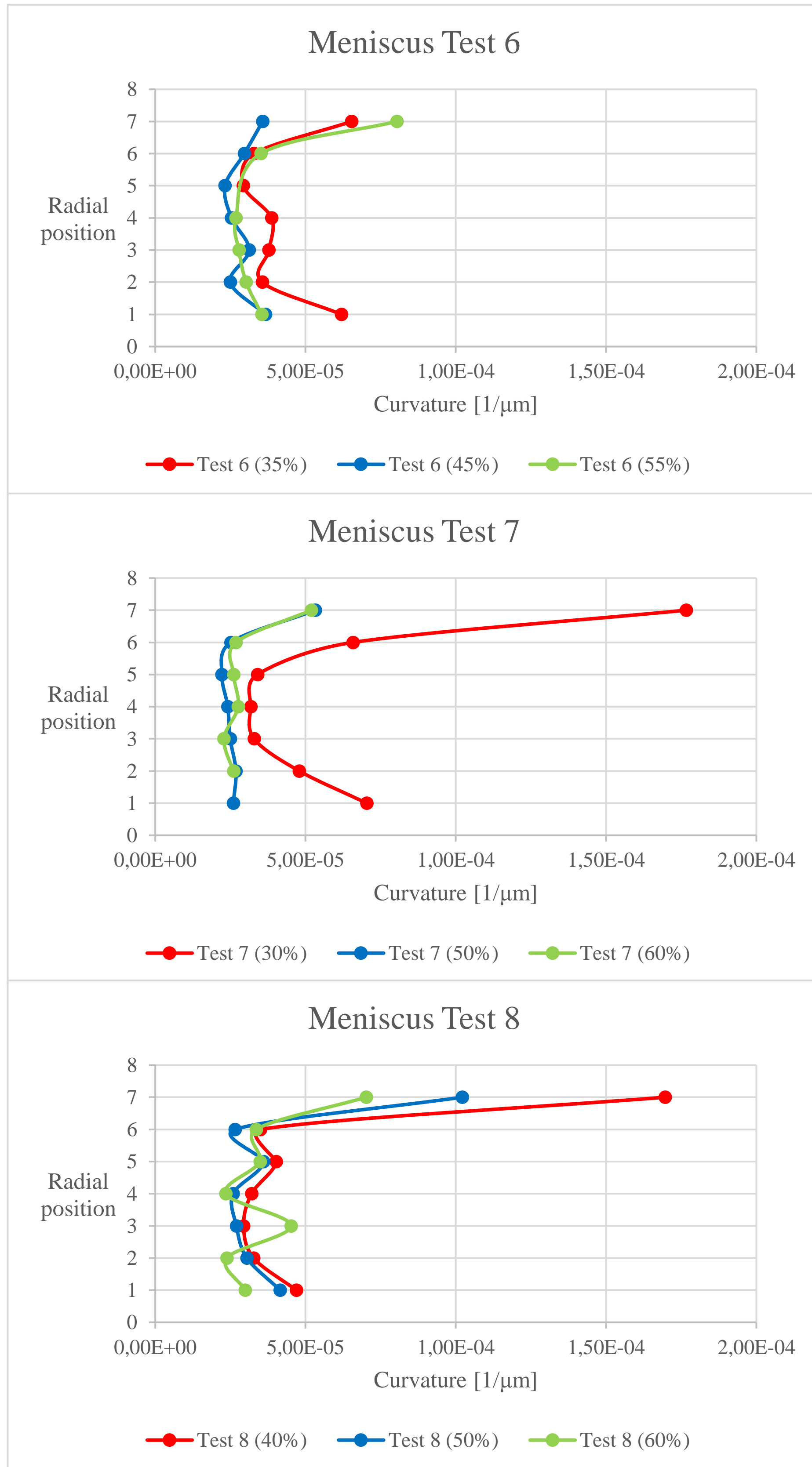

Figure 8.8: Plot of curvature for images at different radial location relative to Meniscus test 5, 6, 7, 8 for all three amounts

The influence of the chamber edge on the meniscus profile is evident, especially for region 7. The values of curvature are much higher for images captured near the upper wall for all four test, reaching in some cases a greater order of magnitude ($10^{-4}\ \mu\text{m}^{-1}$). Also, in region 1 the curvature has values slightly greater, but surely less influenced compared to region 7. This asymmetry of results arises from the fact that the chamber is probably tilted forward two directions.

In order to have consistent results and completely unaffected measurements, the interferometry images have to be taken from region 6 to region 2, including them. Considering that the location at 50% is precisely at the center of the chamber and 0% corresponds to the lateral edges, the interferometry images has to range in the central area from $\pm$ 30%.

8.5. CURVATURE COMPARISON

According to the graph reported below, a consistency of results has been reached.

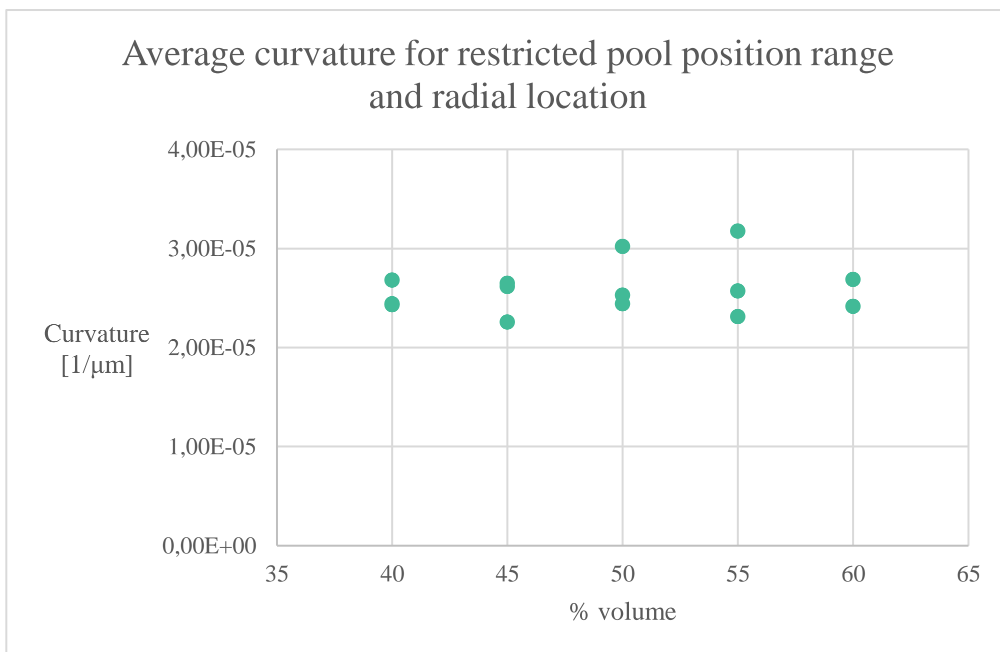

Figure 8.9: Plot of average curvature vs. pool position range 40%-60% relative to Meniscus test 9, 10, 11, 12, 13, 14

The values, referred to Meniscus test 9, 10, 11, 12, 13 and 14, have been obtained by averaging the curvature for pool position in a range that goes from 40% to 60% of volume, and excluding all the images in region 7 and 1.

Then, from this plot a final value of curvature for last six test has been calculated, averaging the results obtained for different amount of liquid. Also, the data variation range is reported.

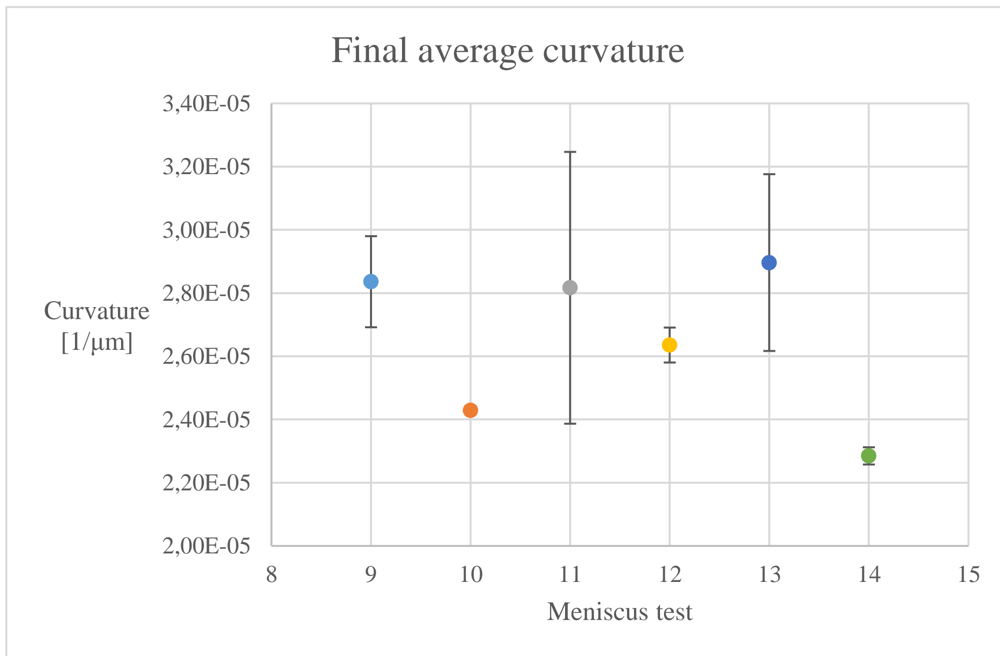

Figure 8.10: Plot of the final average of curvature between pool positions for each Meniscus test

9. CONCLUSIONS AND FUTURE WORK

The mean error associated with measuring the curvature, considering an amount of octane from 40% to 60% the length of the wafer and the range within which the interferometry images are captured from region 6 to region 2, is estimated to be about $1.3 * 10^{-6}$ $\mu\mathrm{m}^{-1}$. For the smooth silicon wafers performed in these test, the average curvature, including not only the bulk meniscus region but entirely the extended meniscus of octane, is about $2.65 * 10^{-5}$ $\mu\mathrm{m}^{-1}$.

To have a comparison, Sashidhar S. Panchamgam et al. [38] calculated the meniscus profile of pentane on a quartz substrate and found a value of curvature in the bulk meniscus region of an order of magnitude of 6000 m^{-1}. Soubhik K. Bhaumik, Monojit Chakraborty et al. [37] measured the thickness profile for a meniscus of surfactants laden water over silicon substrate and obtained a curvature in the bulk meniscus region of 80 m^{-1}. Thus, the average curvature resulted from the Meniscus test, not refers to the bulk meniscus region but averaging the entire meniscus profile, is about 3000 m^{-1} and falls into that reference range.

An improved post data processing is required to measure the constant value of curvature in the bulk meniscus region; a way to further reduce the noises and smooth the profile curve without losing the acquired data from the interference fringe pattern can be found.

An experimental and repeatable procedure and consistent results can be achieved with the ellipsometry technique as has been done for the interferometry technique, in order to measure the adsorbed film thickness in the non-evaporative region. How to perform the ellipsometry technique on rough surface has to be investigated.

The solid surfaces used in this work are smooth; further experiments with Nano-structured surfaces that have a two-scaled roughness are required, in order to measure adsorbed film thickness and bulk meniscus curvature for different roughness samples. The nanowires surfaces can be frabricated using Ag-Catalyzed Etching and by varying the etch time the height of roughness can be varied.

In order to vary the pressure inside the chamber, a redesign of the facility is required. The chamber could be thermostatically controlled with a water-jacketed unit, while being compatible with interferometry and ellipsometry technique.

Michelle L. Gee at al. [25], in order to investigate by ellipsometric measurement the equilibrium film thickness of alkane on a smooth quartz substrate, designed a sample chamber able to be outgassed and operated in a depressurized system, monitoring the pressure by a pressure transducer. Blake [39] measured the disjoining pressure as a function of film thickness for n-octane by pressing a gas bubble against the substrate when immersed in the liquid.

Compare experimentally determined disjoining pressure relationships with model, to better understand how boiling processes are affected by surface roughness, is the long-term objective of the entire project.

ACKNOWLEDGMENTS

Il primo grazie va senza dubbio alla mia famiglia, che non ha mai smesso di sostenermi durante questi 5 anni. Una famiglia che mi ha insegnato a non mollare mai, a non accontentarmi quando so di poter arrivare più in alto, a portare avanti il lavoro con determinazione, costanza, positività, forza e passione. Una famiglia che mi insegnato tantissimo, grazie alla quale sono arrivata qui, fiera di me stessa e soprattutto felice per aver reso loro orgogliosi di me.

Un grazie a tutti i miei amici, sia quelli storici che quelli conosciuti più tardi, con cui ho condiviso momenti divertenti e momenti difficili, e che hanno reso il mio percorso di ingegneria un po' più leggero (se così si può dire). Amici speciali, su cui so davvero di poter contare.

Vorrei ringraziare il mio relatore e al mio co-supervisor che mi hanno dato l'opportunità di vivere quest'esperienza a Purdue, un'esperienza che mi ha fatto crescere sia professionalmente che umanamente.

Ringrazio tutte le persone che ho incontrato durante i miei mesi negli Stati Uniti, che mi sono state vicino e senza le quali la mia avventura non sarebbe stata la stessa; come ho già detto tante volte, è stato molto più difficile tornare che non fa partire.

LIST OF FIGURES

Figure1.1: Nucleate bubble [40]

Figure1.2: Thin liquid film region of nucleated bubble

Figure 1.3: Schematic of a completely wetting meniscus; variation in adhesion force, curvature, heat flux, and thermal resistance in the contact line region of the evaporating meniscus [21]

Figure 1.4: Schematic of a liquid drop showing the quantities in the Young's equation

Figure 1.5: An increase in wetting (decrease in contact angle) results in an increased area for evaporation [41]

Figure 1.6: Schematic of a liquid drop on the rough solid surface. (a) Wenzel model; (b) Cassie-Baxter model [42]

Figure 1.7: Experimental and theoretical Hamaker constant on all surfaces [41]

Figure 1.8: Schematic drawing of an extended meniscus on a rough surface (left); cross-sectional view of a V-groove structure (right) with a flat meniscus (a) and a conformal meniscus (b)

Figure 1.9: Model prediction of disjoining pressure on structured surfaces

Figure 1.10: Schematic of three phase contact line region at isothermal condition

Figure 1.11: Polarized light reflection in ellipsometry technique

Figure 2.1: Monochromatic light reflection in interferometry technique

Figure 2.2: Grey value plot with the interpolatory envelop

Figure 2.3: Gray scale interferometry image of naturally occurring interference fringes produced from the constantly changing thickness of the corner meniscus

Figure 2.4: Gray scale interferometry image of extended meniscus; 10x objective (top); 5x objective (bottom)

Figure 3.1: Schematic of the experimental setup with cross sectional view of Monojit et al. [37]

Figure 3.2: Schematic of half cross sectional view of the chamber, with indication of components

Figure 3.3: Schematic of half cross sectional view of the chamber, with indication of dimensions

Figure 3.4: Lateral (top) and top (bottom) view of the experimental chamber assembled

Figure 3.5: Schematic of uncompressed o-ring in half cross sectional view of chamber (millimiters)

Figure 3.6: Schematic of compressed o-ring in half cross sectional view of chamber

Figure 4.1: Glass beakers under the fume hood during Piranha cleaning process (left); silicon wafer bathed in piranha mixture (right)

Figure 4.2: Interferometry image of extended meniscus after Piranha cleaning process

Figure 4.3: Ultrasonic cleaning machine during a cleaning process

Figure 4.4: Interferometry image of extended meniscus after ultrasonic cleaning A

Figure 4.5: Interferometry image of extended meniscus after ultrasonic cleaning B

Figure 4.6: Interferometry image of extended meniscus after ultrasonic cleaning C

Figure 5.1: Schematic of assembly process of chamber's components

Figure 5.2: Schematic of tilted chamber during the filling

Figure 5.3: Two interferometry images at the same horizontal position of receding meniscus during a test; taken after about an hour from the filling (top); taken after about 3 hours from the filling (bottom)

Figure 5.4: Schematic of experimental setup during a test (left); interferometry image of octane pool edge on smooth silicon wafer (right)

Figure 5.5: Experimental setup during a test

Figure 6.1: Image processing lines: user-drawn line (white), left/right boundaries for averaging (magenta, blue)

Figure 6.2: Plot of intensity between user-drawn line (blue), left/right boundaries (dashed orange, dashed red) vs. distance along profile; not parallel to fringes (top); roughly parallel to fringes (bottom)

Figure 6.3: Plot of standard deviation between rake of line profiles vs. angle adjustment of user-drawn line

Figure 6.4: Image processing line: user-drawn line (white), left/right boundaries for averaging (magenta, blue), rake of line profiles to calculate standard deviation (red); L=50, N=25 (top left); L=400, N=25 (top right); L=150, N=100 (bottom left); L=150, N=10 (bottom right)

Figure 6.5: Plot of intensity vs. distance along profile: first cut before the first dark fringe (top); second cut in the bulk meniscus region with a total length between 500 and 600 pixels (bottom)

Figure 6.6: Plot of intensity vs. distance along profile with peaks/valleys marked: profile line in pixels before smoothing (top); profile line in microns after smoothing (bottom)

Figure 6.7: Plot of film thickness smoothed profile: extrapolated portion (dashed orange), fitted curve (green), smoothed curve (purple), peaks/valleys (dots)

Figure 6.8: Plot of film thickness smoothed profile: extrapolated portion (dashed blue), smoothed curve (red)

Figure 6.9: Noisy interferometry image of octane pool edge on a nanowire surface (top); intensity plot of the noisy interferometry image (bottom)

Figure 6.10: Intensity plot with median filter addition (top); intensity plot without filter addition (bottom)

Figure 6.11: Intensity plot before smoothing with peaks/valleys marked; median filter addition (left); without filter addition (right)

Figure 6.12: Four processing lines covering four pool positions of the same interferometry image (l=150, n=25)

Figure 6.13: Schematic of extended meniscus (top); ideal trend of curvature vs. thickness profile (bottom)

Figure 6.14: Plot of curvature (second derivative) of smoothed profile (top); plot of radius of smoothed profile (bottom)

Figure 6.15: Ideal trend of thickness, slope and curvature of extended meniscus

Figure 6.16: Plot of slope (linearization) of smoothed profile

Figure 7.1: Schematic of meniscus position in viewing window of closed chamber

Figure 7.2: Interferometry images of receding meniscus at 6 different moments, from the moment immediately after the filling (first top left) to an hour later (last bottom left)

Figure 7.3: Schematic of locations of interferometry images in viewing window of closed chamber for Meniscus test 1

Figure 7.4: Piece of teflon affecting measurements during Meniscus test 2

Figure 7.5: Interferometry image of octane pool edge on fresh silicon wafer captured during Meniscus test 2

Figure 7.6: Schematic of locations of interferometry images in viewing window of closed chamber for Meniscus test 2

Figure 7.7: Interferometry image of octane pool edge on smooth silicon wafer after ultrasonic cleaning a captured during Meniscus test 3

Figure 7.8: Schematic of locations of interferometry images in viewing window of closed chamber for Meniscus test 3

Figure 7.9: Interferometry image of octane pool edge on smooth silicon wafer after ultrasonic cleaning B captured during Meniscus test 4

Figure 7.10: Schematic of locations of interferometry images in viewing window of closed chamber for Meniscus test 4

Figure 7.11: Experimental setup during meniscus test 5 with piece of rubber as sealing solution

Figure 7.12: Schematic of locations of interferometry images in viewing window of closed chamber for Meniscus test 5

Figure 7.13: Interferometry images of octane pool edge captured during Meniscus test 6 after a waiting time of 2 hours (top) and 20 hours (bottom)

Figure 7.14: Schematic of locations of interferometry images in viewing window of closed chamber for Meniscus test 6

Figure 7.15: Schematic of locations of interferometry images in viewing window of closed chamber for third filling after a waiting time of 20 hours (Meniscus test 6)

Figure 7.16: Schematic of locations of interferometry images in viewing window of closed chamber for Meniscus test 7

Figure 7.17: Schematic of locations of interferometry images in viewing window of closed chamber for Meniscus test 8

Figure 7.18: Schematic of locations of interferometry images in viewing window of closed chamber for Meniscus test 9

Figure 7.19: Interferometry images of octane pool edge captured during Meniscus test 10 after a waiting time of 6 hours (top) and 28 hours (bottom)

Figure 7.20: Schematic of locations of interferometry images in viewing window of closed chamber for Meniscus test 10

Figure 7.21: Schematic of locations of interferometry images in viewing window of closed chamber for first filling after a waiting time of 28 hours (Meniscus test 10)

Figure 7.22: Dust particle affecting octane pool edge during Meniscus test 11

Figure 7.23: Disassembled chamber after Meniscus test 11 with dust particles in octane pool

Figure 7.24: Schematic of locations of interferometry images in viewing window of closed chamber for Meniscus test 11

Figure 7.25: Schematic of locations of interferometry images in viewing window of closed chamber for Meniscus test 12

Figure 7.26: Schematic of locations of interferometry images in viewing window of closed chamber for Meniscus test 13

Figure 7.27: Schematic of locations of interferometry images in viewing window of closed chamber for Meniscus test 14

Figure 8.1: Interferometry images of receding meniscus: shortly after filling (top); after 6 hours (bottom)

Figure 8.2: Amount of receding meniscus (microns) vs waiting time to reach the steady state

Figure 8.3: Average of mean error between 4 curvature values measured for each image relative to a pool position, averaged between different pool position for each Meniscus test

Figure 8.4: Interferometry images of octane pool edge on smooth silicon wafer after ultrasonic cleaning C (top); on fresh silicon wafer (bottom)

Figure 8.5: Average curvature obtained for different pool position between every Meniscus test

Figure 8.6: Average of mean error between values of curvature of a set images relative to a pool position, averaged considering all Meniscus test

Figure 8.7: Schematic of chamber top view with marked 7 regions at different radial location

Figure 8.8: Plot of curvature for images at different radial location relative to Meniscus test 5, 6, 7, 8 for all three amounts

Figure 8.9: Plot of average curvature vs. pool position range 40%-60% relative to Meniscus test 9, 10, 11, 12, 13, 14

Figure 8.10: Plot of the final average of curvature between pool positions for each Meniscus test

LIST OF TABLES

Table 3.1: Physical properties of octane

Table 3.2: Properties and dimensions of silicon wafer

Table 7.1: Curvature measured for Meniscus test 1

Table 7.2: Curvature measured for Meniscus test 2

Table 7.3: Curvature measured for Meniscus test 3

Table 7.4: Curvature measured for Meniscus test 4

Table 7.5: Curvature measured for Meniscus test 5

Table 7.6: Curvature measured for Meniscus test 6, considering the lowest waiting time for third filling

Table 7.7: Curvature measured at different time for third filling of Meniscus test 6

Table 7.8: Curvature measured for Meniscus test 7

Table 7.9: Curvature measured for Meniscus test 8

table 7.10: curvature measured for Meniscus test 9

Table 7.11: Curvature measured for Meniscus test 10, considering the lowest waiting time for first filling

Table 7.12: Curvature measured at different time for first filling of Meniscus test 10

Table 7.13: Curvature measured for Meniscus test 11

Table 7.14: Curvature measured for Meniscus test 12

Table 7.15: Curvature measured for Meniscus test 13

Table 7.16: Curvature measured for Meniscus test 14

Table 8.1 Comparison between curvature on new fresh silicon wafer (1226) and silicon wafer cleaned using ultrasonic cleaning C (1171)

REFERENCES

[1] S.P. Fisenko, A.A. Brin, A.I. Petruchik, Evaporative cooling of water in a mechanical draft cooling tower, Int. J. Heat Mass Transfer, 47(1) (2004) 165-177

[2] O. Mahian, A. Kianifar, S.Z. Heris, D. Wen, A.Z. Sahin, S. Wongwises, Nanofluids effects on the evaporation rate in a solar still equipped with a heat exchanger, Nano Energy, 36 (2017) 134-155

[3] F. Su, N. Zhao, Y. Deng, H. Ma, An Ultrafast Vitrification Method for Cell Cryopreservation, J. Heat Transfer, 140(1) (2017) 012001-012001-012004

[4] K. Pettigrew, J. Kirshberg, K. Yerkes, D. Trebotich, D. Liepmann, Performance of a MEMS based micro capillary pumped loop for chip-level temperature control, 2001, Technical Digest, 14th IEEE International Conference on Micro Electro Mechanical Systems (Cat. No.01CH37090)

[5] Wayner, P. C., Jr., Interfacial profile in the contact line region of a finite contact angle system, 1980, Journal of Colloid and Interface Science 77(2): 495-500

[6] Kim, I. Y. and P. C. Wayner Jr, Shape of an Evaporating Completely Wetting Extended Meniscus, 1996, Journal of Thermophysics and Heat Transfer 10(2): 320-325

[7] Wayner, P. C., Jr., Intermolecular Forces in Change of Phase Heat Transfer: 1998 Donald Q. Kern Award Review, 1999, AIChE Journal 45: 2055-2068

[8] H. Wang, S.V. Garimella, J.Y. Murthy, Characteristics of an evaporating thin film in a microchannel, Int. J. Heat Mass Transfer, 50(19-20) (2007) 3933-3942

[9] H. Hu, C.R. Weinberger, Y. Sun, Effect of nanostructures on the meniscus shape and disjoining pressure of ultrathin liquid film, Nano Lett., 1991, 14(12) (2014) 7131-7137

[10] L. Leger, J.F Joanny, Liquid spreading, 1992 Rep. Prog. Phys. 55 431

[11] George Palasantzas, Wetting on rough self-affine surfaces, Phys. Rev. B 51, 14612,1995

[12] Wayner, P. C., Jr., et al., The Interline Heat-Transfer Coefficient of an Evaporating Wetting Film, 1976, International Journal of Heat and Mass Transfer 19: 487-492

[13] Wayner, P. C., Jr., The Effect of Interfacial Mass Transport on Flow in Thin Liquid Films, 1991, Colloids and Surfaces 52: 71-84

[14] Renk, F., et al., On the transition between a wetting film and a capillary meniscus, 1978, Journal of Colloid and Interface Science 67(3): 408-414

[15] Renk, F. J. and P. C. Wayner, Jr., An Evaporating Ethanol Meniscus, Part I: Experimental Studies, 1979, Journal of Heat Transfer 101: 55-58

[16] Liu, A.-H., et al., Image scanning ellipsometry for measuring the transient, film thickness profiles of draining liquids, 1994, Physics of Fluids 6(6): 1963-1971

[17] DasGupta, S., et al., Use of the Kelvin-Clapeyron Equation to Model an Evaporating Curved Microfilm, 1994, Journal of Heat Transfer 116: 1007-1015

[18] D.S. Antao, S. Adera, Y. Zhu, E. Farias, R. Raj, E.N. Wang, Dynamic Evolution of the Evaporating Liquid–Vapor Interface in Micropillar Arrays, Langmuir, 32(2) (2016) 519-526

[19] S. DasGupta, J.L. Plawsky, P.C. Wayner, Interfacial force field characterization in a constrained vapor bubble thermosyphon, AlChE J., 41(9) (1995) 2140-2149

[20] M.S. Hanchak, M.D. Vangsness, L.W. Byrd, J.S. Ervin, Thin film evaporation of n-octane on silicon: Experiments and theory, Int. J. Heat Mass Transfer, 75 (2014) 196-206

[21] M. Ojha, A. Chatterjee, G. Dalakos, P.C. Wayner, Jr., J.L. Plawsky, Role of solid surface structure on evaporative phase change from a completely wetting corner meniscus, Phys. Fluids, 22(5) (2010) 052101

[22] M. Potash Jr, P.C. Wayner Jr, Evaporation from a two-dimensional extended meniscus, Int. J. Heat Mass Transfer, 15(10) (1972) 1851-1863

[23] S. Moosman G.M Homsy, Evaporating menisci of wetting fluids, J. of Colloid and Interface Science, 1980, 212-223

[24] Jack G. Truong, Peter C. Wayner, Effects of capillary and van der Waals dispersion forces on the equilibrium profile of a wetting liquid: Theory and experiment, J. Chem. Phys. 87, 4180 (1987)

[25] Michelle L. Gee, Thomas W. Healy et al., Ellipsometric Studies of Alkane Adsorption on Quartz, Journal of Colloid and Interface Science, 1989

[26] R. Pericet-Cámara, A. Best, H.J Butt, E. Bonaccurso, Effect of Capillary Pressure and Surface Tension on the Deformation of Elastic Surfaces by Sessile Liquid Microdrops: An Experimental Investigation, Langmuir, 2008, 24 (19), pp 10565–10568

[27] J. B. Sweeney, T. Davis, L. E. Scriven, Equilibrium Thin Films on Rough Surfaces. 1. Capillary and Disjoining Effects, Langmuir 1993, 9, 1551-1555 1551

[28] S. Li, R. Furberg, Muhammet S. Toprak, B. Palm, M. Muhammed, Nature-Inspired Boiling Enhancement by Novel NanostructuredMacroporous Surfaces, Advanced Functional Materials, 2008

[29] Q. Liao, T.C Jena, Q. Chena, L. Li, W. Cuib, Heat transfer performance in 3D internally finned heat pipe, International Journal of Heat and Mass Transfer, 2007, Volume 50, 1231-1237

[30] H. Kubo, H. Takamatsu, H. Honda, Effects of Size and Number Density of Micro-reentrant Cavities on Boiling Heat Transfer from a Silicon Chip Immersed in Degassed and Gas-dissolved FC-72, Journal of Enhanced Heat Transfer, 1999, 151-160

[31] Anderson, D. M. and S. H. Davis, The spreading of volatile liquid droplets on heated surfaces, Physics of Fluids, 1995, 7(2): 248-265

[32] Y. Takata, S.Hidaka, A.Yamashita, H.Yamamoto, Evaporation of water drop on a plasma-irradiated hydrophilic surface, International Journal of Heat and Fluid Flow, 2004, 320-328

[33] McHale, G., et al., Analysis of droplet evaporation on a superhydrophobic Surface, Langmuir, 2005, 21(24): 11053-11060

[34] Cheng, Y. T. and D. E. Rodak, Is the lotus leaf superhydrophobic? Applied Physics Letters, 2005, 86(14)

[35] M.O. Robbins, D. Andelman, J.-F. Joanny, Thin liquid films on rough or heterogeneous solids, Phys. Rev. A, 43(8) (1991) 4344-4354

[36] H. Hu, C.R. Weinberger, Y. Sun, Effect of nanostructures on the meniscus shape and disjoining pressure of ultrathin liquid film, Nano Lett., 14(12) (2014) 7131-7137

[37] S. K. Bhaumik, Monojit Chakraborty, S. Ghosh, S. Chakraborty, and S. DasGupta, Electric Field Enhanced Spreading of Partially Wetting Thin Liquid Films, Langmuir, 2011

[38] Sashidhar S. Panchamgam et al., J. Heat Transfer, 2005

[39] Blake, T. D., Chem. Soc. Faraday Trans., (1075) 71, 192

[40] T. Chen, Suresh V. Garimella, Measurements and high-speed visualizations of flow boiling of a dielectric fluid in a silicon microchannel heat sink, 2006, Elsevier

[41] M. Ojha, Contact line wettability and transport during phase change processes from nanostructured surfaces, 2008, Rensselaer Polytechnic Institute, New York

[42] M. Nosonovsky, B. Bhushan, Why re-entrant surface topography is needed for robust oleophobicity, 2016, Philosophical Transactions of the Royal Society A